Studies of the Inverse Problem in Supersymmetry in Particle Physics

Diplomarbeit

von

Matthias Hamer

geboren in

Paderborn

angefertigt am

II. Physikalischen Institut
der Georg-August-Universität Göttingen

2010

Angenommen am: 08. Februar 2010
Referent: Prof. Dr. Arnulf Quadt
Korreferent: Dr. Carsten Hensel

GEORG-AUGUST-UNIVERSITÄT GÖTTINGEN

II. Physikalisches Institut

Studies of the Inverse Problem in Supersymmetry in Particle Physics

von

Matthias Hamer

A study on the inverse problem in supersymmetry in particle physics is presented. A method for the measurement of an edge in the dimuon spectrum of a decay chain of the second lightest neutralino at the ATLAS experiment is tested for an mSUGRA model in a best case scenario. This kinematic edge is then used together with a set of other observables to extract the fundamental Lagrangian parameters with the program Fittino. Two new interfaces for Fittino and a first study on systematic uncertainties on the central parameter values obtained with Fittino are presented.

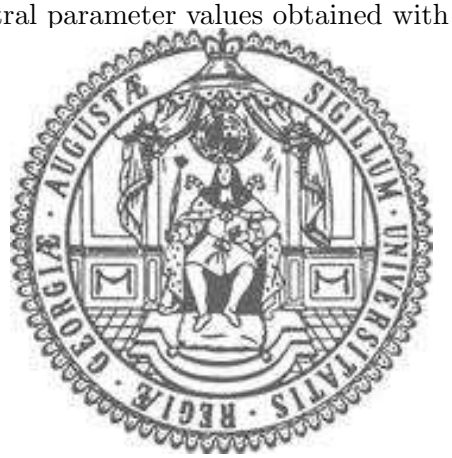

Post address:
Friedrich-Hund-Platz 1
37077 Göttingen
Germany

II. Physikalisches Institut
Georg-August-Universität Göttingen
February 2010

Contents

1 Introduction

More than a century ago it was believed that physicists had solved the last great mysteries of nature [1]. The remaining caveats, which could not be explained at that time, like the spectrum of the black-body radiation, were thought of as minor inconsistencies to be resolved very soon. However, the approaches that were followed for the resolution of the remaining problems brought up the formulation of quantum theory and general relativity. These revolutionised the whole view of the world as accepted in those days and pushed open the door to new scientific territories which were unknown to exist until then. Now, more than a hundred years after most questions in physics seemed to be answered and the theoretical description of nature was assumed to be complete, we have to admit that the number of unanswered, fundamental questions has steadily increased since then.

One of the fields in physics that arose from a number of new experimental results and new theoretical concepts is the field of elementary particle physics, whose birthday is sometimes defined by the discovery of the electron by J. J. Thompson in 1897 [2]. In the following decades discoveries of more and more elementary particles and bound states were announced, finally opening out in the discovery of what is today believed to be the top quark [3] and the tau neutrino [4]. The current theory of particle physics, the Standard Model (SM), which has been developed for many years, has until now been most successfull in describing the experimental results in this field.

However, it is known today that the SM is not a complete theory of nature. There is a number of shortcomings, which require either an extended or a completely new theory. The Large Hadron Collider (LHC) at the European Organization for Nuclear Research (CERN) near Geneva, Switzerland, has been built to provide experimental input for the search of such an extended or new theory, amongst other purposes. It is expected that new physics will be observed at the LHC, as physicists will set foot on so far unknown ground when the machine starts colliding protons at its design center-of-mass energy of 14 TeV. Collisions at this center-of-mass energy have never been observed under laboratory conditions so far, such that the LHC will allow physicists all over the world to "explore strange new worlds, to seek out new particles and new interactions, to boldly go where no man has gone before".

One family of the extensions to the SM, which resolve some of its shortcomings in an elegant way, are supersymmetric extensions, the best studied of which is the Minimal Supersymmetric Standard Model (MSSM). This theory predicts a number of so far undiscovered particles, the so called superpartners of the SM particles, which makes it attractive not only for particle physics but also for cosmology. This is because the lightest of these new particles might turn out to constitute a significant amount of the Cold Dark Matter in the universe, whose identity is mainly unknown until now.

The question if supersymmetry (SUSY) is realised in nature is therefore one of the most interesting unanswered questions in modern particle physics. A number of experiments at the Large Electron Positron Collider and at the Tevatron, as well as astrophysical experiments, have already excluded certain regions in the MSSM configuration space. However, it is expected that a definite answer to this question can for the first time be given by data from the experiments at the LHC.

At the LHC it will be possible to directly produce the superpartners of the SM particles with a significant rate for the first time, given that nature is actually supersymmetric. The measurement of these particles' properties, like their masses and couplings, at the two LHC multipurpose experiments ATLAS and CMS will finally allow for a first reconstruction of the fundamental parameters of the supersymmetric theory and the rejection of some supersymmetric models. This will in turn allow for the prediction of other important quantities, one of which is the fraction of supersymmetric Cold Dark Matter. As for any other measurement, a detailed analysis of the uncertainties on the reconstructed parameters is crucial, as these are finally pivotal for the uncertainties - and therefore the significance - of the predicted quantities. It is the aim of this study to provide a first insight into the complex task of SUSY parameter estimation, with the main focus on a first estimation of systematic uncertainties.

After this introduction, a short theoretical overview about the SM and its minimal supersymmetric extension, the MSSM is given in chapter 2. In chapter 3, the basic problem of SUSY parameter estimation is introduced, starting with a very simple example from classical mechanics which is then carried over to SUSY in particle physics. The LHC and the ATLAS detector are shortly described in chapter 4. In chapter 5, a method for the measurement of a mass related supersymmetric observable is tested in a best-case scenario with the ATLAS detector. This observable, together with a number of other toy measurements, is finally used in chapter 6, where a first study on systematic uncertainties for SUSY parameter extraction with the program *Fittino* is presented.

In the present thesis, natural units have been used, i.e. $c = 1 = \hbar$. All masses and momenta are therefore given in units of eV and not in $\mathrm{eV/c}^n$. In all shown Feynman diagrams, time floats from left to right.

2 The Standard Model of Elementary Particle Physics and its Minimal Supersymmetric Extension

2.1 The Standard Model of Elementary Particle Physics

The so far most successfull theoretical model of elementary particle physics is the Standard Model (SM), which is a locally gauge invariant, renormalisable, Lorentz covariant quantum field theory. It has been developed over many years, and in its current form it has been most successfull in describing nearly all experimental results in the field of high energy physics [5–8]. A detailed description of the aspects of quantum field theory and the SM can for example be found in [9–13], on which this overview mainly relies.

The SM distinguishes between two types of elementary particles, namely fermions with half-integer spin, and bosons with integer spin. There are twelve fermions and four vector bosons, the former making up the matter in the universe, the latter mediating forces between them. By now it is believed that there are four such fundamental interactions, three of them being described by the SM. Historically, the first of these is the electromagnetic interaction, which was described classically by Maxwell [14]. Electromagnetic interactions take place between particles carrying an electric charge and are mediated by the photon. The second fundamental force is the weak interaction, known for the β-decay, as an example. The three heavy gauge bosons $W^{\pm}$ and Z^0 are the force carriers associated to the weak interaction, whose associated hypercharge is the weak isospin. In atomic nuclei, the dominant force is the strong force, which is the third interaction being described by the SM. This force affects particles which carry a so-called colour charge and is mediated by the gluons. The strength of each force is characterised by a coupling constant. At relatively low energies (≤ 1 GeV), these numbers are at the order of 1 for strong interactions, 10^{-2} for electromagnetic and 0.7 for weak interactions. Only particles carrying the associated charge can interact via the respective fundamental force. Finally, the last particle in the SM is a fundamental scalar, the Higgs particle. All particles in the SM acquire mass via their coupling to the Higgs field. This last particle has not been found until now (February 2010).

Gravity, which was discussed by physicists even before electromagnetic interactions, is not a part of the SM. Although gravity is most evident in everyday life, it is the weakest of the fundamental interactions. It appears dominant at large scales only because most objects do not carry any net charge associated with the stronger interactions, such that these become negligible. At scales where quantum effects become visible, and which are accessible today, gravity does not play a key role, such that no hints on a quantum theory of gravity are given by the experimental side. In addition, despite the fact that the classical force laws of gravitational and electric interactions are mathematically identical, the hypothetical force mediator in quantum gravity would carry spin 2, in contrast to the photon, which carries spin 1. This is due to the fact that the source of gravity is the stress-energy tensor, which is of second rank, whereas the four-current, the source of electromagnetism, is a first rank tensor. This complicates the formulation

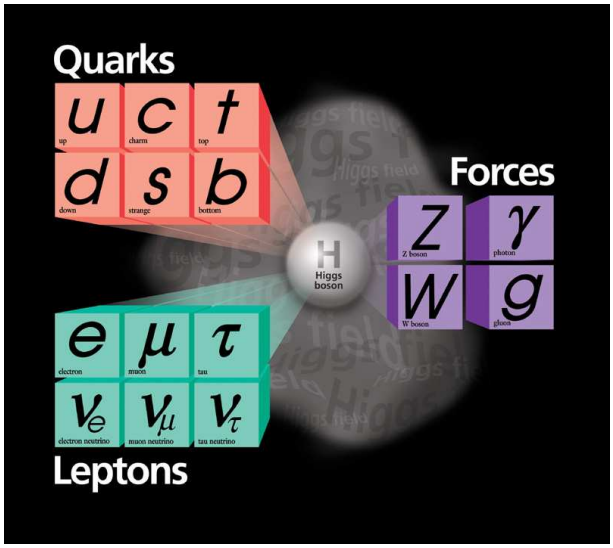

Figure 2.1: The particle content of the SM, which contains six quarks (upper left), three charged leptons and three neutral leptons (lower left), as well as four gauge bosons (right) and the Higgs-boson (centre), which has not been experimentally observed, yet. The quarks in principle occur with three different colour charges.

of a quantum theory of gravity, and although Weinberg gave a treatment of spin 2 particles (see, for example, [15]), not much attention will be paid to gravity in the following.

The particle content of the SM is shown in Figure 2.1 and Tables 2.1 and 2.2. In the SM, each particle is connected to an antiparticle, which has the same quantum numbers except for the charge. As a matter of fact, neutrinos do not carry charge, such that they might be Majorana fermions being their own antiparticle. However, this is not confirmed by experiment, yet. The fermions, of which all visible matter in the universe is composed according to the SM, are divided into leptons and quarks. While the former can exist as free particles, the latter always build bound states, like the proton, due to confinement. The charged leptons couple to photons and the heavy gauge bosons, while the neutral leptons only interact weakly. In addition, the quarks also carry a colour charge and are therefore liable to the strong force, too.

2.1.1 Local Gauge Invariance, Interactions and the Higgs Mechanism

One of the remarkable features of the SM is the emergence of the SM gauge bosons and interactions from the requirement of local gauge invariance of the free theory. This is one of the most fundamental principles in particle physics: The SM gauge bosons are not put into the theory by hand, but it is the concept of symmetries that rules all particle interactions. In the following, internal symmetries, i.e. transformations taking place in abstract spaces, are considered rather than external symmetries, i.e. space-time transformations. If not stated otherwise, the Einstein notation is used.

A physical system is said to be invariant - or symmetric - with respect to a certain transformation if the action integral

$$S = \int L\left(\phi_i, \partial_\mu \phi_i, x^\mu\right) dx_0 = \int \mathcal{L}\left(\phi_i, \partial_\mu \phi_i, x^\mu\right) d^4x, \tag{2.1}$$

where L is the Lagrangian, $\mathcal{L}$ the Lagrangian density, x^μ the relativistic space-time coordinates

Particle	Type	Generation	Mass [MeV]	El. Charge
electron-neutrino (ν_e)	lepton	I	$\geq 0 \leq 2 * 10^{-6}$	0
electron (e)	lepton	I	0.511	-1
muon-neutrino (ν_μ)	lepton	II	$\geq 0 \leq 2 * 10^{-6}$	0
muon (μ)	lepton	II	105.7	-1
tau-neutrino ν_τ	lepton	III	$\geq 0 \leq 2 * 10^{-6}$	0
tau (τ)	lepton	III	1,776.84 $\pm$ 0.17	-1
up (u)	quark	I	$1.5 \leq m_u \leq 3.3$	+2/3
down (d)	quark	I	$3.5 \leq m_d \leq 6.0$	-1/3
charm (c)	quark	II	$1{,}270^{+70}_{-110}$	+2/3
strange (s)	quark	II	105^{+25}_{-35}	-1/3
top (t)	quark	III	$(171.3 \pm 1.6) \cdot 10^3$	+2/3
bottom (b)	quark	III	$(4.2^{+0.17}_{-0.07}) \cdot 10^3$	-1/3

Table 2.1: The SM fermions with their masses and electric charge. Leptons and quarks are separated into three generations, as illustrated here. The masses and charges are taken from [16]. The extraordinary role of the top quark in particle physics becomes clear, as its mass is nearly two orders of magnitude above the mass of the b-quark, which is the next heaviest fermion. Due to its high mass, the top quark decays before it can form any bound states. It's charge has not been measured until now.

Particle	Associated Interaction	Mass [GeV]	El. Charge
gluon (g)	strong	0	0
photon (γ)	electromagnetic	0	0
$W^\pm$	weak	80.398 $\pm$ 0.025	$\pm$1
Z^0	weak	91.188 $\pm$ 0.002	0

Table 2.2: The Standard Model gauge bosons with their masses and electric charge. The numbers are taken from [16]. In addition to their masses and charge, the associated gauge interactions are shown.

and the ϕ_i denote the involved quantum fields, does not change under the transformation. This implies that the equations of motion for the physical fields ϕ_i, given by the Euler-Lagrange equations

$$\partial_\mu \left(\frac{\partial \mathcal{L}}{\partial \left(\partial_\mu \phi_i \right)} \right) - \frac{\partial \mathcal{L}}{\partial \phi_i} = 0, \tag{2.2}$$

stay invariant under the transformation, while the Lagrangian may change by a total derivative. Noether's theorem, which was proven by Emmy Noether in 1918 for the first time [17], connects such symmetries to conserved quantities. It is of fundamental importance in physics. If the transformation

$$x^\mu \rightarrow x^\mu + \delta x^\mu = x^\mu + \epsilon X^\mu, \tag{2.3}$$

$$\phi_i \rightarrow \phi_i + \delta \phi_i = \phi_i + \epsilon \Phi_i \tag{2.4}$$

leaves the action integral invariant, Noether's theorem states that the quantities

$$j^\mu = -\frac{\partial \mathcal{L}}{\partial(\partial_\mu \phi_i)} \Phi_i + \left(\frac{\partial \mathcal{L}}{\partial(\partial_\mu \phi_i)} \partial_\nu \phi_i - \mathcal{L} \delta^\mu_\nu \right) X^\nu \tag{2.5}$$

are conserved in the sense that

$$\partial_\mu j^\mu = 0. \tag{2.6}$$

An important requirement is that the transformations are continuous. The operators performing such transformations on quantum fields are representations of Lie-groups, whose elements depend on one or more continuous parameters and are differentiable with respect to these. It was shown by Wigner, that these representations must be either unitary or anti-unitary [18]. Any unitary operator U acting on a physical field, can be written as

$$U(\Theta) = e^{i\Theta\mathbf{A}}, \tag{2.7}$$

where Θ is a vector of the group parameters and $\mathbf{A}$ a vector of hermitian operators. The operators A_i are called the generators of the group, as for infinitesimal transformations, i.e. infinitesimal values of each Θ_i, (2.7) can be written as

$$U(d\Theta) = 1 + i\mathbf{A}d\Theta. \tag{2.8}$$

Any finite transformation can then be constructed from these infinitesimal transformations. If $\Theta \neq \Theta(x)$, a system is said to be globally invariant under the transformations $U(\Theta)$. If the parameters are allowed to be functions of space and time, the system is said to be locally invariant under the transformation U. It is now summarised how the requirement of gauge invariance under local U(1) phase transformations for a system with one free electron yields the existence of a gauge field, which is the photon field in this case.

The Lagrangian density for a free electron field ψ is given by

$$\mathcal{L} = i\overline{\psi}\gamma^\mu\partial_\mu\psi - m_e\overline{\psi}\psi, \tag{2.9}$$

which, by applying (2.2), yields the Dirac Equation,

$$\left(i\gamma^\mu\partial_\mu - m_e\right)\psi = 0. \tag{2.10}$$

The Lagrangian density (2.9) is obviously invariant under global U(1)-phase transformations

$$\psi \to e^{i\alpha}\psi = (1 + i\alpha)\,\psi, \qquad\qquad \alpha \in \mathbb{R} \tag{2.11}$$

where the equal sign is valid for infinitesimal transformations only. The invariance under these transformations, according to Noether's Theorem, implies the conservation of the current

$$j^\mu_{em} \propto \overline{\psi}\gamma^\mu\psi. \tag{2.12}$$

The proportionality factor can then be chosen as the electron's charge $-e$, such that (2.12) is the electron's charge current. This choice identifies the generators of this symmetry with the charge operators, Q. Applying (2.6) leads to charge conservation. This shows that the phase α is of no physical meaning, such that it can be chosen arbitrarily and fixed. At two different places, different values of α, i.e. different gauges, might be chosen. This way, α becomes dependent on the space-time coordinates, but the physics observed in both places should be the same. For this reason not only global, but also local gauge invariance is imposed.

However, (2.9) is not invariant under local phase transformations

$$\psi \to e^{i\alpha(x^\mu)}\psi. \tag{2.13}$$

This is due to the derivative with respect to x^μ in the first term of the Lagrangian. Applying (2.13) yields

$$\delta\mathcal{L} = -\overline{\psi}\gamma^\mu\psi\partial_\mu\alpha(x^\mu), \tag{2.14}$$

which is not a total derivative. The problem is solved by introducing the covariant derivative

$$D_\mu = \partial_\mu - ieA_\mu, \tag{2.15}$$

where the vector field A_μ is required to transform as

$$A_\mu \to A_\mu + \frac{1}{e}\partial_\mu\alpha(x^\mu) \tag{2.16}$$

under a local phase transformation. Rewriting (2.9) with the substitution (2.15) yields

$$\begin{aligned}\mathcal{L} &= i\overline{\psi}\gamma^\mu D_\mu\psi - m_e\overline{\psi}\psi \\ &= \overline{\psi}(i\gamma^\mu\partial_\mu - m_e)\psi + e\overline{\psi}\gamma^\mu\psi A_\mu \\ &\overset{(2.12)}{=} \overline{\psi}(i\gamma^\mu\partial_\mu - m_e)\psi - j^\mu_{em}A_\mu,\end{aligned} \tag{2.17}$$

where the latter equal sign is valid because the conserved current according to Noether's theorem is the same for both global and local phase transformations. Thus the requirement of local gauge invariance forces the introduction of a new vector field which couples to the electron. The equation of motion obtained by (2.17) is

$$(i\gamma^\mu\partial_\mu - m_e)\,\psi + e\gamma^\mu\psi A_\mu = 0, \tag{2.18}$$

which is exactly what is obtained by setting up the single particle wave equation for an electron in an electromagnetic field, without imposing any specific transformation behaviour. The gauge field A_μ can therefore be identified with the photon field, and the Lagrangian (2.17) is "completed" by adding the kinetic term for the photon,

$$\mathcal{L} = \overline{\psi}\,(i\gamma^\mu\partial_\mu - m_e)\,\psi + e\overline{\psi}\gamma^\mu A_\mu\psi - \frac{1}{4}F_{\mu\nu}F^{\mu\nu}, \tag{2.19}$$

where the field strength tensor

$$F_{\mu\nu} = \partial_\mu A_\nu - \partial_\nu A_\mu, \tag{2.20}$$

which is invariant under (2.16), has been used. A mass term proportional to $m^2A_\mu A^\mu$ is forbidden by gauge invariance.

The physically well motivated requirement for invariance under local U(1) phase transformations of a free electron field yields the complete Lagrangian density for quantum electrodynamics; a natural symmetry introduces one of the four fundamental interactions.

The other two interactions described by the SM can be derived in the very same way, just that different transformations need to be taken into account. For strong interactions, these are local SU(3) phase transformations,

$$\psi_q \to U_s(\alpha)\psi_q = e^{i\alpha_i(x^\mu)\Lambda_i}\psi_q, \tag{2.21}$$

where ψ_q denotes a quark field, the α_i are the continuous parameters of the transformation and the Λ_i are the respective generators. There are three types of colour charge, namely red, green

and blue, but all free particles observed so far do not carry any net colour. This is the reason why SU(3) rather than U(3) transformations are considered. As stated above, the matrix U_s needs to be unitary, which requires the generators to be hermitian. Furthermore, since $U_s \in$ SU(3) and thus $\det U = 1$, the Λ_i are required to be traceless. In general there are eight linearly independent, traceless hermitian matrices, which are mostly chosen as the eight Gell-Mann matrices λ_i. These matrices do not commute pairwise, which has remarkable consequences. If the invariance of (2.9), where ψ is to be replaced by a quark field ψ_q, under transformations (2.21) is requested, eight gauge fields G^a_μ have to be introduced. Since

$$[\Lambda_i, \Lambda_j] = i f_{ijk} \Lambda_k, \tag{2.22}$$

with the SU(3) structure constants f_{ijk}, these fields need to transform as

$$G^i_\mu \to G^i_\mu - \frac{1}{g_s} \partial_\mu \alpha_i(x^\mu) - f_{ijk} \alpha_j G^k_\mu \tag{2.23}$$

in order to achieve gauge invariance. The kinetic term for the SU(3) gauge fields becomes

$$\mathcal{L}_{kin,gauge} = -\frac{1}{4} G^i_{\mu\nu} G^{\mu\nu}_i, \tag{2.24}$$

where

$$G^i_{\mu\nu} = \partial_\mu G^i_\nu - \partial_\nu G^i_\mu - g_s f_{ijk} G^j_\mu G^k_\nu. \tag{2.25}$$

Due to the non-vanishing structure constants of the SU(3) group, self interaction terms need to be introduced in the field strength tensor $G^i_{\mu\nu}$. These are of third and fourth order in the eight gauge fields, which are the eight gluon fields, physically. The mediators of the strong force carry colour and thus couple to themselves. This is directly related to the so-called *asymptotic freedom*, which describes the fact that strong interactions become smaller at smaller distances. As in the electromagnetic case, the gluons must be massless because the introduction of a mass term would spoil the local gauge invariance again.

For weak interactions, the procedure is not that straight forward. The reason for this is that the gauge bosons associated to weak interactions are known to be massive. For the theory discussed so far, this is a fundamental problem. Mass terms for the gauge fields, which are put into the Lagrangian density by hand, besides spoiling the symmetry, spoil renormalisability, which is discussed in chapter 2.1.2, as well. This problem can be solved in an elegant way via the Higgs mechanism. Before this mechanism is described, electroweak unification needs to be summarised.

The charge associated to weak interactions is the weak isospin T^i. The strength of weak interactions becomes comparable to that of electromagnetic interactions at scales larger than roughly 100 GeV. The relative weakness of the weak interactions with respect to electromagnetic interactions at lower momentum transfers is related to the mass of the heavy gauge bosons as the propagator for the Z^0 and $W^\pm$ bosons is given by

$$\frac{-i\left(g_{\mu\nu} - q_\mu q_\nu / M^2\right)}{q^2 - M^2}, \tag{2.26}$$

where M denotes the mass of the respective boson. When trying to construct weak currents which reflect an assumed underlying SU(2) symmetry, these currents have only left chiral components due to the V-A structure of the weak interactions. Taking into account experimental data from neutrino-quark scattering, this cannot be correct. The neutral weak current

$$J^3_\mu = \frac{1}{2}\left(\overline{\nu_L} \gamma_\mu \nu_L - \overline{e_L} \gamma_\mu e_L\right), \tag{2.27}$$

associated to the Z^0, does not include a right chiral component, but a right chiral component is experimentally observed.

Now, (2.12) is a neutral current with both a right chiral and a left chiral component. Combining the electromagnetic with the neutral weak current, introducing the hypercharge

$$Y = 2\left(Q - T^3\right), \tag{2.28}$$

leads to

$$j_\mu^Y = 2\left(j_\mu^{em} - J_\mu^3\right). \tag{2.29}$$

In analogy to the U(1) symmetry group, generated by the charge operator Q, the operator Y generates a new symmetry group, which is named $\mathrm{U}(1)_Y$ to distinguish between the mixed - or unified - electroweak symmetry group and the pure electromagnetic symmetry group, which from now on will be referred to as $\mathrm{U}(1)_{em}$. The complete electroweak interactions are then described by a $\mathrm{SU}(2)_L\times\ \mathrm{U}(1)_Y$ symmetry group with gauge fields $\mathbf{W}^\mu$ and B^μ, from which the physical gauge fields are derived as

$$W_\mu^\pm = \sqrt{\frac{1}{2}}\left(W_\mu^1 \mp iW_\mu^2\right) \qquad \mathrm{W}^\pm \text{ bosons,} \tag{2.30}$$

$$Z_\mu = W_\mu^3\cos\theta_w - B_\mu\sin\theta_w \qquad \mathrm{Z}^0 \text{ boson and} \tag{2.31}$$

$$A_\mu = W_\mu^3\sin\theta_w + B_\mu\cos\theta_w \qquad \text{photon.} \tag{2.32}$$

The couplings are then given by

$$g = \frac{e}{\sin\theta_w} \qquad \text{and } g' = \frac{e}{\cos\theta_w}, \tag{2.33}$$

where θ_w is the Weinberg angle,

$$\cos\theta_w = \frac{m_W}{m_Z}, \tag{2.34}$$

g describes the coupling of the currents J_μ^i to the gauge fields W_μ^i, and g' describes the coupling of j_μ^Y to B_μ. This description is far from being complete and is given in more detail in [12].

As mentioned before, the non-vanishing mass of the weak gauge bosons cannot be introduced by hand into the Lagrangian density, as this would destroy the renormalisability and completely invalidate the theory. This can be solved by the Higgs mechanism, which in the following is described for a simplified Lagrangian density including only electrons and electron neutrinos. The simplification allows for the description of the basic idea of the mechanism, which afterwards can easily be applied to more complex Lagrangian densities, as for example done in [12].

A simple Lagrangian density, including only electrons and electron neutrinos, which is invariant under $\mathrm{SU}(2)_L\times\mathrm{U}(1)_Y$ transformations, is given by

$$\begin{aligned}\mathcal{L}_1 &= \overline{\chi}\gamma^\mu\left(i\partial_\mu - \frac{1}{2}g\tau\cdot\mathbf{W}_\mu + \frac{1}{2}g'B_\mu\right)\chi \\ &+ \overline{e}_R\gamma^\mu\left(i\partial_\mu + g'B_\mu\right)e_R - \frac{1}{4}\mathbf{W}_{\mu\nu}\mathbf{W}^{\mu\nu} - \frac{1}{4}B_{\mu\nu}B^{\mu\nu},\end{aligned} \tag{2.35}$$

where

$$\mathbf{W}_{\mu\nu} = \partial_\mu\mathbf{W}_\nu - \partial_\nu\mathbf{W}_\mu - g\mathbf{W}_\mu\times\mathbf{W}_\nu, \tag{2.36}$$

$$B_{\mu\nu} = \partial_\mu B_\nu - \partial_\nu B_\mu \qquad \text{and} \tag{2.37}$$

$$\chi = \begin{pmatrix} e_L \\ \nu_L \end{pmatrix}. \tag{2.38}$$

Neither the fermionic nor the bosonic fields included in this Lagrangian density get a mass term, as both is incompatible with the requirement of local gauge invariance. Nevertheless, by adding a second term to (2.35), the boson and fermion masses can be obtained. This term is given by

$$\mathcal{L}_2 = \left| \left(i\partial_\mu - g\mathbf{T}\cdot\mathbf{W}_\mu - g'\frac{Y}{2}B_\mu \right)\phi \right|^2 \underbrace{-\mu^2\phi^\dagger\phi - \lambda(\phi^\dagger\phi)^2}_{V(\phi)}, \tag{2.39}$$

in which two additional complex scalar fields, constituting an isospin doublet

$$\phi = \begin{pmatrix} \phi^+ \\ \phi^0 \end{pmatrix} = \sqrt{\frac{1}{2}} \begin{pmatrix} \phi_1 + i\phi_2 \\ \phi_3 + i\phi_4 \end{pmatrix}, \tag{2.40}$$

with hypercharge Y = 1 have been introduced. Now, if $\mu^2 < 0$ and $\lambda > 0$, $V(\phi)$ has a minimum at

$$|\phi|^2 = -\frac{\mu^2}{\lambda}. \tag{2.41}$$

This means, that the vacuum expectation value of the field ϕ is not zero, but there is a hypersphere in the ϕ_i-space with non-vanishing radius that minimizes $V(\phi)$. By choosing a specific value for the ϕ_i, namely

$$\phi_1^2 = \phi_2^2 = \phi_4^2 = 0, \qquad \phi_3^2 = v^2 = -\frac{\mu^2}{\lambda}, \tag{2.42}$$

and only looking at small perturbations $h(x)$ from this value, i.e.

$$\phi(x) = \sqrt{\frac{1}{2}} \begin{pmatrix} 0 \\ v + h(x) \end{pmatrix}, \tag{2.43}$$

the $\mathrm{SU}(2)_L \times \mathrm{U}(1)_Y$ symmetry is spontaneously broken. The ground state does not reflect the symmetry. This is referred to as electroweak symmetry breaking (EWSB). Nevertheless, the pure $\mathrm{U}(1)_{em}$ symmetry is conserved, as the chosen ground state for ϕ is neutral. If this ground state is put into (2.40), the mass terms for the heavy gauge bosons emerge:

$$m_W = \frac{1}{2}vg, \tag{2.44}$$

$$m_Z = \frac{1}{2}v\sqrt{g^2 + g'^2}, \tag{2.45}$$

$$m_A = 0, \tag{2.46}$$

whereas the latter identity reflects the remaining invariance of the Lagrangian density under $\mathrm{U}(1)_{em}$ transformations. For the fermion masses, in the present case only the electron's mass, another term has to be added to the Lagrangian density. This term is

$$\mathcal{L}_3 = -G_e \left(\chi^\dagger \phi e_R + \overline{e_R}\phi^\dagger\chi \right). \tag{2.47}$$

where

$$G_e = \sqrt{2}\frac{m_e}{v}. \tag{2.48}$$

If quarks are considered as well their mass is generated by the Higgs field ϕ in a very similar way. There is one difference, which becomes important if the theory is made supersymmetric

(see chapter 2.2). For the up-type quarks, a second Higgs doublet needs to be created, which in the SM is essentially given by the hermitian conjugate of ϕ, namely

$$\phi_c = -i\tau_2\phi^*. \tag{2.49}$$

So far, it was described how all interactions between particles in the SM can be derived from the requirement of local gauge invariance under appropriate phase transformations. Furthermore, weak and electromagnetic interactions can be unified, such that the SM is a $\mathrm{SU}(3)_{colour}\times$ $\mathrm{SU}(2)_L\times$ $\mathrm{U}(1)_Y$ gauge theory. The fact that the gauge bosons of the weak interaction are massive requires the introduction of a Higgs field. By a specific choice of the non-vanishing vacuum expectation value of this field, the $\mathrm{SU}(2)_L\times$ $\mathrm{U}(1)_Y$ symmetry is spontaneously broken and the masses for all massive fermions and bosons are generated. In the next chapter, another important feature of the SM is shortly described.

2.1.2 Renormalisation and the Running of Physical "Constants"

If higher order corrections to electron-muon scattering are considered, one of the Feynman diagrams to be taken into account is shown in Figure 2.2(b). If the matrix element for this diagram is calculated, it can be shown that the addition of it to the matrix element of the scattering process shown in Figure 2.2(a) is effectively a modification of the photon propagator, namely

$$-i\frac{g_{\mu\nu}}{q^2} \rightarrow -i\frac{g_{\mu\nu}}{q^2} - \frac{I_{\mu\nu}}{q^4}, \tag{2.50}$$

where

$$I_{\mu\nu} = -ig_{\mu\nu}q^2 I\left(q^2\right) + q_\mu q_\nu J\left(q^2\right). \tag{2.51}$$

In this expression for the correction to the photon propagator, the latter term vanishes when the propagator couples to external currents. Now

$$I\left(q^2\right) = \frac{\alpha_{em}}{3\pi}\left\{\lim_{\Lambda_C\rightarrow\infty}\ln\left(\frac{\Lambda_C^2}{m_f^2}\right) - 6\int_0^1 z(1-z)\log\left(1-\frac{q^2z(1-z)}{m_f^2}\right)dz\right\}, \tag{2.52}$$

which is logarithmically divergent with the introduced *cutoff* Λ_C. In (2.52), m_f refers to the mass of the fermion in the loop.

Without considering the limit for a moment, the matrix element for electron-muon scattering including one loop corrections can be written as

$$\mathcal{M} = -4\pi\alpha_{em}j^e_{em}\frac{g_{\mu\nu}}{q^2}\left\{1-\frac{\alpha_{em}}{3\pi}\left[\ln\left(\frac{\Lambda_C^2}{m_f^2}\right) - f\left(-q^2\right)\right]\right\}j^\mu_{em}, \tag{2.53}$$

$$\approx -4\pi\alpha^R_{em}j^e_{em}\frac{g_{\mu\nu}}{q^2}\left\{1+\frac{\alpha^R_{em}}{3\pi}f\left(-q^2\right)\right\}j^\mu_{em}, \tag{2.54}$$

where the *renormalised* coupling constant

$$\alpha^R_{em} = \alpha_{em}\left(1-\frac{\alpha_{em}}{3\pi}\ln\left(\frac{\Lambda_C^2}{m_f^2}\right)\right) \tag{2.55}$$

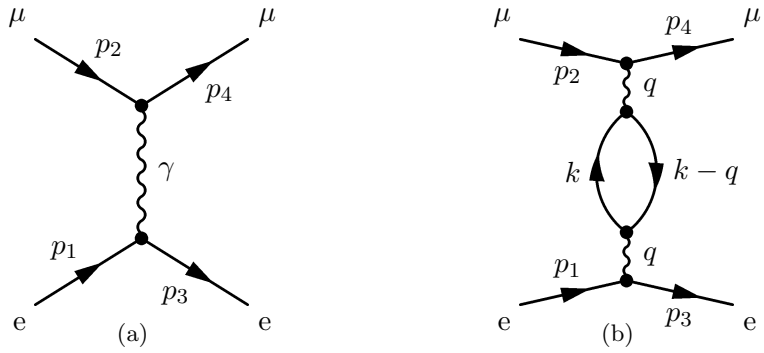

Figure 2.2: (a) Tree level diagram for electron-muon scattering via t-channel photon exchange. (b) A loop-diagram for electron-muon scattering. The exchanged photon splits into a fermion-antifermion pair, which reannihilates to the same photon. If this diagram is included in the calculation of the matrix element, the matrix element diverges. Effectively, the inclusion is a change in the photon propagator, such that the divergence can be absorbed in renormalised coupling constants.

has been introduced and terms $O(\alpha_{em}^3)$ have been omitted. The infinities arising from loop-diagrams like the one shown in Figure 2.2(b) by sending the cutoff Λ_C to infinity are absorbed in the renormalised coupling constant. Whenever this is possible, a theory is called renormalisable, which is a crucial requirement for a quantum field theory, because non-renormalisable theories do not have any prediction power.

Thus, couplings which appear in tree level diagrams receive higher order corrections, which can be separated into an infinite and a finite part. The infinite part can be absorbed by a reinterpretation of the coupling constant. What remains is a finite correction of the form $f\left(-q^2\right)$. This can as well be absorbed into the coupling constant, which actually makes the constant a function of the momentum transfer q^2, given by

$$\alpha_{em}^R(q^2) = \alpha_{em}^R(0) \cdot \left(1 + \frac{\alpha_{em}^R(0)}{3\pi} f(-q^2)\right). \tag{2.56}$$

The dependence of the coupling "constant" on the momentum transfer is indicated by the term *running coupling*. The effect can be explained in an illustrative way at least for electromagnetic interactions: The reasons for the running of the coupling are higher order corrections, which in principle reflect vacuum polarisation and therefore charge screening. Different effective charges are seen when measuring from different distances, i.e. at different energies.

The couplings, i.e. the charges, are not the only properties of a particle which need to be renormalised, or reparameterised. There are also loops which lead to renormalised masses and magnetic moments. It can be shown that, in addition, these diagrams do not contribute to the renormalisation of the coupling constant (Ward identity). This ensures, that the charge correction for particles of the same *bare* charge but different mass are exactly the same. The finite corrections arising from diagrams with n loops are always proportional to $\left(\alpha_{em}^R(0)\right)^{n+1}$, in the electromagnetic case. However, loop corrections need to be taken into account for all interactions.

The exact behaviour of the renormalised quantities with respect to the momentum transfer is described by the so-called Renormalisation Group Equation (RGE):

$$\frac{\partial \alpha}{\partial Q} = \frac{1}{Q}\beta(\alpha), \tag{2.57}$$

where the transferred momentum $\sqrt{q^2}$ has been replaced by Q, and α denotes the renormalised quantity. The dependence of α on Q is defined by the so-called beta function $\beta(\alpha)$. Beta functions yielding the correction terms for n loops are then called n-loop-beta functions. The one-loop beta function for quantum electrodynamics is given by

$$\beta(\alpha_{em}^R) = \frac{2\alpha_{em}^R}{3\pi}, \tag{2.58}$$

which yields

$$\alpha_{em}^R(Q) = \frac{\alpha_{em}^R(Q_0)}{1 - \frac{2\alpha_{em}^R(Q_0)}{3\pi} \ln\left(\frac{Q}{Q_0}\right)}, \tag{2.59}$$

where a reference value Q_0 has to be chosen to get rid of the cutoff Λ_C. In the renormalisation procedure, the value $\alpha_{em}^R(Q_0)$ is subtracted from $\alpha_{em}^R(Q)$. The one-loop beta function for the strong coupling α_s in a theory with n_f flavours is given by

$$\beta(\alpha_s) = -\left(11 - \frac{2n_f}{3}\right)\frac{\alpha_s^2}{2\pi} \tag{2.60}$$

$$\Rightarrow \quad \alpha_s(Q) = \frac{\alpha_s(Q_0)}{1 + \frac{\alpha_s(Q_0)}{12\pi}(33 - 2n_f)\ln\left(\frac{Q^2}{Q_0^2}\right)}. \tag{2.61}$$

2.1.3 Shortcomings of the Standard Model

The Standard Model has been extremely successfull over decades in the precise prediction of experimental results. Nevertheless, there are strong indications that it is not a complete theory of nature.

The Higgs particle, as introduced in the last section, is a fundamental scalar and receives mass corrections from loop diagrams. If the Feynman diagram shown in Figure 2.3 is considered, it can be shown that the corresponding correction is in principle given by

$$\delta m_H^2 \propto \lambda \Lambda_C^2. \tag{2.62}$$

In this formula, m_H^2 is the mass of the Higgs, i.e. $m_H^2 = 2\mu^2$ with μ taken from (2.39). This correction is quadratically divergent with the cutoff Λ_C. By electroweak precision data, a Higgs mass at the order of 100 GeV is strongly favored [5]. If no new physics is assumed to exist below the Planck scale $M_P \sim 10^{19}$ GeV, Λ_C was of the same order as M_P, as the *bare* Higgs mass had to be, as well, in order to obtain the physical mass of ~ 100 GeV. Thus enormous cancellations are necessary, which seems "unnatural". This *fine-tuning* would affect all other particles, as well, since their masses are generated by their couplings to the Higgs field. This rather aesthetical flaw of the SM is referred to as the hierarchy problem.

Another issue is the unification of the gauge couplings at high scales. Electric and magnetic forces are unified in the electromagnetic interaction, which is unified with the weak interaction in the electroweak model. It is somehow expected that in a similar sense the strong force can be unified with the electroweak force, such that all three forces are different manifestations of one fundamental interaction. This *grand unification* is mostly expected to happen at scales $> 10^{15}$ GeV. If the measured SM gauge couplings are extrapolated to these scales, such a unification does not appear, as illustrated in Figure 2.4. At even higher scales, gravity might be included and unified with the other forces, which can neither be provided by the SM, as it does not even contain a quantum theory of gravity.

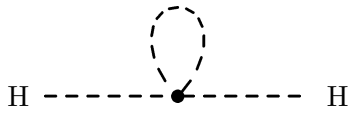

Figure 2.3: A bosonic loop correction to the Higgs mass. In the SM, these Feynman graphs do not have an opposite sign counterpart, which leads to quadratic divergences in the calculation of the Higgs mass. This is known as the hierarchy problem, as the integrals for the loop corrections are typically carried out up to the Planck scale and the Higgs mass is expected at the order of 100 GeV by electroweak precision data, such that the Higgs mass had to be fine-tuned in a way that seems unnatural.

There are 25 parameters in the Lagrangian of the SM, such as masses and mixing angles. These parameters are not predicted, but they rather need to be determined by experiment. Thus, the SM does not explain why the masses and couplings are exactly what they are. For example, the charge of a proton (net quark content uud) exactly cancels the charge of an electron. The SM does not offer an answer to the question why this is the case.

In addition, it does not explain why the amount of matter in the universe exceeds the amount of antimatter, as it is assumed that this asymmetry was not an initial condition of the universe. There are processes in the SM which clearly distinguish between matter and antimatter, like the leptonic decay of the long-lived neutral kaon, but these are not sufficient to explain the asymmetry quantitatively.

The last point to be mentionend here is the existence of Dark Matter and Dark Energy. The COBE and WMAP experiments showed that the total amount of visible matter in the universe makes up only 5% of its overall energy content [19, 20]. About 20% Dark Matter and 75% Dark Energy dominate the universe. Dark Matter can only be detected indirectly, e.g. by microlensing effects. Any particles it is made of must interact weakly (if at all) or via gravity only. In addition, in order to explain the large scale structure of the universe, Dark Matter needs to be cold, i.e. non-relativistic. It must therefore consist of weakly interacting massive particles (WIMPs). The only particles in the SM which undergo only weak interactions are neutrinos. Due to their very low mass (O(eV)), they are relativistic and hence cannot be considered as Cold Dark Matter. Black holes and brown dwarfs are also not sufficient to explain the assumed amount of Dark Matter. As in addition the nature of Dark Energy is completely speculative, the SM does not offer an explanation for 95% of our universe.

2.2 Supersymmetry

In the first section of this chapter, the fundamental importance of symmetries for the SM has been pointed out. In particular, the claim for local gauge symmetry assures the photon to be massless, such that from diagrams like the one shown in Figure 2.5(a) only logarithmic divergences arise. These can be absorbed in renormalised constants, preserving the theory's prediction power. Chiral symmetry for $m \to 0$ ensures the same for the electron self energy, as shown in Figure 2.5(b). Thus, the masses of fundamental spin-1/2 particles and vector bosons are "protected" from quadratic divergences. But there is no such symmetry in the SM that "saves"

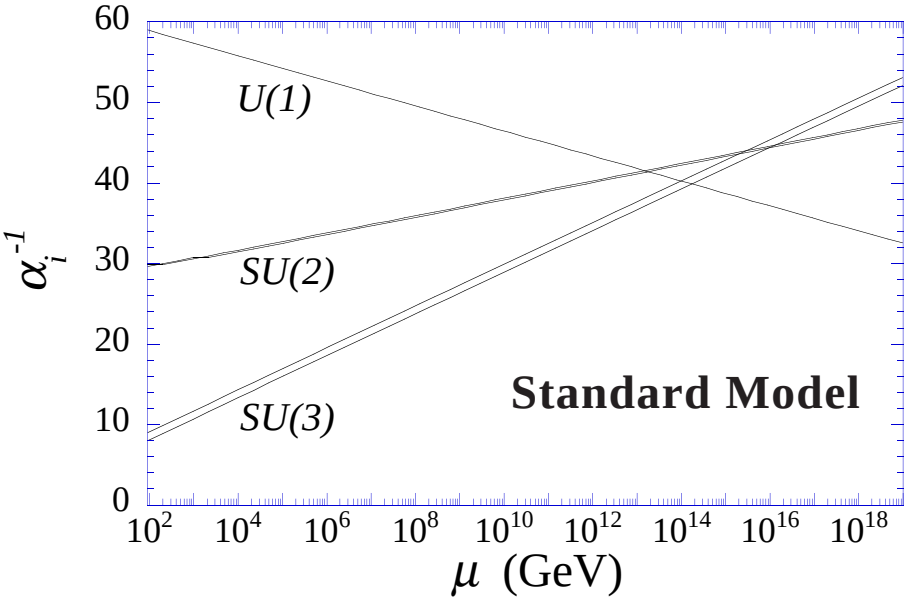

Figure 2.4: The running of the gauge-couplings in the Standard-Modell. If the SM was valid up to energies at which quantum gravity is believed to provide significant contributions (10^{16} GeV), there would be no unification of the gauge-couplings. Although no strict reason can be given, it seems somehow uncomfortable that a unification does not appear at some high scale.

the masses of fundamental scalars like the Higgs in a similar way. If a symmetry connecting scalars with fermions or vector bosons existed, the "protection" for fundamental scalar masses would be restored.

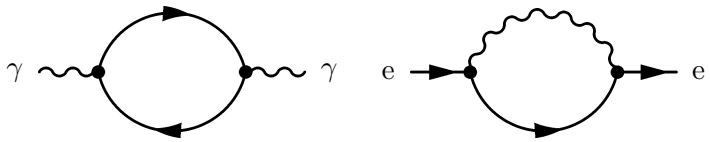

(a) (b)

Figure 2.5: One-loop diagrams giving rise to mass corrections for a photon (a) and an electron (b). For both particles, symmetries ensure the absence of quadratic divergences.

The question is, if such a symmetry can be realised in nature. It was shown by Coleman and Mandula, that the only charges generating a symmetry transformation in a consistent 4-dimensional theory, are Lorentz scalars or elements of the Poincaré group [21]. Now Lorentz scalars do not affect the spin of a field when applied to it, and neither do the elements of the Poincaré group, such that a symmetry between scalars and fermions or vector bosons seems to be ruled out by the Coleman-Mandula theorem. As a matter of fact, this is not true, if charges with spinorial Lorentz transformation behaviour are considered, as stated by the Haag-Lopuszanski-Sohnius theorem [22]. If such generators Q_a act on a particle field, the spin of

this field is altered by 1/2, and if furthermore a series of other requirements is fulfilled, such a symmetry would finally provide cancellations of the quadratic divergences in the calculation of the masses of fundamental scalars. Supersymmetry (SUSY) is exactly that kind of a symmetry, although the hierarchy problem was clearly not the motivation that lead to the intense theoretical examination of this new symmetry.

This short discussion of supersymmetry is mainly based on [11, 23, 24].

2.2.1 The SUSY Algebra

SUSY connects fermionic and bosonic degrees of freedom. If a SUSY transformation Q acts on a fermionic field, a bosonic field with the same quantum numbers except for the spin of course, is obtained and vice versa:

$$Q|\text{boson}\rangle = |\text{fermion}\rangle, \tag{2.63}$$
$$Q|\text{fermion}\rangle = |\text{boson}\rangle. \tag{2.64}$$

Information about any symmetry can be obtained by looking at its associated algebra and the irreducible representations of this algebra. Algebras associated to the "classical" symmetries are Lie algebras, which only contain bosonic generators and whose Lie bracket is the commutator. When fermionic generators are taken into account, the Lie bracket is the anticommutator. If, like SUSY, a symmetry connects bosonic with fermionic fields, Lie superalgebras need to be considered, which include both types of generators. The (anti)commutation relations for the SUSY generators Q_a and the space-time transformation generators P_μ are given by

$$\{Q_a, Q_b\} = \{Q_a^\dagger, Q_b^\dagger\} = 0, \tag{2.65}$$
$$[Q_a, P_\mu] = [Q_a^\dagger, P_\mu] = 0, \tag{2.66}$$
$$\{Q_a, Q_b^\dagger\} = (\sigma^\mu)_{ab} P_\mu. \tag{2.67}$$

The irreducible group representations of the SUSY algebra are chiral and gauge supermultiplets, containing both fermionic and bosonic fields. The bosonic field in a supermultiplet is referred to as the superpartner of the respective fermionic field (and vice versa). The commutation relation (2.66) implies

$$\left[Q_a, P^2\right] = 0, \tag{2.68}$$

which means that the particles in a supermultiplet have the same masses.

Although the focus in the next chapters will be on phenomenological aspects of SUSY, the connection between SUSY and space-time transformations via (2.67) needs to be emphasised in a few words. If SUSY, with generators Q_a, existed, the concept of 4-dimensional spacetime had to be extended to include 'fermionic' degrees of freedom. Although the implementation of SUSY necessitates the introduction of new particles, as will be described in the next chapters, this extension of spacetime is the most radical implication of a supersymmetric theory.

2.2.2 A Basic SUSY Lagrangian Density

In this chapter only the final formulae for a supersymmetric theory are quoted, where the notation of [24] is used. A more detailed and complete deduction of the formulae can be found in [11, 23, 24], for example. After this short formal summary, in the next chapter more phenomenological aspects of the Minimal Supersymmetric Standard Model (MSSM) are pointed out.

For chiral supermultiplets, consisting of left chiral fermionic fields χ_i, and complex scalar fields ϕ_i, the changes in the fields when applying a SUSY transformation are given by

$$\begin{aligned} \delta\phi_i &= \epsilon\chi_i, && (2.69)\\ \delta\left(\chi_i\right)_\alpha &= -i\left(\sigma^\mu\epsilon^\dagger\right)_\alpha D_\mu\phi_i + \epsilon_\alpha F_i, && (2.70)\\ \delta F_i &= -i\epsilon^\dagger\overline{\sigma}^\mu D_\mu\chi_i + \sqrt{2}g\left(T^a\phi\right)_i\epsilon^\dagger\lambda^{\dagger a}. && (2.71) \end{aligned}$$

For a gauge multiplet, consisting of a SM gauge field A^a_μ and its superpartner λ^a_α, the respective transformations are

$$\begin{aligned} \delta A^a_\mu &= -\frac{1}{\sqrt{2}}\left(\epsilon^\dagger\overline{\sigma}_\mu\lambda^a + \lambda^{\dagger a}\overline{\sigma_\mu}\epsilon\right), && (2.72)\\ \delta\lambda^a_\alpha &= \frac{i}{2\sqrt{2}}\left(\sigma^\mu\overline{\sigma}^\nu\epsilon\right)_\alpha F^a_{\mu\nu} + \frac{1}{\sqrt{2}}\epsilon_\alpha D^a, && (2.73)\\ \delta D^a &= \frac{i}{\sqrt{2}}\left(-\epsilon^\dagger\overline{\sigma}^\mu D_\mu\lambda^a + D_\mu\lambda^{\dagger a}\overline{\sigma}^\mu\epsilon\right), && (2.74) \end{aligned}$$

in which

$$F^a_{\mu\nu} = \partial_\mu A^a_\nu - \partial_\nu A^a_\mu + g f^{a\beta\gamma}A^\beta_\mu A^\gamma_\mu, \tag{2.75}$$

with the structure constants $f^{\alpha\beta\gamma}$. The non-propagating fields F and D, not to be confused with the covariant derivative D_μ, have to be introduced to restore degrees of freedom balance between the SM fields and their respective superpartners. These auxiliary fields can be completely expressed as functions of the scalar fields ϕ_i.

For the complete Lagrangian density, in addition to the gauge interactions, interactions involving the gaugino and D fields have to be taken into account. All interactions are then determined by the gauge groups and the so-called superpotential W, which is an analytical, complex function of the involved scalar fields and contains additional Yukawa couplings. A complete Lagrangian density for a renormalisable supersymmetric theory containing chiral and gauge multiplets is then given by

$$\begin{aligned} \mathcal{L} &= -\partial^\mu\phi^{*i}\partial_\mu\phi_i + i\chi^{\dagger i}\overline{\sigma}^\mu\partial_\mu\chi_i - \frac{1}{2}\left(W^{ij}\chi_i\chi_j + W^*_{ij}\chi^{\dagger i}\chi^{\dagger J}\right) - W^iW^*_i\\ &- \frac{1}{4}F^{a\mu\nu}F^{\mu\nu a} + i\lambda^{\dagger a}\overline{\sigma}^{mu}D_\mu\lambda^a + \frac{1}{2}D^aD^a\\ &- \sqrt{2}g_a(\phi^{*i}T^a\chi_i)\lambda^a - \sqrt{2}g_a\lambda^{\dagger a}(\chi^{\dagger i}T^a\phi_i) + g_a(\phi^{*i}T^a\phi_i)D^a. \end{aligned} \tag{2.76}$$

In this formula, the T^a denote the generators of the gauge transformations with the coupling constants g_a.

One implication of the anticommutation relations (2.67) is the extension of the concept of space-time to include fermionic degrees of freedom, which are referred to as θ and θ^* here, following the convention of [23]. This allows for the formulation of a supersymmetric theory in terms of superfields, which are used only for the formulation of the MSSM superpotential in this thesis. Therefore, only the definition of a superfield is given here. For a supermultiplet, containing a left chiral fermionic field $\chi_i(x)$ and a bosonic field $\phi_i(x)$, the corresponding superfield is given by

$$\Phi_i(x,\theta) = \phi_i(x) + \theta\chi_i(x) + \frac{1}{2}\theta\theta F_i(x). \tag{2.77}$$

2.2.3 The MSSM and the Resolution of SM Shortcomings

It was stated above, that, apart from the spin, the superpartner of a given field must have the very same quantum numbers as the field itself. It is therefore not possible to combine only SM particles to supermultiplets, which means that in a supersymmetric model new fields have to be introduced. The superpartners of the SM fermion fields are called s(calar)fermions, whereas the superpartners of the gauge bosons and the Higgs bosons are called gauginos (Higgsinos). As in supersymmetric theories Yukawa interactions must not contain a complex scalar field and its hermitian conjugate, two independent Higgs doublets are needed to give masses to the up-type and down-type quarks. The complete particle content of the MSSM is shown in Tables 2.3 and 2.4, and in Figure 2.6.

The superpotential for the MSSM is given by

$$W_{MSSM} = \overline{u}\mathbf{y_u}QH_u - \overline{d}\mathbf{y_d}QH_d - \overline{e}\mathbf{y_e}LH_d + \mu H_u H_d, \tag{2.78}$$

where the superfields as specified in Table 2.3 are used and family indices are implicitly included. The Yukawa matrices $\mathbf{y_i}$ define the masses and CKM mixings of the quarks and leptons, and are mostly chosen to be zero except for the (3,3) component, due to the high masses of the third generation particles in the SM. The superpotential (2.78) does not allow for lepton or baryon number violation, although such terms could be introduced without spoiling gauge invariance or SUSY. In order to avoid an a priori postulation of the conservation of these quantum numbers

Name	Symbol	spin 0	spin 1/2
squarks/quarks	Q	$(\tilde{u}_L,\, \tilde{d}_L)$	$(u_L,\, d_L)$
	$\overline{u}$	$\tilde{u}^*_R$	$\tilde{u}^\dagger_R$
	$\overline{d}$	$\tilde{d}^*_R$	$\tilde{d}^\dagger_R$
sleptons/leptons	L	$(\tilde{\nu}_L,\, \tilde{e}_L)$	$(\nu,\, e_L)$
	$\overline{e}$	$\tilde{e}^*_R$	$e^\dagger_R$
Higgs, Higgsinos	H_u	$(\, H^+_u,\, H^0_u\,)$	$(\, \tilde{H}^+_u,\, \tilde{H}^0_u\,)$
	H_u	$(\, H^0_d,\, H^-_d\,)$	$(\, \tilde{H}^0_d,\, \tilde{H}^-_d\,)$

Table 2.3: The chiral supermultiplets in the MSSM. In this minimal supersymmetric extension to the SM, each SM fermion is assigned to a bosonic (scalar) superpartner. In the table, the supersymmetric partner of a SM fermion f is labelled $\tilde{f}$. Although the sfermions' chirality is not defined, they "inherit" this index (R or L) from their SM partners. As the neutrinos are regarded to be massless, only one sneutrino per SM neutrino (the $\tilde{\nu}_L$), is introduced. Finally, the Higgses and their superpartners, the Higgsinos complete the set of chiral multiplets in the MSSM. These are the only chiral multiplets, whose SM particles are scalars, while their superpartners are fermions, as shown in the Table.

Name	spin 1/2	spin 1
gluino/gluon	$\tilde{g}$	g
winos/W bosons	$\tilde{W}^\pm,\, \tilde{W}^0$	$W^\pm,\, W^0$
bino/B boson	$\tilde{B}^0$	B^0

Table 2.4: The gauge supermultiplets in the MSSM. The fundamental force carriers are grouped together with their supersymmetric spin 1/2 partners and as for the SM fermions, the MSSM superpartners of the SM bosons are labelled with a $\sim$.

by hand, which is not necessary in the SM, a new conserved, multiplicative quantum number, namely R-parity, is introduced. This number is defined by

$$R = (-1)^{3(B-L)+2s}, \tag{2.79}$$

where B is the Baryon number, L the lepton number and s the spin. Squarks, sleptons, gauginos and Higgsinos, from now on referred to as sparticles, therefore have odd R-parity (-1), while their SM superpartners have even R-parity (+1). If R-parity was conserved, terms violating L and B would be eliminated in the Lagrangian density. Furthermore, the lightest supersymmetric particle (LSP) would be stable, it could only be produced in pairs at collider experiments, and an odd number of LSPs would occur in any sparticle decay chain. Another consequence of R-parity conservation is the stability of the proton, which would decay very quickly if the respective Yukawa couplings were at the order of unity and R-parity was violated.

SUSY elegantly solves many of the known shortcomings of the SM. First to be mentioned here is the hierarchy problem. The quadratic divergences in the calculation of the masses of fundamental scalars in a supersymmetric theory can be expressed as

$$\delta m^2 \sim \left(\lambda_{scalar} - g^2_{fermion}\right) \Lambda^2_C, \tag{2.80}$$

where essentially

$$\lambda_{scalar} = g^2_{fermion}, \tag{2.81}$$

i.e. the quadratic divergences arising from scalar loop corrections are exactly cancelled by the loop corrections including their fermionic superpartners. Two loop diagrams which cancel out each other are shown in Figure 2.7.

Furthermore, if R-parity is conserved, the LSP might be an excellent candidate for Cold Dark Matter. This requires it to be massive, colourless and electrically neutral. In many models, the LSP is the lightest neutralino, which fits these requirements perfectly. A detailed analysis of supersymmetric Dark Matter is provided in [25].

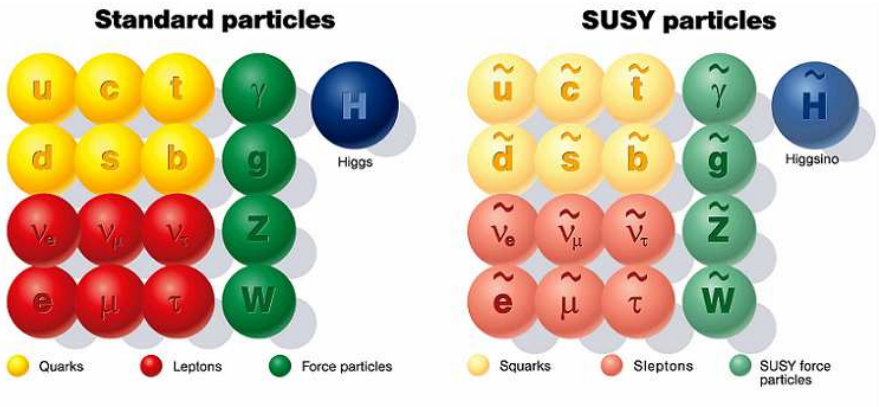

Figure 2.6: The particle content of the MSSM. Except for the Higgs, all SM particles, which are shown on the left hand side, have already been discovered, while their superpartners on the right hand side remain undetected, so far. The particle content shown here is the minimal particle content of any supersymmetric extension to the SM. In principle, for each particle of the SM, a new, supersymmetric version has to be introduced.

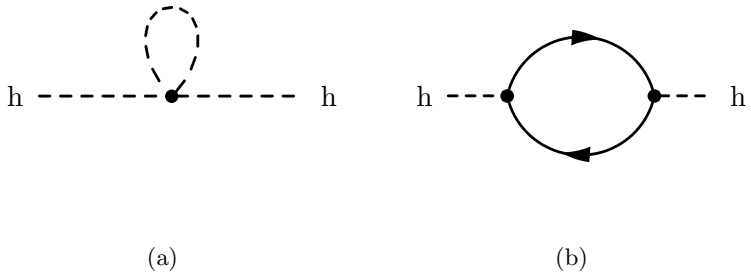

Figure 2.7: A (a) bosonic and (b) fermionic loop contribution to the Higgs mass. From both diagrams, quadratic divergences arise if the calculation of the Higgs mass is carried out. If the boson and fermion appearing in the above Feynman diagrams were superpartners of each other, their divergences would cancel out each other, such that the Higgs mass would remain finite without any fine-tuning.

The next issue SUSY solves is the unification of the gauge couplings at scales $m_U \approx 10^{16}$ GeV. This is shown in Figure 2.9.

Now, due to (2.68), SUSY cannot be an exact symmetry, as none of the sparticles has been experimentally observed, yet. If SUSY is realised in nature, it is therefore expected to be spontaneously broken, i.e. the symmetry is invisible in the vacuum state. Nevertheless, there is no evidence on how SUSY might spontaneously be broken, such that terms are added to the Lagrangian density by hand which explicitly break SUSY. In fact, the actual SUSY breaking must take place in a hidden sector, which interacts very weakly only with the visible MSSM sector. SUSY breaking is mediated between these two sectors by some flavour blind interaction, as illustrated in Figure 2.8. The soft SUSY breaking terms in the Lagrangian density are then usually considered as a low energy parametrisation of the ignorance of the exact SUSY breaking mechanism. There are strong restrictions to these terms, as they must not spoil renormalisability, Lorentz invariance or gauge invariance. A Lagrangian density for a model with explicitly broken SUSY is then given by

$$\mathcal{L} = \mathcal{L}_{SUSY} + \mathcal{L}_{soft}, \tag{2.82}$$

in which $\mathcal{L}_{SUSY}$ is the unbroken SUSY Lagrangian density (2.76) and $\mathcal{L}_{soft}$ contains the SUSY breaking terms. The attribute *soft* refers to the fact that in addition to the mentioned restrictions on the breaking terms, these terms should neither reintroduce quadratic divergences in the calculation of loop diagrams, which requires them to be of positive mass dimension. Only terms leading to corrections of the form

$$\delta m^2 \sim m_{soft}^2 \log\left(\frac{\Lambda_C}{m_{soft}}\right), \tag{2.83}$$

in which m_{soft} is the scale for the soft SUSY breaking terms, may remain. For the solution of the hierarchy problem, $m_{soft} \sim 1$ TeV is strongly favoured. Although the constraints on the SUSY breaking terms are rather strict, more than 100 parameters are needed to describe them in their most general form, and no explanation for the mass scale m_{soft} is provided by the theory.

The allowed soft SUSY breaking terms for the MSSM can be divided into five sectors. Four of these sectors contain mass terms for the gauginos, squarks, sleptons and Higgses, and the last

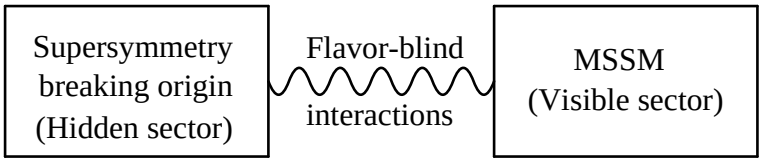

Figure 2.8: An illustration of the SUSY breaking mechanism. The actual breaking of the symmetry is assumed to take place in some hidden sector (left hand side), which is not directly accessible. Via flavour blind interactions, the SUSY breaking is mediated to the visible sector on the right hand side. There are various ideas of how the breaking could be mediated. The most famous scenarios feature anomaly mediated (AMSB), gauge mediated (GMSB) or gravity mediated (mSUGRA) SUSY breaking.

contains triple scalar couplings, such that essentially

$$\begin{aligned}\mathcal{L}_{soft} = \; & -\; \frac{1}{2}\left(M_3\tilde{g}\tilde{g} + M_2\tilde{W}\tilde{W} + M_1\tilde{B}\tilde{B} + h.c.\right) \\ & -\; \tilde{Q}^\dagger \mathbf{m_Q^2}\tilde{Q} - \tilde{L}^\dagger \mathbf{m_L^2}\tilde{L} - \tilde{\bar{u}}\mathbf{m_{\bar{u}}^2}\tilde{\bar{u}}^\dagger - \tilde{\bar{d}}\mathbf{m_{\bar{d}}^2}\tilde{\bar{d}}^\dagger - \tilde{\bar{e}}\mathbf{m_{\bar{e}}^2}\tilde{\bar{e}}^\dagger \\ & -\; m_{H_u}^2 H_u^* H_u - m_{H_d}^2 H_d^* H_d - (bH_u H_d + h.c.) \\ & -\; \left(\tilde{\bar{u}}\mathbf{a_u}\tilde{Q}H_u - \tilde{\bar{d}}\mathbf{a_d}\tilde{Q}H_d - \tilde{\bar{e}}\mathbf{a_e}\tilde{L}H_d + h.c.\right), \end{aligned} \tag{2.84}$$

where *h.c.* means the hermitian conjugate. These terms include the masses and mixings between the sparticles. As an example, the gluino mass is essentially given by M_3. For the Higgsinos and the winos/bino, which are the superpartners of the electroweak gauge bosons, this is not the case. For non-zero vacuum expectation values (vev) of the neutral scalar Higgs fields, mixings between the neutral Higgsinos and the bino/winos are generated by EWSB and the μ-terms in the Lagrangian density. As a consequence, the gauge eigenstates of these particles are not their (physical) mass eigenstates. The masses of these mass eigenstates can be determined by diagonalizing the respective mass matrices. For the neutral Higgses, the wino and the bino, the mass eigenstates are called neutralinos. The neutralino mass matrix is given by

$$\mathbf{M}_{\tilde{\chi}^0} = \begin{pmatrix} M_1 & 0 & -c_\beta s_W m_Z & s_\beta s_W m_Z \\ 0 & M_2 & c_\beta c_W m_Z & -s_\beta c_W mZ \\ -c_\beta s_W m_Z & c_\beta c_W m_Z & 0 & -\mu \\ s_\beta s_W m_Z & -s_\beta c_W m_Z & -\mu & 0 \end{pmatrix}, \tag{2.85}$$

where $\tan\beta = v_u/v_d$ is the ratio of the vevs of the two Higgs doublets, and $c_\beta = \cos\beta$, $s_\beta = \sin\beta$, $c_W = \cos\theta_W$, $s_W = \sin\theta_W$. The quantity $\tan\beta$ can be calculated from the parameters in the Lagrangian, but it is mostly used as a parameter itself, replacing one of the other parameters. The matrix (2.85) can be diagonalised by unitary matrices $\mathbf{N}$, and the mass eigenstates $\tilde{\chi}_i^0$ are calculated from the gauge eigenstates via

$$\begin{pmatrix} \tilde{\chi}_1^0 \\ \tilde{\chi}_2^0 \\ \tilde{\chi}_3^0 \\ \tilde{\chi}_4^0 \end{pmatrix} = \mathbf{N} \begin{pmatrix} \tilde{B} \\ \tilde{W}^0 \\ \tilde{H}_d^0 \\ \tilde{H}_u^0 \end{pmatrix}. \tag{2.86}$$

In principle, the same can be applied to the charged gaugino/Higgsino sector, but this time two distinct matrices are needed for the diagonalisation of the chargino mass matrix, as this

matrix is not orthogonal. For the sfermion sector the situation is even more complicated in the MSSM. Generation and flavour mixing terms are in principle allowed by the theory, which would introduce complex 6×6 mixing matrices in the charged slepton and the squark sectors.

Although the unbroken SUSY Lagrangian density contains only one additional parameter, namely the Higgs mass parameter μ, in the broken case a total of 105 additional parameters are put into the Lagrangian density via (2.84). However, by experiments, there are strong restrictions on all parameters, which by making certain assumptions, allow for a dramatic reduction of the dimension of the parameter space, partly corresponding to a substantial simplification of mixing matrices. One such a model is the minimal supergravity (mSUGRA) model.

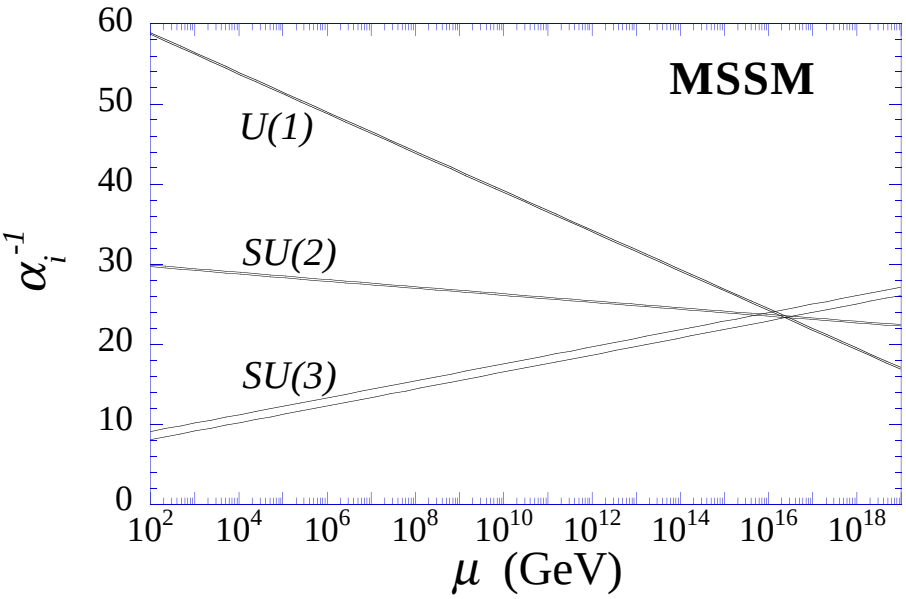

Figure 2.9: The diagram shows the running of the gauge-couplings in the MSSM. Within their theoretical uncertainties, the three coupling constants are unified at energy scales $\gtrsim 10^{16}$ GeV. The exact value depends on the actual breaking mechanism and the parameters of the SUSY Lagrangian density. The unification of the gauge couplings at a high-scale is one of the convincing arguments to consider SUSY seriously. However, there is no evidence that such a unification has to appear in nature, but it seems nicer to a certain extend.

2.2.4 The mSUGRA Model

In the mSUGRA model SUSY breaking is mediated between the hidden and the visible sector via gravity. This introduces non-renormalisable terms in the effective Lagrangian density, which are suppressed by the Planck mass M_P, however. By assuming a 'minimal' form for certain terms in that Lagrangian density, the dimensionality of the MSSM parameter space is broken down to 5.

One of the remaining parameters is the ratio of the Higgs vevs, $\tan\beta$. The sparticle masses are covered by only two parameters, reflecting the unification of all gaugino masses and all sfermion masses at a high scale, typically referred to as GUT (Grand Unified Theory) scale.

These parameters, m_0 and $m_{1/2}$, are connected to the MSSM parameters by

$$M_3 = M_2 = M_1 = m_{1/2} \qquad \text{at GUT scale,} \tag{2.87}$$

$$\mathbf{m}^2_{\tilde{\mathbf{Q}}} = \mathbf{m}^2_{\tilde{\mathbf{u}}} = \mathbf{m}^2_{\tilde{\mathbf{d}}} = \mathbf{m}^2_{\tilde{\mathbf{L}}} = \mathbf{m}^2_{\tilde{\mathbf{e}}} = m_0^2\mathbf{1} \qquad \text{at GUT scale,} \tag{2.88}$$

in which $\mathbf{1}$ is the unit matrix. Furthermore

$$m^2_{H_u} = m^2_{H_d} = m_0^2. \qquad \text{at GUT scale} \tag{2.89}$$

The fourth parameter A_0 unifies the trilinear couplings at the GUT scale, namely

$$\mathbf{a_u} = A_0\mathbf{y_u}, \mathbf{a_d} = A_0\mathbf{y_d}, \mathbf{a_e} = A_0\mathbf{y_e} \qquad \text{at GUT scale,} \tag{2.90}$$

in which the Yukawa matrices from the superpotential (2.78) occur. The GUT scale is typically in the order of 10^{16} GeV (see figure 2.9). Finally, the fifth parameter is a discrete parameter, namely the sign of the Higgs mass parameter, sign μ, which can only acquire values ± 1 while in principle $A_0 \in \mathbb{R}$, $m_i, \tan\beta \in \mathbb{R}^+$.

Despite their degeneracy at the GUT scale, the sparticles acquire different masses at low (EWSB) scale, $Q_{EWSB} \sim m_Z$, as their charges associated to the gauge interactions differ. If their Yukawa couplings are neglected, the one-loop beta functions for the first and second generation squarks as an example are given by

$$Q\frac{dm^2_{\tilde{Q}_{1,2}}}{dQ} = \left(-\frac{32}{3}\alpha_3 M_3^2 - 6\alpha_2 M_2^2 - \frac{2}{15}M_1^2\right)/4\pi, \tag{2.91}$$

$$Q\frac{dm^2_{\tilde{u}_{1,2}}}{dQ} = \left(-\frac{32}{3}\alpha_3 M_3^2 - \frac{32}{15}M_1^2\right)/4\pi, \tag{2.92}$$

where the *rescaled* gauge couplings

$$\alpha_1 = \frac{5}{3}\frac{g'^2}{4\pi}, \tag{2.93}$$

$$\alpha_2 = \frac{g^2}{4\pi} \qquad \text{and} \tag{2.94}$$

$$\alpha_3 = \frac{g_s^2}{4\pi} \tag{2.95}$$

have been used. The most general form for the sfermion masses at Q_{EWSB} in the mSUGRA model is thus given by

$$m^2_{\tilde{f}_i} = m_0^2 + \kappa_1^i K_1 + \kappa_2^i K_2 + \kappa_3^i K_3, \tag{2.96}$$

where the coefficients κ_j^i depend on the gauge quantum numbers of the fermion, and the K_j are positive values with $K_j \sim m^2_{1/2}$. As the slepton masses do not receive corrections by strong interaction loops, i.e. $\kappa_3^{\tilde{l}} = 0$, the squarks are generally heavier then the sleptons. It is for essentially the same reason, that the superpartners of right chiral SM fermions are lighter than the respective partners of the left chiral SM particles, as the former do not interact weakly in contrast to the latter. The calculation for the third generation sfermions are more complex, as additional terms due to their non-vanishing Yukawa couplings enter in the beta functions. These induce a mixing between the left chiral and right chiral superpartners of the top quark, the bottom quark and the tau lepton, such that in contrast to the first and second generation,

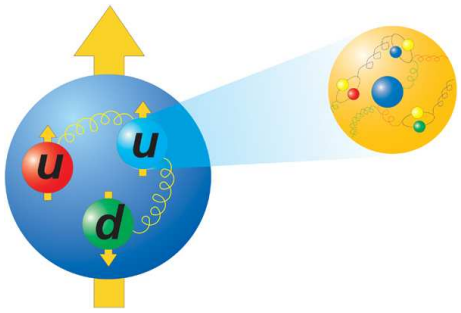

Figure 2.10: The proton structure. At low energies (i.e. at high distances), the proton seems to be a pointlike particle with electric charge +1. However, deep inelastic scattering experiments at the Stanford Linear Accelerator Center (SLAC) and the Deutsches Elektronen-Synchrotron (DESY) revealed the substructure of the proton, which if examined at not too high energies, seems to consist of two up quarks and one down quark, which are kept together by the strong interactions via gluons (left side of the Figure). The spin of the proton and its quark constituents is illustrated with an arrow here. If the distance is decreased, a dynamic amount of sea-quarks and gluons becomes visible, as depicted on the right hand side.

the mass eigenstates are not the gauge eigenstates $\tilde{f}_R$ and $\tilde{f}_L$. The mass eigenstates are usually referred to as $\tilde{f}_1$ and $\tilde{f}_2$ in these cases, and information about the actual mixing is mathematically fixed in mixing matrices, as usual. In the stau and sbottom sector, the mixing mainly depends on $\tan\beta$, while the large value of m_{top} dominates the mixing in the stop sector. Beta functions for the gaugino masses and the Yukawa couplings can be found in [23, 24], and will not be quoted here.

Finally a short summary of SUSY phenomenology at hadron colliders, especially at proton-proton colliders is given in the following. Protons are bound states of three valence quarks and a fluctuating number of sea quarks and gluons, see Figure 2.10, such that the main production mechanisms for sparticles at proton-proton colliders are strong interactions. As in mSUGRA models, due to (2.96), squarks, and for essentially the same reason gluinos, are expected to have masses ~ 1 TeV, high centre of mass energies are needed to produce the sparticles at significant rates.

The dominating Feynman diagrams for sparticle production are shown in Figure 2.11. In most models, the squarks and gluinos are unstable and will very quickly decay via long decay chains with characteristic final states. Two decay chains, which are typical for the models studied in the remainder of the present thesis, are shown in Figure 2.12.

Of course it strongly depends on the exact model of SUSY breaking and the respective parameter values what kind of decays are allowed, and what decays are suppressed. This does not only depend on the actual mass hierarchy, but also on the exact composition of the neutralinos and the heavy flavour squarks and sleptons. For example, the second lightest neutralino in Figure 2.12 might be mainly wino, such that a decay into a right chiral slepton and a lepton is strongly suppressed in comparison to the decay into a left chiral slepton and a lepton, if the latter is kinematically allowed.

It can be deducted from Figure 2.12, that a typical SUSY final state at hadron colliders contains a lot of different particles, namely quarks and gluons which form jets in the detector, charged leptons, neutrinos and, depending on the model, indetectable LSPs. The reconstruction of such decay chains and the extraction of observables is thus quite a complex enterprise, in particular because the production cross sections for SUSY in most scenarios are much lower

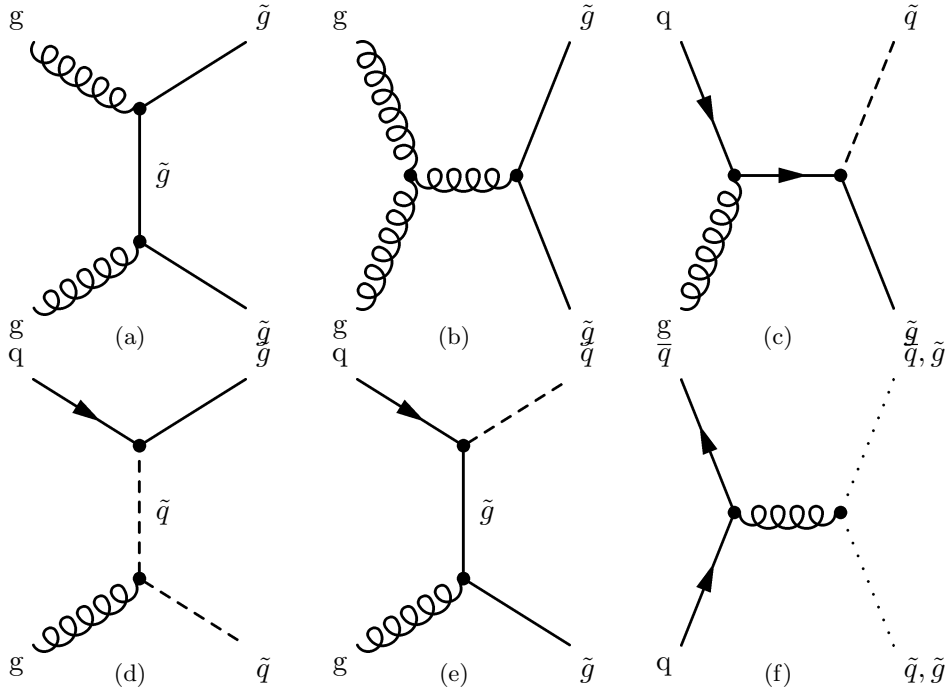

Figure 2.11: SUSY production mechanisms at hadron colliders. Depending on the energy and the type of hadrons used for the collisions, (a) gluon-gluon scattering, (b) gluon-gluon fusion, (c)-(e) quark-gluon scattering or (f) quark-antiquark annihilation will provide the dominant contributions to the total SUSY cross sections. However, the dominant production processes are strong interactions involving t-channel gluino/squark exchange or an s-channel gluon/quark exchange as shown in the Feynman diagrams. There are also possibilities to produce sparticles weakly, but as these mostly play only a minor role at hadron colliders, the respective Feynman diagrams are not shown here.

than those for relevant background processes. A sophisticated detector at a high energy collider is therefore needed in order to discover SUSY experimentally, and precision measurements are needed to find out the actual SUSY breaking mechanism. Before such a collider and detector are introduced, the basic problem of SUSY parameter estimation is now pointed out.

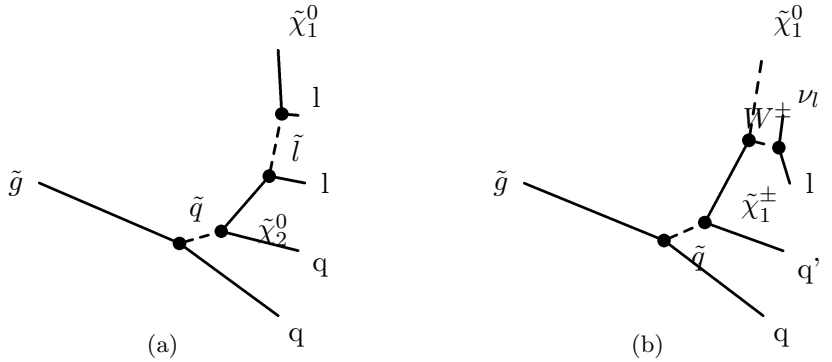

Figure 2.12: Two typical SUSY decay chains at hadron colliders. A gluino is produced, which typically decays into a squark and a quark. As shown in (a), this squark may decay into another quark of the same flavour as the first quark, and and the second lightest neutralino, which may decay into a slepton and a lepton. Finally, the slepton decays into the lightest neutralino, which is the LSP here, and another lepton of the same flavour and opposite charge. In (b), a different decay channel of the squark is shown. Here, it decays into a quark of different flavour and a chargino, which decays into a W and the LSP. Finally, the W may decay hadronically or leptonically (as shown here). In both cases, two jets and a large amount of missing transverse energy, together with one or two leptons would be observed.

3 Introduction to Inverse Problems

In this chapter the problem of extracting model parameters from measured observables is described. A basic introduction given in the first section by means of a simple example from classical mechanics is followed by a brief overview on the extraction of SUSY Lagrangian parameters from possible future experimental data.

3.1 A Simple Example from Classical Mechanics

For a classical, pointlike particle of known mass m, which can move without friction along the x-axis and which is attached to a spring with strength k, the Lagrangian is given by [26]

$$L = E_{kinetic} - E_{potential} = \frac{m}{2}\dot{x}^2 - \frac{k}{2}x^2. \tag{3.1}$$

$$\tag{3.2}$$

This yields the equation of motion [26]

$$m\ddot{x} = -kx. \tag{3.3}$$

The system is sketched in figure 3.1. Given the initial condition

$$x(t=0) = x_{max}, \tag{3.4}$$

the trajectory of the particle is

$$x(t) = x_{max} \cdot \cos(\omega t). \tag{3.5}$$

If the numerical value of the spring constant k is of interest but unknown, the frequency ω can be experimentally determined. It can be connected to the spring constant by inserting (3.5) into (3.3):

$$\begin{aligned} -m\omega^2 x_{max}\cos(\omega t) &= -kx_{max}\cos(\omega t) \\ \Rightarrow k &= m\cdot\omega^2 \end{aligned} \tag{3.6}$$

This equation can be solved uniquely, since the square of ω and the mass m of the particle are uniquely determined. m can be determined before measuring ω by applying a known force and measuring the acceleration of the particle, or by simply calibrating the mass scale by setting $m = 1$ mass unit. Thus, by measuring ω, the spring constant k, which occurs as a parameter in (3.1), can be unambiguously extracted from one measurement. The uncertainty on k can then be calculated from the uncertainties on m and ω. With the knowledge of the numerical value of k, precise predictions can be obtained. For example, the frequency ω' for a particle of mass m' attached to the same spring can be predicted, or the mass m' can be determined by measuring ω'.

Precise knowledge of the value of k is therefore advantageous, and it can be obtained by a one-to-one mapping between the measured observables and the parameter itself as it occurs in

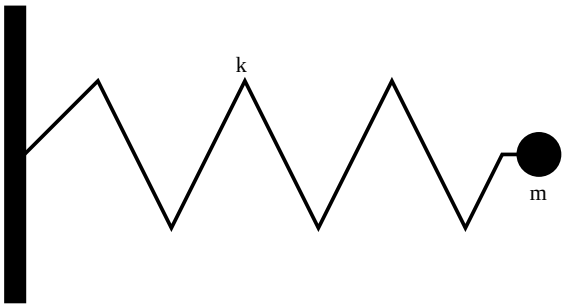

Figure 3.1: A single harmonic oscillator with spring constant k and mass m. The eigenfrequency of this system can be measured, and from the measurement the fundamental parameter k can be deduced.

the Lagrangian (since $\omega \geq 0$ physically, (3.6) is indeed a one-to-one mapping, although it is quadratic in ω).

The same procedure can be applied to a second harmonic oscillator with mass M and spring constant K, where the frequency Ω is measured and the parameter K can be extracted from this measurement. But the situation changes if a physical system like the one shown in figure 3.2 is considered, which is a system of two coupled harmonic oscillators.

A mass m_1 is attached to a wall via a spring with constant k_1 and to a second mass m_2 via a spring with constant k_{12}. The mass m_2 is itself attached to another wall with a spring of strength k_2. If it was possible to measure only the eigenfrequencies of this system, which can be calculated as functions of the parameters m_i, k_i and k_{12} [26],

$$\begin{aligned} \omega_{E,\pm}^2 &= \frac{1}{2m_1m_2}\left(m_1k_2 + m_2k_1 + (m_1+m_2)k_{12}\right) \\ &\pm \sqrt{\frac{1}{4m_1^2m_2^2}\left(m_1k_2 + m_2k_1 + (m_1+m_2)k_{12}\right)^2 - \frac{k_1k_2 + (k_1+k_2)k_{12}}{m_1m_2}}, \end{aligned} \tag{3.7}$$

the three k's cannot be uniquely determined even if m_1 and m_2 are known, since equations (3.7) are not invertable with respect to these. The coupling between the two oscillators has introduced no additional observable but one additional parameter in the Lagrangian. Without further knowledge, these parameters cannot be extracted from the available measurements.

Of course, additional measurements for the coupled oscillators can be easily performed, and the situation is different for the physics discussed in this thesis. But the example shows in principle the nature of the so-called *inverse problems*. Any model describing a given physical system contains a certain number of parameters. All possible measurements in the physical system can then be expressed in terms of the parameters. But the reverse is not always possible, especially when couplings between different sectors of the physical system are introduced. In addition, most inverse problems in physics can not be solved by simply increasing the number of measurements until it equals the number of parameters in the model. Highly non-linear equations show up, which further complicate the extraction of the correct parameters.

Nevertheless, there are ways to extract the parameters if enough experimental data is collected. One approach, which is referred to as a bottom-up-scenario [27], uses approximations to exploit invertable first-order relations, for example. In some cases, the parameter space and the observables can be separated into independent subspaces, such that to first order any couplings between the subsectors can be set to zero. The actual entanglement of the subsectors is then

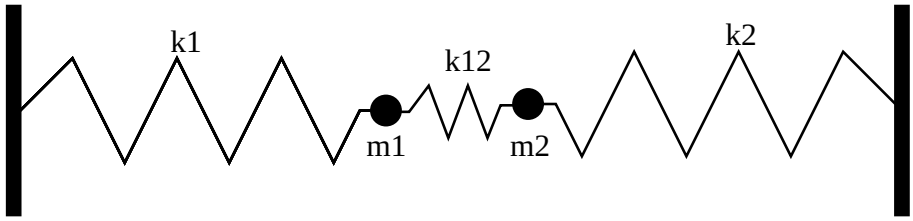

Figure 3.2: Two harmonic oscillators, which are coupled via a third spring. As the system shown in this figures has only two eigenmodes, the available measurements do not suffice to determine the parameters at a first view.

taken into account in an iterative way. In the above example, if the coupling k_{12} is small, it can be neglected in the first step of the calculation. Then, the values for k_1 and k_2 can be extracted, as ω_1 is only connected to k_1 in this case, but not to k_2 and vice versa. With the first order values, in an iterative procedure more accurate determinations taking into account non-vanishing values of k_{12} are obtained.

Another approach is a so called top-down scenario [27]. Given some reasonably chosen start values for the parameters, the corresponding values for the observables are computed and compared to the actual measurement. By using adequate fitting procedures, the parameter values describing the measurements best can be extracted.

When such techniques are applied in order to determine the parameters of a given physics model, there is always a risk to take wrong decisions. Especially if the parameter space is high-dimensional, there might exist more than one set of parameters that describe the given set of observables well within the experimental and theoretical uncertainties. The results obtained by following a top-down approach may then vary significantly if different start values are used.

3.2 The Inverse Problem for SUSY

The parameter space of the MSSM is a paradigm for a high-dimensional parameter space. In addition to the SM parameters, the MSSM Lagrangian contains more than 100 free parameters. The mass spectrum of the SUSY particles, their couplings, mixings and branching fractions, which partly constitute the set of physical quantities that are measured at collider experiments, can definitely be calculated from these parameters. In practice, since the calculation is done only to finite order, there are, of course, theoretical uncertainties on the computed values.

The inverse calculation cannot be done directly, especially when some masses, couplings and branching fractions are unknown and the uncertainties on the measured observables are large. At tree level, the parameter space and the observable space can partly be divided into uncoupled subspaces, but once loop corrections are included, the mass of a particle can only be calculated by taking into account nearly all parameters via mainly non-linear relations [27].

SUSY has not been observed experimentally, yet, such that the reconstruction of the parameters of a supersymmetric Lagrangian density has not been performed on direct SUSY measurements, yet. Nevertheless, if SUSY is realised in nature, the typical mass scale for sparticles is expected be in the order of 1 TeV, which means that observables directly related to SUSY will be available from present and future experiments at the Large Hadron Collider (LHC) [28–30] and the planned International Linear Collider (ILC) [31–34]. In a certain sense the situation is then similar to the one described in the first section of this chapter. Knowledge about the parameters of the SUSY Lagrangian, corresponding to the values of k_1, k_2 and k_{12} would help

to make predictions, one of which is the fraction of supersymmetric cold dark matter in the universe. For the determination of these parameters, the observables provided by the experiments at the LHC and ILC can be used, like the frequencies $\omega_{E,\pm}$. Since SUSY is an extension to the SM, the complete Lagrangian would contain the SM parameters as well. Fits of the Lagrangian strongly benefit from prior knowledge about these parameters, which is available from previous experiments. The strong and electromagnetic coupling constants α_s and α_{em} are examples for such parameters, and although the analogy is of course not perfect, this corresponds to the masses m_1 and m_2 in the first section of this chapter. Using tree level estimates is on par with setting $k_{12} = 0$, whereas taking into account loop corrections would be analogous to setting k_{12} to non-zero values.

Once enough observables have been measured with a sufficient precision, they can be used for fits of SUSY Lagrangians. In R-parity conserving SUSY models with a dark matter candidate LSP, this is always produced in pairs at the LHC and the ILC and escapes the experiments undetected. In addition, full information about the initial state is not available for the proton-proton collisions at the LHC, because protons have a substructure and it is actually the constituents of the proton (quarks and gluons) which are scattered. This makes direct measurements of sparticle masses difficult. Other observables, which are accessible more easily, are being examined. Edges in the spectra of detectable decay products can be expressed in terms of the sparticle masses. These edges, as well as shapes of the respective distributions, production rates and ratios of branching fractions provide a fair basis for an extraction of the Lagrangian parameters.

If a top-down approach is being followed, programs are needed to predict the values of these observables for a given set of parameter values. Approximations and initial estimations need to be done during the calculation of the predictions and as different programs handle these approximations and estimations in a different way, they provide similar but not exactly equal predictions, thus leading to different best-fit parameter values. In order to quote reasonable uncertainties on fit results, amongst other things, these differences have to be studied.

The intention of the study presented in this thesis is to provide a first insight into systematic shifts of best-fit parameters for fits to SUSY Lagrangians with the program *Fittino* [35] when using either *SPheno* [36], *SoftSUSY* [37] or *SuSpect* [38] for the prediction of the SUSY mass spectrum during the fitting procedure.

For this purpose, the measurement of one specific SUSY observable in a best case scenario is studied first. This observable, which is a kinematic endpoint in the invariant mass spectrum of the visible products of a certain sparticle decay chain, together with a number of other toy measurements is then used to fit mSUGRA Lagrangians with each of the three available spectrum calculators, looking for possible problematic parameter regions, i.e. regions with notable differences in results.

4 The LHC and the ATLAS Experiment

4.1 The Large Hadron Collider

The Large Hadron Collider is a hadron-hadron collider, located at the European Organization for Nuclear Research (CERN) near Geneva, Switzerland. Approved by the CERN council in 1994, the construction started in 2000, after the shutdown of the Large Electron Positron Collider (LEP). Making use of LEP's infrastructure, especially the 27 km long circular underground tunnel, the first start-up could be performed in September 2008. The description provided here relies on [28–30].

The machine can accelerate protons to energies up to 7 TeV, using Radio Frequency (RF) cavities. 1,232 superconducting cryodipole magnets, providing a nominal magnetic field of 8.33 T at a current of 11,850 A, bend the protons around the beampipe. The dipoles, based on Nb-Ti Rutherford cables, operate at a nominal temperature of 1.9 K, for which 96 tons of superfluid helium are needed. The focusing of the beam is realised by a number of multipole magnets and the RF cavities.

The given specifications of the LHC allow for proton-proton collisions at a centre of mass energy up to 14 TeV. There are up to 2808 bunches inside the storage ring, divided into one beam circulating clockwise and one beam circulating counterclockwise. Each bunch contains up to $\sim 1.15 \times 10^{11}$ protons. At the maximum luminosity, a bunch crossing occurs every 25 ns at the 8 interaction points (IPs), each of which induces about 20 proton-proton interactions on average. This corresponds to an instantaneous luminosity of 1.0×10^{34} $\mathrm{cm}^{-2}\mathrm{s}^{-1}$. The total cross section expected for 14 TeV proton-proton interactions is 100 mbarn (40 mbarn elastic scattering and 60 mbarn inelastic scattering).

The LHC is not only designed for colliding protons with protons, but also lead ions with lead ions. The Pb^{82+} ions are accelerated up to 2.76 TeV/nucleon leading to a total centre of mass energy of 1,148 TeV. The design luminosity when operating in ion mode is 7×10^{7} $\mathrm{cm}^{-2}\mathrm{s}^{-1}$, with 592 bunches of ions in the ring and a bunch spacing of 100 ns.

The design of the LHC is chosen in a way that enables physicists working at its six major experiments to explore energy regions which were so far unreached under laboratory conditions. ATLAS (A Toroidal LHC ApparatuS) [39, 40] and CMS (Compact Muon Solenoid)[41] are multipurpose detectors, designed for a comprehensive analysis of any kind of inelastic proton-proton interactions. At the energy scale accessible with the LHC, new physics is expected to be discovered. The LHCb (LHC beauty) [42] experiment is designed for b-physics, in which new insights about CP violation and baryon asymmetry may be found, whereas ALICE (A Large Ion Collider Experiment) [43] is a detector focusing on measurements of the quark-gluon plasma which is expected to be experimentally created for the first time in the Pb-Pb collisions, increasing the knowledge about the very early universe. With TOTEM (TOTal Elastic and diffractive cross section Measurement) [44], amongst others measurements, precise information about the LHC luminosity is obtained. Finally, with LHCf (LHC forward)[45], which consists of two smaller detectors positioned near ATLAS, cascades similar to cosmic rays in the atmosphere can be examined under laboratory conditions for the first time. Figure 4.1 shows a schematic overview of the LHC and the associated experiments.

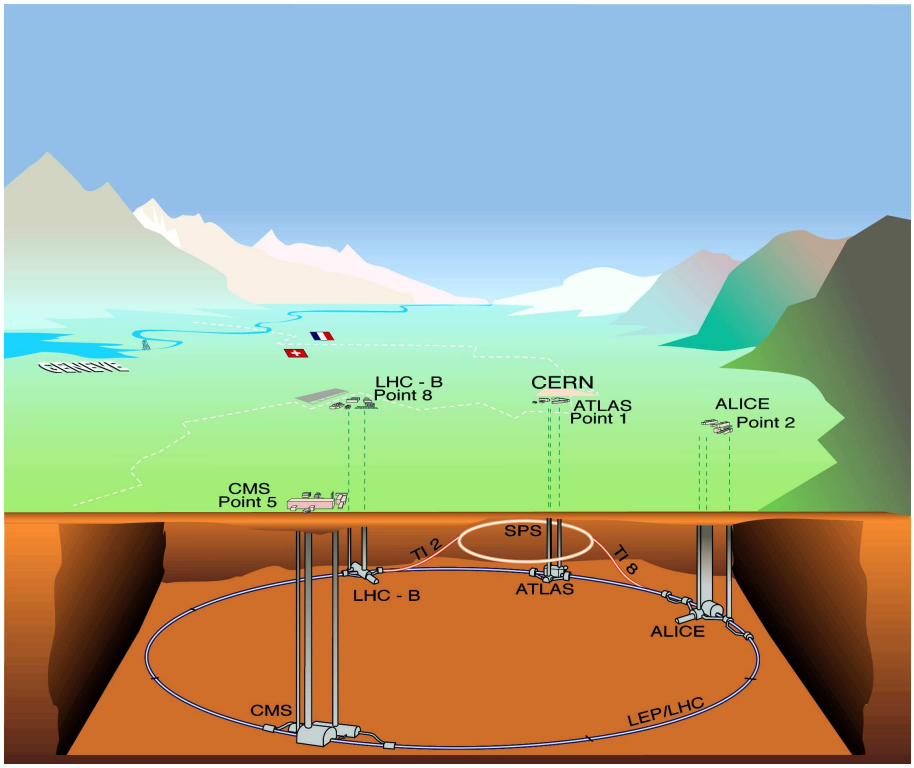

Figure 4.1: An overview of the Large Hadron Collider, situated $\sim$ 100 m underground at CERN, near the city of Geneva in Switzerland. The ring has an overall circumference of about 27 km, most of it lying below French ground. The major experiments ATLAS, CMS, ALICE and LHCb, as well as the Super Proton Synchrotron(SPS), which is an important part of the LHC injection chain, are shown in the figure.

Current Status Due to a malfunctioning bus connection between two magnets and a resulting helium leak, the machine was severely damaged on 19th September 2008 [46]. Repairs and improvements to avoid similar accidents in the future took more than one year. Finally, on November 20th 2009, the first proton beams were back in the LHC, and only three days later, on November 23rd 2009, the first proton proton collisions were recorded at the four main experiments at a centre of mass energy of 900 GeV. A ramp to 2.36 TeV centre of mass energy succeeded little later, and a run at $\sqrt{s} = 7$ TeV is planned for 2010 and 2011 until all major experiments have collected a total amount of 1fb^{-1} of data. Collisions at the design centre of mass energy of 14 TeV are expected by 2013.

4.2 The ATLAS Experiment

The ATLAS detector is one of the two multipurpose experiments at the LHC. It is designed to examine any inelastic proton-proton scattering processes. This includes a rediscovery of already known SM processes like production of the heavy gauge bosons Z^0 and $W^{\pm}$ and top quark pair production, as well as searches for the Higgs boson, supersymmetry, extra dimensions and any other kind of new physics, which is expected to show up at LHC's centre of mass energy. To allow for such analyses, ATLAS must be able to collect information about any (meta)stable particles that might originate from the processes to be studied. Some of these particles, in

particular electrons and muons, can be seen directly in the detector. In contrast, quarks build (unstable) hadronic bound states too quickly to be observed directly. Thus information about coloured particles can only be obtained by looking at hadronic jets in the detector. Finally there are particles which completely escape detection. The only elementary particles which belong to this group and are known so far are the neutrinos. They carry away a certain amount of energy and momentum from the detector, which then misses in the respective balance. In the following, after a short overview, the different subsystems, which capacitate ATLAS to fulfill all these requirements, are explained. The description provided here relies on [39, 40].

4.2.1 Overview

Figure 4.2 shows a scheme of the ATLAS detector with its subsystems. With a length of roughly 46 m, a radius of 22 m and an overall weight of 7,000 tons, ATLAS is the biggest but not heaviest experiment at the LHC. It has a spatial coverage of $\sim 4\pi$ and a typical onion shell design, which allows the detector to meet the requirements mentioned in the last paragraph, as shown in figure 4.3. In the Inner Detector (ID) the tracks of charged particles can be measured accurately. Next to the ID, a solenoid magnet and, behind that, an electromagnetic liquid argon calorimeter (LAr EM calo) are located. Behind that, in the barrel region, the hadronic tile calorimeter (TileCal) is situated. In addition to the barrel calorimeters, an electromagnetic and a hadronic endcap calorimeter are installed. The overall dimensions of ATLAS are defined by the muon chambers, which form the outermost part of the detector. The magnetic fields needed to reconstruct the momenta of charged particles are provided by a central solenoid (CS) for the ID and a system of three toroids for the muon spectrometer. Due to the high luminosity it is impossible to store information about every event and a trigger system is needed to identify and store interesting events.

Before the subsystems of ATLAS are described in more detail, the coordinate system used is

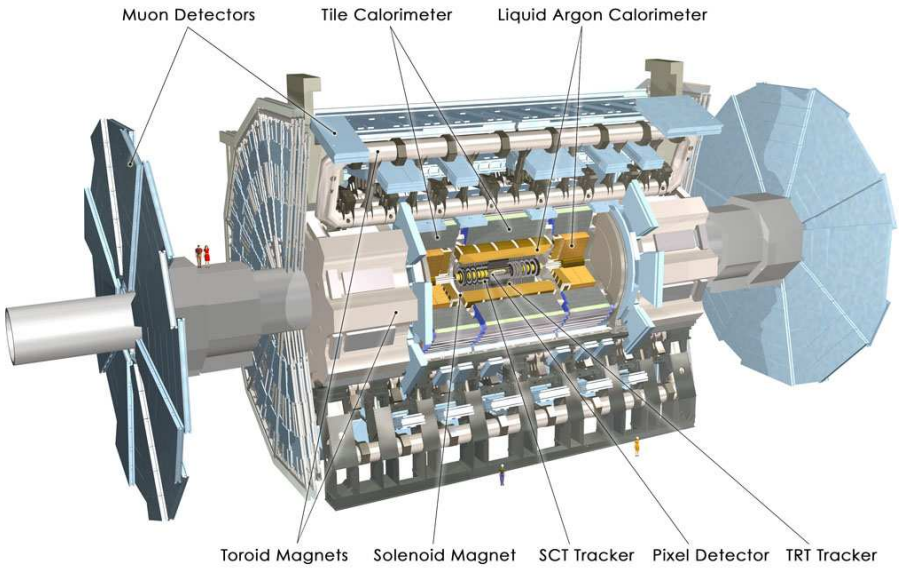

Figure 4.2: An overview of the ATLAS detector. The main subsystems are labelled. Between the left hand side muon detectors and the main barrel of the detector, two persons are shown to illustrate the enormous dimensions of the experiment.

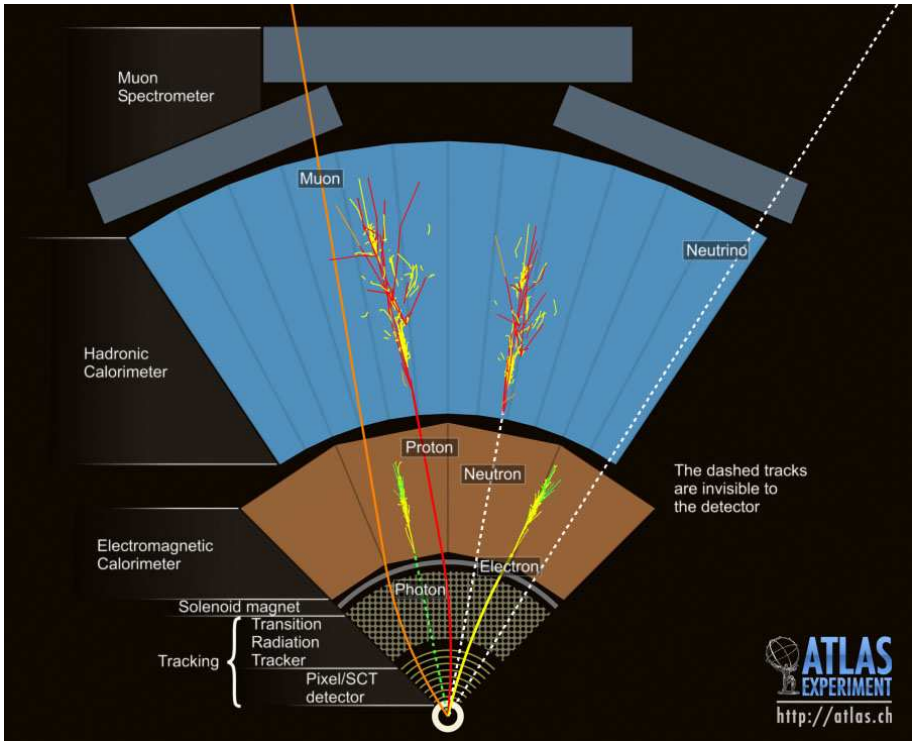

Figure 4.3: This schematic picture illustrates how the onion shell structure of modern multi-purpose detectors allows for the reconstruction of nearly all known (semi)stable particles. Dashed lines denote invisibility of particles in the respective detector parts. As shown, an electron leaves hits in the tracker and creates an electromagnetic shower in the electromagnetic calorimeter. If such a shower is found in the calorimeter without an associated track, it is most likely to originate from a photon. Charged hadrons can be identified by entries in the electromagnetic and hadronic calorimeters with an associated track in the inner detector, while neutral hadrons only deposit their energy in the hadronic calorimeter. This is exemplarily shown for a proton and a neutron, here. Muons, which are stable on the detector scale, are the only particles which are expected to leave tracks in the muon chambers. However, it may happen that the content particles of a jet are not fully stopped in the calorimeter and cause hits in the muon chambers, too (punch through). Of course, as shown here, muons can also be seen by the inner detector, such that for precise muon reconstruction the combined information of the inner tracker and the muon system may be used. The pictures shows also a neutrino, which escapes the detector without leaving any entries in the calorimeters or any tracks.

now explained. The beam going into counterclockwise direction defines the positive z-axis. The positive x-axis points towards the centre of the LHC ring, as the positive y-axis points upwards from the IP. The azimuthal angle ϕ is defined in the range of $[\pi, -\pi]$, with $\phi = 0$ corresponding to the positive x-axis and $\phi = \pi/2$ corresponding to the positive y-axis. Instead of the polar angle θ defined with respect to the positive z-axis, the pseudorapidity $\eta = -\ln\tan\frac{\theta}{2}$ is used, as differences in this variable are Lorentz invariant. Since the initial conditions in hadron-hadron collisions are unknown along the beam axis, projections on the x-y plane are used for some quantities. These are referred to as transverse quantities, like the transverse momentum and energy.

4.2.2 Inner Detector

The purpose of the ID is the accurate vertexing and measurement of tracks and momenta. In order to provide low uncertainties, the ID must have a high granularity, as it is situated next to the IP. In addition, the ID has to be made up of radiation hard material, since the innermost part of it is located at a distance of 5 cm from the beampipe, facing over 300 kGy of ionising radiation and $O(10^{14})$ neutrons per cm^2 in ten years of LHC operation. The ID is divided into a barrel, placed in parallel around the beampipe and one endcap on each side, perpendicular to the z-axis. It has an overall length of 7 m with a radius of 1.15 m.
Three subsystems, as seen in figure 4.4 enable the ID to measure particle tracks and momenta with a high precision. Particles originating from the IP first pass the pixel detector. Behind that, the SemiConductor Tracker (SCT) is located. In addition to these two discrete subdetectors, the outermost part consists of a continuous transition radiation tracker (TRT).

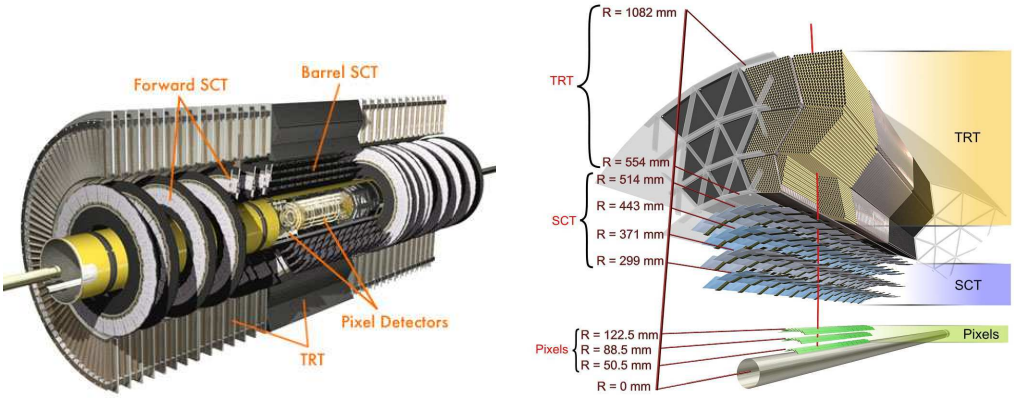

(a) (b)

Figure 4.4: The ATLAS inner detector, which consists of the pixel detector, the semiconductor tracker and the transition radiation tracker. (a) shows a longitudinal cross-section of the ID, while (b) shows a transversal cross-section and the radial distance of the separate detector parts from the beampipe. From both pictures, the relative vicinity of the pixel detector to the beampipe with respect to the other ID subsystems can be seen.

The pixel detector, which is the ID subsystem closest to the beampipe, consists of three layers of silicon n-in-n pixels in the barrel at radii 5 cm, 10 cm and 13 cm, and three additional disks in the endcap region at each side, covering radii from 11 cm to 20 cm. 1,800 modules with a total of 80 million pixels are installed. This high granularity ensures an excellent precision over the covered solid angle. In order to achieve a maximum spatial coverage, bump bonding techniques have been used to connect the active material to the readout electronics. The pixel detector has a resolution of 12 μm in Rϕ for both barrel and disks, and 66 μm (77 μm) in z for the barrel (disks). The pixel detector covers an η-range of ± 2.5.

The second part of the ID, the SCT, consists of four double layer silicon microstrip detectors. One module of the SCT contains four p-on-n silicon detectors. In the barrel, two pairs of wire-bonded, 12.8 cm long strips are attached to another with a respective angle of 40 mrad, with one of them parallel to the beampipe. The pitch between two strips is 80μm. The endcap modules are constructed in a similar way, but with one of the strips being aligned radially. The SCT provides a spatial resolution of 16 μm in Rϕ and 580 μm in the z-direction. It hast 6.2 million readout channels and covers an η-range of ± 2.5 (barrel ± 1.4, endcap wheels $\pm(1.4 - 2.5)$).

Finally, the TRT contains 50,000 straw tubes in the barrel region, and 320,000 radial straws in the endcaps, each of which is 4 mm in diameter and filled with a mixture of CO_2, CF_4 and Xe. Gold-plated W-Re wires ensure a fast response. While the first two parts of the ID make use of the ionisation of depleted silicon by charged particles, the TRT works as a gas tube detector and furthermore exploits another effect. This is the emission of transition radiation when a particle crosses the boundary surface between two materials with different dielectric constants. As the intensity of the transition radiation is different for different types of particles, in particular electrons and pions here, the TRT helps to distinguish between them. Each channel of the TRT has a spatial resolution of 170 μm and two independent detection thresholds to distinguish between tracking hits and actual transition radiation hits. Typically, the TRT measures 36 hits per track, providing good pattern recognition and momentum resolution.

4.2.3 Calorimeters

The ATLAS calorimeter system, whose main purpose is to measure the energy of particles, and which is therefore essential for the determination of the missing transverse energy, consists of four parts. For the detection of electromagnetic interacting particles, in particular electrons and photons, the electromagnetic calorimeter is inbuilt. These particles interact with the detector material, creating a shower of more photons and electrons due to bremsstrahlung and pair production. The electromagnetic calorimeter is made of a barrel part and an endcap on each side. Hadronic particles are measured with the hadronic calorimeters. These are the hadronic barrel calorimeter, the hadronic endcap calorimeters (HEC) and the forward calorimeters (FCAL). As in the electromagnetic calorimeter, due to interactions between the passing hadrons and the detector material, particle showers develop in the hadronic calorimeter. However, the physical processes for energy deposition here are completely different with respect to electromagnetic energy deposition. Since the passing particles interact with the atomic nuclei in the hadronic calorimeter, a high energy deposition of the hadrons is achieved by using detector material with a high Z.

The LAr EM calo, situated next to the CS, consists of accordion shape lead plates and Kapton electrodes. Electromagnetically interacting particles create showers when passing through the lead plates, which ionize the liquid argon. Because of the capacitive coupling between the electrodes and the ionisation charge, the latter can be measured and is read out in intervals of 25 ns. The EM calo, as the subsystems of the ID, is divided into a barrel part and two endcaps on each side. The barrel covers a range of $\eta \leq 1.475$ while the endcaps can measure particles in the range of $1.375 \leq \eta \leq 2.5$ (inner end-cap) or rather $2.5 \leq \eta \leq 3.2$ (outer end-cap). The barrel is divided into two parts, each covering one hemisphere of the detector, both being separated from another by a gap of 6 mm.

The two half-barrels have a thickness of more than 24 radiation lengths (more than 26 for the endcaps). As precision physics is intended to be done for $\eta \leq 2.5$, the LAr EM calo is split into three longitudinal sections. Narrow strips with a pitch of roughly 4 mm constitute the strip section, which has a constant thickness of ~ 6 X_0 with respect to η. This section provides good position measurements in η and improves particle identification. The second section of the LAr EM calo is segmented into towers with a size of $\Delta\eta \times \Delta\phi = 0.025 \times 0.025$. It extends to a thickness of 24 X_0. The final section varies in thickness (2 X_0 to 12 X_0) and is divided into parts of $\Delta\eta = 0.05$. The granularity is coarser in the endcaps, since these are mainly used for jet reconstruction and $\not{E}_T$ measurements. A presampler is used for the regions in which the upstream material in front of the calorimeter exceeds 2 X_0 to account for energy losses in this material.

The resolution of the LAr EM calo, which is made up of a sampling term, a constant term and a noise term, is expected to be approximately 1.6% for moderate photons over the whole η-coverage, or better. For low-energy electrons, a resolution of 5% in the barrel and 3% in the endcaps is expected. In figure 4.5 the EM Cal is shown together with the other parts of the ATLAS calorimetry system.

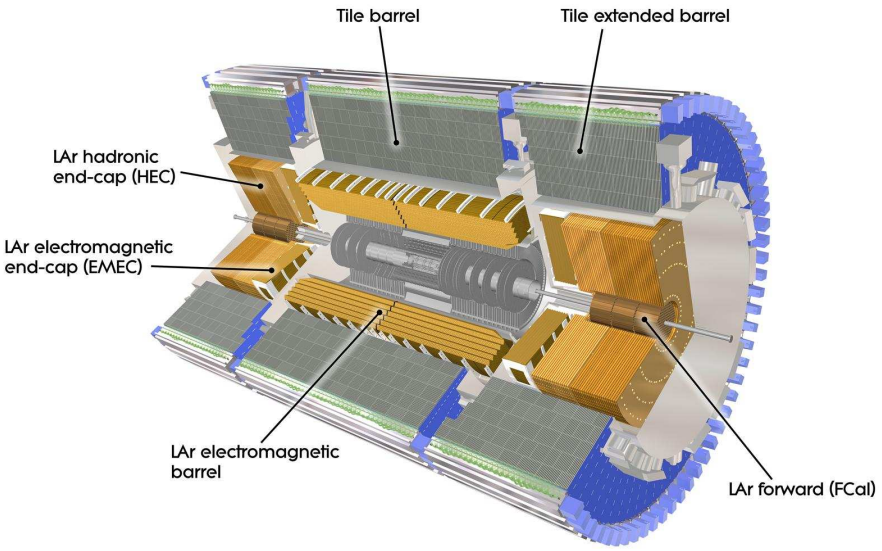

Figure 4.5: The ATLAS calorimeters. The different parts of the calorimeter systems allowing for the measurement of the energies of electrically charged particles and hadrons are labelled.

The hadronic barrel calorimeter is a sampling calorimeter which uses scintillating plastic tiles as active material, and iron as the absorber material. Light pulses are emitted, when charged particles cross the scintillators, which are quickly read out by wavelength shifting fibres into photomultipliers with a low dark current and rise/transmit times in the order of nanoseconds. The TileCal is divided into three parts, one barrel and two extended barrels. With a granularity of $\Delta\eta \times \Delta\phi = 0.1 \times 0.1$ (except for the last layer, where $\Delta\eta \times \Delta\phi = 0.2 \times 0.1$) and a thickness of 11 interactions lengths at $\eta = 0$, the TileCal covers an η-range of ± 1.7 and allows for good resolution of high energetic jets and for low punch through.

The liquid argon HECs measure hadronic energy deposition for $1.5 \leq \eta \leq 3.2$. There are two wheels per side, which use copper plates as absorber material. Each of the four HEC wheels is composed of 32 identical modules. With increasing η, the HEC become coarser in terms of $\Delta\eta \times \Delta\phi$ (0.1×0.1 for $1.5 \leq \eta \leq 2.5$ and 0.2×0.2 for $2.5 \leq \eta \leq 3.2$).

Finally, at a distance of 4.7 m from the IP, the FCAL covers a range of $3.1 \leq \eta \leq 4.9$. Three sections, one made of copper, the other two of tungsten, work as absorber material, while once again liquid argon is used as the sensitive medium. The FCAL has a granularity of $\Delta\eta \times \Delta\phi = 0.2 \times 0.2$.

The performance of the hadronic calorimeters is expected to be

$$\frac{\sigma_E}{E} \approx \frac{2}{E[\text{GeV}]} \oplus \frac{62.4\%}{\sqrt{E[\text{GeV}]}} \oplus 1.7\% \tag{4.1}$$

for jets, whereas the numerators on the RHS are actually not constant for all jet compositions.

4.2.4 Muon System

With a mass of roughly 106 MeV, muons are more than 200 times heavier then electrons. Typical lepton momenta at the LHC are in the order of $1 - 100$ GeV, which means that the muons produced in pp-collisions are minimum ionizing particles (MIP). As a consequence, they pass the ATLAS detector leaving only small amounts of energy in its calorimeters, while all electrons are stopped in the electromagnetic (or at the latest in the hadronic) calorimeter. Since nearly all other particles deposit all their energy in the calorimeter cells as well, muons are the only charged particles known so far, that pass through the whole detector without being stopped. Ionisation chambers outside the calorimeter system can therefore be employed to gain information about muons in addition to the respective hits in the ID.

As they constitute the outer part of ATLAS, the muon chambers define its overall dimensions. The muon system consists of three cylindrical layers concentric with the beam axis, the outermost being located at a radius of about 10 m. Four disks at each side of the barrel region cover the high η regions, the last one being located at a distance of roughly 23 m from the IP.

The muon chambers are not only used for precision measurements of muon momenta, but also for triggering on muon events with well defined p_T cuts. For these two purposes, four different detector technologies are employed, as indicated in figure 4.6. Cathode strip chambers (CSC) and monitored drift tubes (MDT) are used for the precision measurements, while the trigger parts are made of resistive plate chambers (RPC) and thin gap chambers (TGC).

The MDTs cover a range of $0.05 \leq \eta \leq 2$. They consist of aluminium tubes with a diameter of 30 mm, a thickness of 400 μm and varying lengths between 0.7 m and 6.3 m. Signals due to ionisation of the used mixture of 93% Ar/7% CO_2 are transported via 50 μm diameter W-RE wires, which provide a single resolution of 80 μm. The name of the MDTs derives from

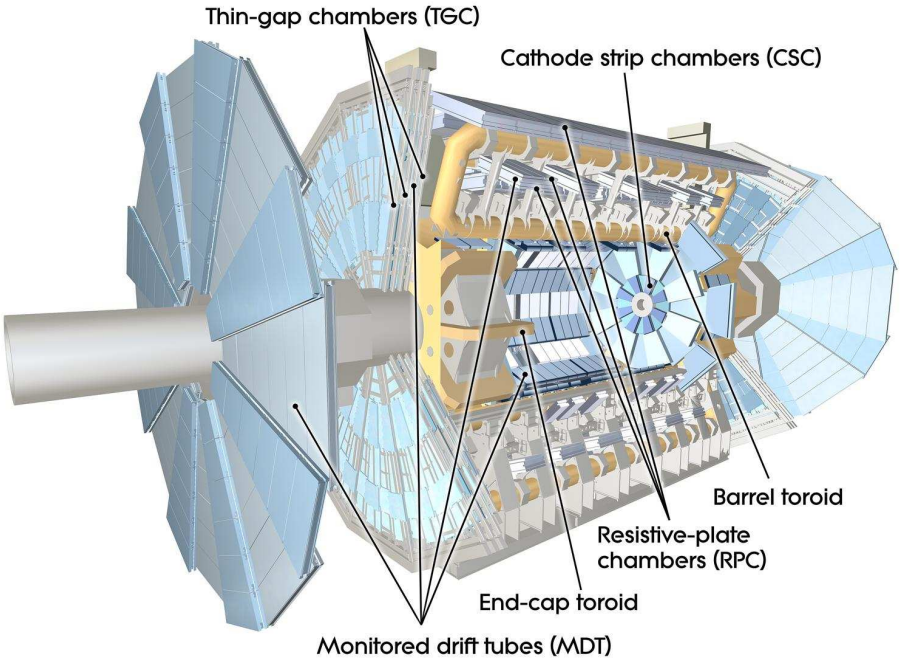

Figure 4.6: This is a scheme of the ATLAS muon systems. The figure shows the arrangement of the CSCs, TGCs, RPCs and MDTs. Furthermore, the toroid magnets for the bending of the muon tracks are labelled.

the optical monitoring of their alignment. Deformations after installation are measured by an in-plane optical system, such that they can be corrected for in the offline analysis.

To meet the higher radiation rates for larger η, CSCs are used for this region ($2 \leq \eta \leq 2.7$). These are multiwire proportional chambers, whose good spatial resolution is ensured by the segmentation of the readout cathode and charge interpolation between neighbouring strips. Spatial precision of more than 60 μm is achieved, as well as good timing resolution (7 ns) and low neutron sensitivity. A total of 1.1 m^3 of an $Ar/CO_2/CF_4$ is used in the CSCs.

The RPCs used for trigger issues are detectors operating with a mixture of SF_6 and $C_2H_2F_4$ between two parallel resistive bakelite plates. In an electric field of 4.5 kV/mm ionisation charges develop into avalanches, which produce electric pulses of typically 0.5 pC. Two coordinates are measured with two orthogonal rectangular layers, one being parallel to the MDTs, the other perpendicular to it.

Finally the second part of the muon trigger system in ATLAS are the TGCs. They operate with a total of 16 m^3 of a gaseous mixture of CO_2 and n-C_5H_{12}. In principle, the TGCs are multiwire proportional chambers, except that the distance between the cathode and anode is smaller than the anode wire pitch. The TGCs provide an excellent ageing behaviour in addition to a good time resolution due to short drift times.

The performance of the muon chambers strongly depends on η and ϕ, as can be seen in figure 4.7. Values between 2% and 10% are obtained for a nominal value of $p_T = 100$ GeV.

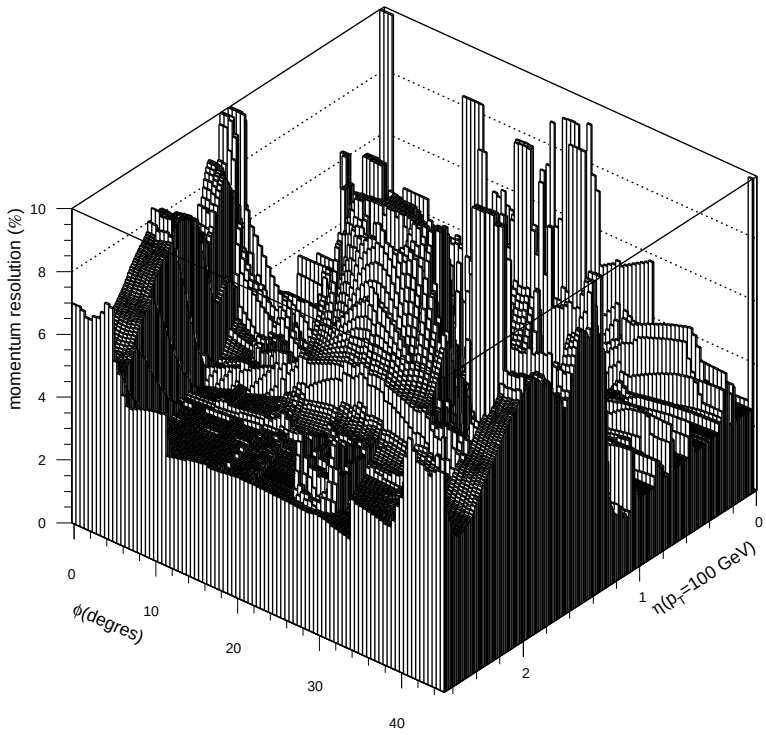

Figure 4.7: The expected performance of the ATLAS muon system. As this two-dimensional histogram indicates, for a transverse momentum of 100 GeV, momentum resolutions between $\sim 2\%$ and $\sim 10\%$ are expected. The figure shows also the strong dependence of the resolution on η and ϕ.

4.2.5 The Magnet System

The track of charged particles is bend when the particles enter a magnetic field perpendicular to their direction of motion. The curvature of the track is then not only dependent on the strength of the magnetic field, but also on the momentum of the particle transverse to the field. Thus, if a magnetic field is applied in the tracking chambers of a detector, the particle momentum can be reconstructed from the track via

$$r[\mathrm{m}] = \frac{p[\mathrm{GeV}]}{0.3B[\mathrm{T}]}, \tag{4.2}$$

where r is the bending radius, which is determined from the sagitta of the track, p the particle momentum and B the magnetic field. If a spatial hit resolution of σ_x is provided, the momentum resolution for a track measured at N equidistant points is given by the Glueckstern formula

$$\frac{\sigma_p}{p} = \frac{\sigma_x p}{0.3BL^2}\sqrt{\frac{720}{N+4}}. \tag{4.3}$$

Thus, in addition to a good spatial resolution, a high B field is needed for high precision momentum measurements. In ATLAS, this is achieved by two magnet systems. For the inner detector a central solenoid magnet provides a nominal axial magnetic field of 2 T (peak strength 2.6 T) with an electric current of 7.6 kA. The solenoid is attached in ATLAS between the ID and the LAr EM calo. It bends the tracks of charged particles in the inner detector.

For the muon chambers, a system of three toroidal magnets is used, each consisting of eight superconducting air-core coils. The magnetic field, which is kept up by an electric current of 20 kA, peaks at a value of 3.9 T (4.1 T) for the barrel part (endcap toroids) and is adequate for the desired precision. The end-cap toroids are rotated with respect to the barrel toroid by an angle of 22.5 degrees in order to achieve optimal bending power in the overlap region of the two magnets on each side.

4.2.6 Trigger System and Data Acquisition

The LHC bunchcrossing frequency of 40 MHz at its design luminosity of $L = 10^{34}\mathrm{cm}^{-2}\mathrm{s}^{-1}$, each with ~ 20 proton proton interactions, corresponds to a data rate of more than 1 PByte/s. As this is clearly too much for permanent storage, the data rate has to be reduced by orders of magnitude. Moreover, the cross sections for most new physics processes is much lower than for the respective background processes, as shown in figure 4.8. Thus, before any event data is stored, it has to be decided whether the event is "interesting" and worth saving it, or not. The ATLAS trigger system takes these decisions, by checking the abundance of muons, electrons/photons or jets exceeding certain thresholds in transverse momentum, energy and isolation, as well as the total (missing) transverse energy.

The reduction of the data rate is done stepwise at ATLAS and the level-1 (LVL1) trigger, which is the only pure hardware trigger of ATLAS, performs the first of these steps. With an input rate of approximately 1 GHz, the LVL1 trigger uses information from the muon trigger system (i.e. RPC and TGC only) and from the tracker (TRT only), as well as coarsened calorimeter information. The actual parametrisation of the LVL1 trigger is configured via e.g. Field Programmable Gate Arrays, which allow for modifications, if needed. As long as it takes the LVL1 trigger to take a decision, the information about the whole event has to be stored in pipeline memories, being either deleted if the LVL1 response is negative, or read out into readout buffers (ROBs) in the reverse case, where they are held until the event passes or is refused by the level-2 (LVL2) trigger.

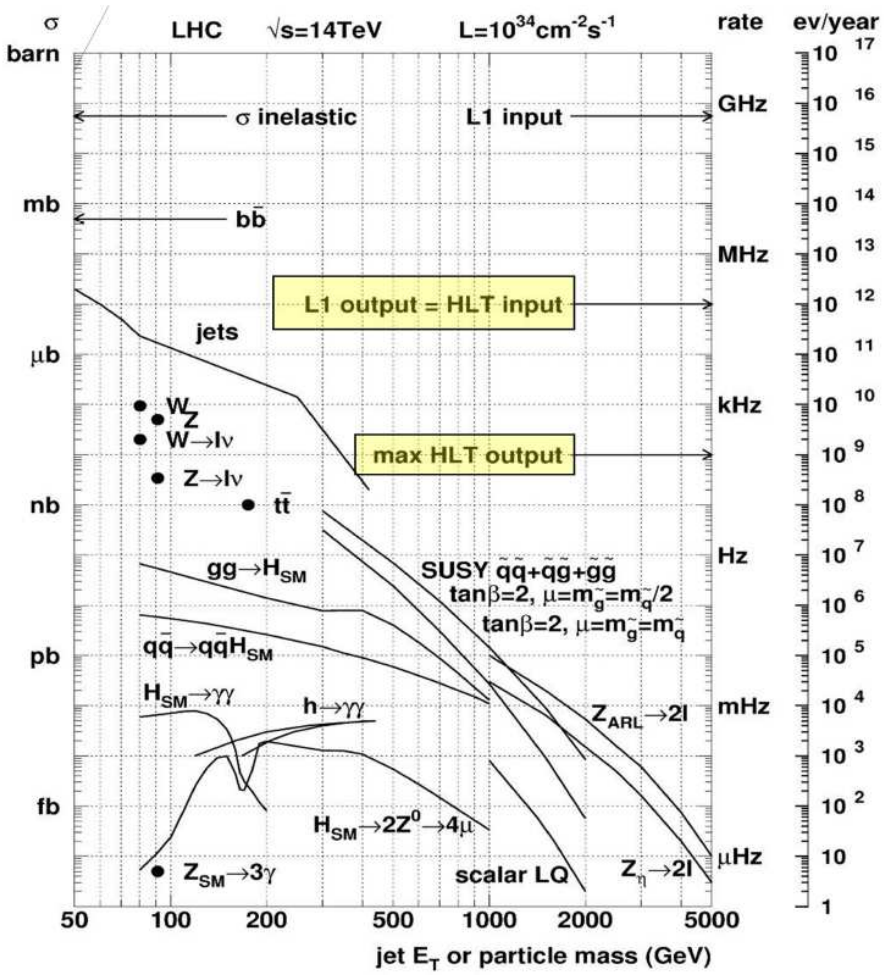

Figure 4.8: The expected cross sections for various physics processes at the LHC. The total elastic cross-section is expected to be $\sim$ 40 mbarn. The interesting processes, of which for example the $t\bar{t}$-pair production is included in the figure, occur at rates orders of magnitude below that. Processes involving new physics have even lower production rates (depending on the kind of new physics, of course). For example, the cross section for sparticle pair production for $\tan\beta = 2$, are in the order of one nbarn in the best case, while it may happen that this cross sections gets below one pbarn, in a still realistic scenario. The dependence of this cross-section with respect to the squark/gluino masses is shown in the graph. The figure illustrates that besides providing the conditions for sparticle production, it is a huge challenge to pick out event candidates for these processes.

The LVL1 trigger has a maximum output rate of about 75 kHz. Nevertheless, the actual output rate is expected to be only half of this for interesting physics events. The LVL2 trigger reduces this rate further to approximately 1 kHz. In order to do this, the LVL2 trigger examines so-called Regions of Interest (RoIs). By looking only at certain regions in the η-ϕ space, the LVL2 trigger only accesses event information that is necessary for its decision. This is typically only a few percent of the overall event data. It is expected that it will take the LVL2 trigger some microseconds ($O(1-10)$) to accept or reject an event. In contrast to LVL1, the LVL2 trigger uses information from the precision muon chambers (MDTs and CSCs) in addition to

the TGCs and RPCs, as well as the full granularity information from the calorimeters and the ID, leading to sharpened thresholds for example.

The final step in the online event selection is the EventFilter (EF). The data is moved here from the ROBs in a process called event building. The EF can access the whole event data, which allows it to use complex algorithms like vertex or track fitting. The output rate of the EF is in the order 100 Hz, which corresponds to a recording rate of $O(100)$ MB/s. This data is then processed and prepared for offline analyses. The LVL2 trigger and the EF are both pure software based triggers and are together referred to as the High Level Trigger.

The complete trigger system is shown in figure 4.9. An overall data volume of about 1 PByte is expected per year, which can be accessed by physicists in a distributed analysis computing model via grid computing, where several tenthousand CPUs are available for offline analyses.

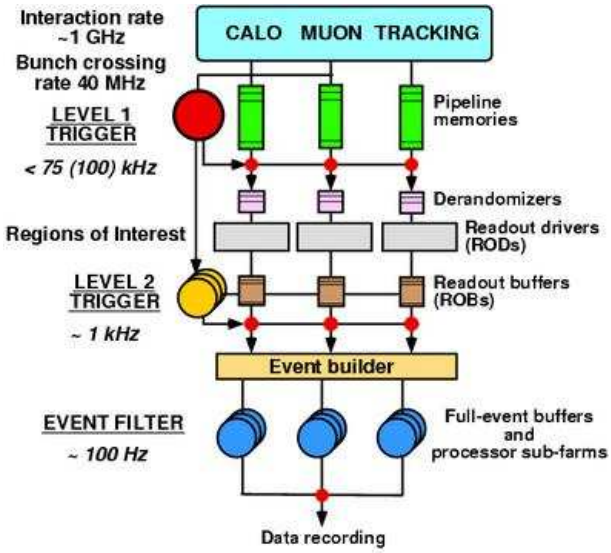

Figure 4.9: This is an illustration of the ATLAS trigger system. The different stages of triggering and the individual components of each trigger are shown. On the left hand side, the respective input/output rates of the trigger stages are shown.

5 An Estimator for a Sparticle Mass Sensitive Observable

The kinematic endpoint in the invariant mass spectrum of the visible products of a leptonic decay chain of the second lightest neutralino is one observable sensitive to sparticle masses. This observable can most likely be measured at the ATLAS experiment, given that the nature is supersymmetric and that the mSUGRA model is the correct parametrisation of SUSY breaking. An estimator for this endpoint was constructed and evaluated for different input values using Monte Carlo (MC) data, assuming that nature is actually supersymmetric and that the mSUGRA model is the correct model of SUSY breaking. A calibration curve was constructed by comparing the estimated values with the input values. The procedure is described in this chapter.

5.1 Monte Carlo Simulation

Any method used for the analyses of ATLAS data needs to be tested on Monte Carlo data before being applied to real data. The ATLAS software framework, *Athena* [47], which is an ATLAS specific distribution of the *GAUDI* [48] system, provides the infrastructure for the generation, simulation, digitisation and reconstruction of the MC data, as well as the actual analysis of the produced/measured datasets itself. All these steps can be run independently from each other. Several codes like Herwig [49], MC@NLO [50] and ALPGEN [51] are available for the first step, the event generation. The second step is the detector simulation which is done with the *Geant4* package [52]. This software simulates the passage of particles and radiation through matter in detail. Thus, a given set of particle four-momenta is translated into detector hits. These are subsequently processed in the digitisation step and reconstruction algorithms are run over the output of the digitisation. These steps take into account the finite resolution of the detector systems and the efficiencies of the reconstruction process. Finally, the output of these reconstruction algorithms is stored in Event Summary Data (ESD) or Analysis Object Data (AOD). The MC data stored in the AODs and ESDs contains the *true* information of all particles, like the four-momenta as calculated by the event generator, as well as the reconstructed candidates for physics objects.

As the detailed simulation of the ATLAS detector with all its subsystems is a time consuming task ($\sim$ 15-30 minutes per event using a CPU with a clock rate of $\sim$ 2 GHz) and a high number of events ($\sim 10^4 - 10^6$) is usually required, the detector simulation can also be done with the ATLFAST I package [53]. Instead of using the full *Geant4* simulation, the digitisation and the reconstruction algorithms, the resolution effects and detector efficiencies are parametrised. The four-momenta of the generated particles are smeared according to Gaussian distributions. The parameters of these distributions depend on the particle type and its direction, and are extracted from full simulations.

5.1.1 Event Generation

A number of independent and numerically different theoretical endpoints was needed for the construction of the calibration curve. Events were generated within the scope of the bachelor thesis of J. Hofestaedt [54], where the exact procedure is described in a little more detail. The event generator Herwig and the multi parton scattering plug-in Jimmy [55] as embedded in the *Athena* release 14.5.0 were used for the generation of the events. For each of the parameter sets listed in table 5.1, approximately 160,000 SUSY events in proton-proton collisions at a center of mass energy of 10 TeV, at which the first significant dataset from ATLAS was expected at that time, were generated. All possible supersymmetric production processes in such collisions were switched on and any allowed decay may occur in the generated events (for examples see chapter 2.2.4). The input SUSY mass spectrum, decay rates and mixing matrices were computed with the *Isasugra* package, version 7.79 [56, 57].

5.1.2 Detector Simulation

The ATLAS detector was simulated using the ATLFAST II package [58], which is a combination of a full detector simulation and a fast parametrised smearing of the directly measurable quantities of particles and jets. The ATLAS Inner Detector is fully simulated using *Geant4*, while the Calorimeters are simulated using the *FastCaloSim* package. The Muon System can be fully simulated, or simply parametrised as in the ATLFAST I simulation. The fully simulated muons were used, while trigger information was not taken into account for the present study. The ATLFAST II simulation was performed on the LHC computing grid (LHCG), using *Athena* version 14.5.0.1.

5.1.3 Validation of the Generated Monte Carlo Data

For the validation of the privately produced MC data, a total of 18,500 events were produced at the ATLAS SU3 benchmark point [59]. These events were compared to the official dataset "mc08.105403.SU3_jimmy_susy.merge.AOD.e352_a84_t53". This was produced with *Athena* version 14.2.25.6. All the parameter points under examination here are SU3 like points in the sense that three of the five mSUGRA parameters are fixed at the SU3 values. The figures 5.1 and 5.2 show the comparison for several muon variables. Since only muons were used for the construction of the calibration curve, the respective plots for electrons and jets are not shown at this point. However, the agreement between the official and the private production is good for electrons and jets at event generator level, as well. For a number of reasons, the private MC had to be produced locally rather than on the LHCG, such that a one-to-one agreement is not expected. This is due to the unavoidable usage of two different *Athena* versions for the production of both samples, as some of the patched versions that were used for the production of the official MC were not available locally.

There are small differences in the distributions, especially in the tails of the energy and transverse momentum distributions. These can be explained by the usage of different *Athena* versions for the production of the two samples. Besides statistical differences, a major change in the electron reconstruction from 14.2.25.6 to 14.5.0.1 and changes in the jet reconstruction algorithms might slightly affect the muon distributions by overlap removal. Minor changes in the muon reconstruction could as well explain the differences, partly. Overall, the distributions show a reasonable agreement, such that the private production was regarded to be valid.

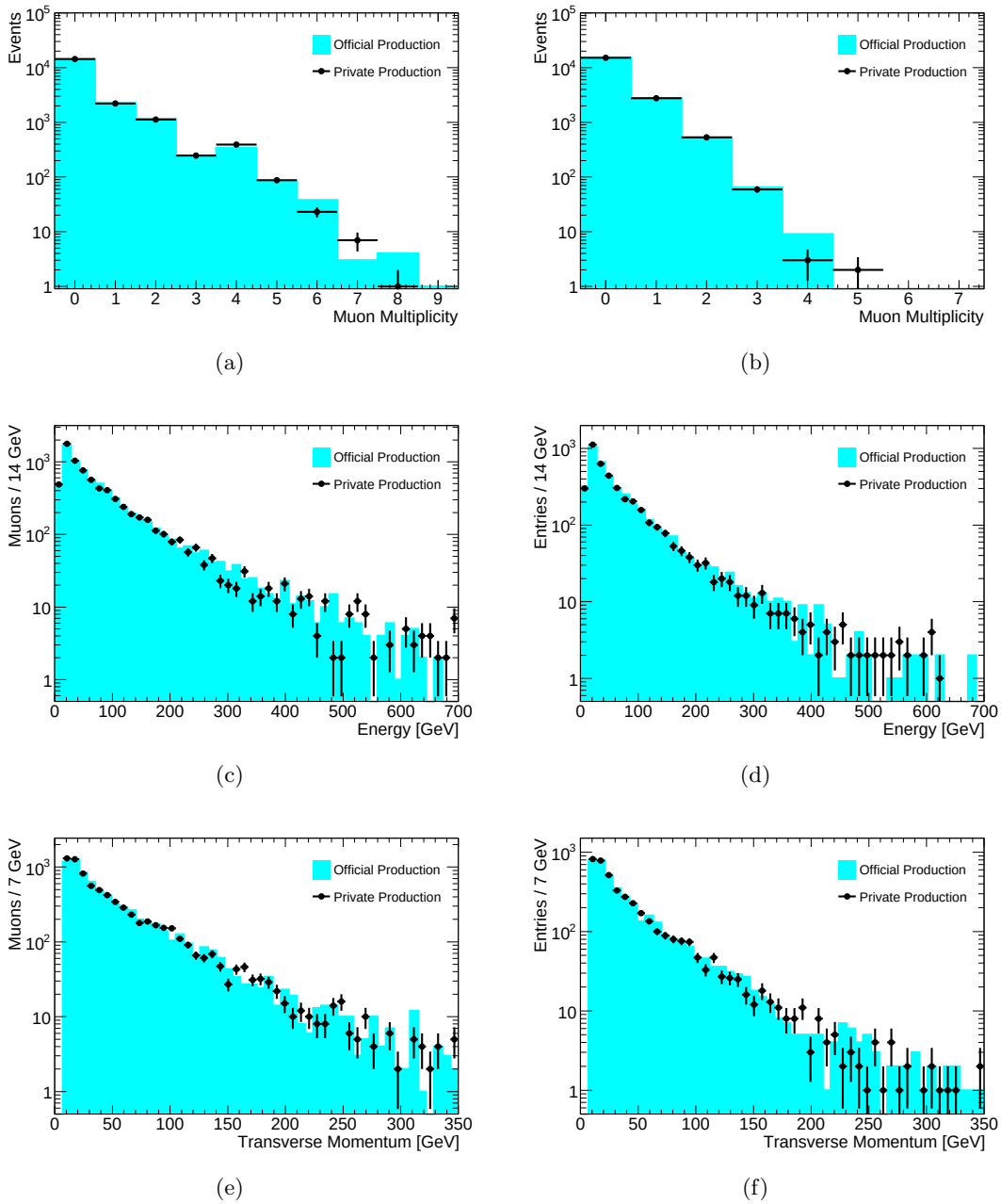

Figure 5.1: Comparison of private Monte Carlo Production with official Monte Carlo Production. On the left hand side, (a), (c) and (e), the comparison is shown for the Monte Carlo *truth* information (i.e. generator level), while on the right hand side, (b), (d) and (f) show the respective distributions for the reconstructed muons after some selection cuts have been applied. The STACO muon collection has been used [59]. In all histograms the error bars for the official sample have been omitted for a better readability. The observed differences are mostly within statistical limits and do not seem to be critical. An explanation for differences in the reconstructed spectra, besides statistical fluctuations, might be a major difference in the electron reconstruction algorithms, which via overlap removal might slightly affect the selection of the muon candidates.

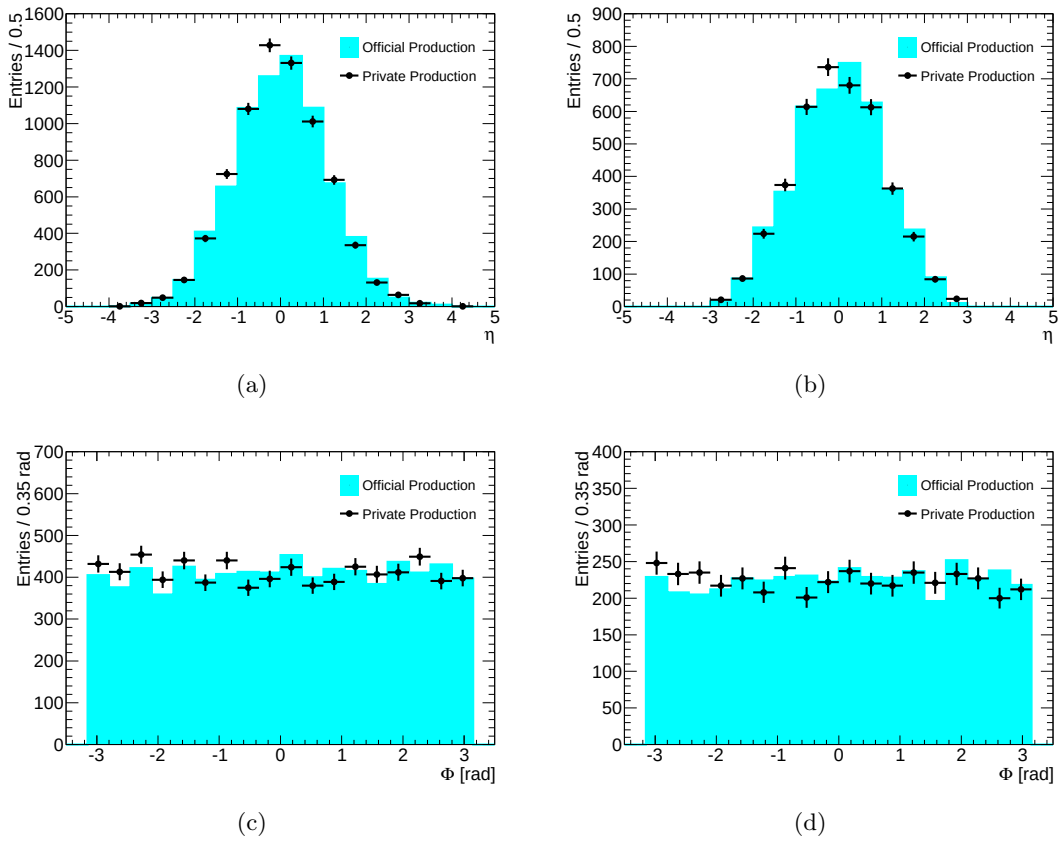

Figure 5.2: A comparison between the private and the official Monte Carlo for η and ϕ. As for the energy, momentum and multiplicity, a good agreement between both samples can be seen. As expected, the ϕ distributions are both flat, while the η-distribution peaks around $\eta = 0$. Again, the plots on the left hand side show the comparison at generator level, while on the right hand side the comparison for the reconstructed muon candidates is shown.

5.2 An Estimator for a Kinematic Endpoint Related to Sparticle Masses

A significant region of the mSUGRA parameter space features a neutralino LSP. At least two undetectable, massive particles are therefore expected in these regions in the final states of supersymmetric processes at the LHC, given that R-parity is conserved. A direct measurement of the sparticles' masses is thus difficult and more advanced techniques and observables need to be studied for the extraction of the sparticle mass spectrum. One family of observables which is being studied extensively are kinematic edges in the mass spectra of visible decay products. An example is the endpoint in the dilepton mass spectrum of the decay chain

$$\tilde{\chi}_2^0 \rightarrow \tilde{l}_i^{\mp} l^{\pm} \rightarrow \tilde{\chi}_1^0 l^{\mp} l^{\pm}. \tag{5.1}$$

The endpoint m_{ll}^{max} is sensitive to the masses of all three sparticles occurring in this chain. The distribution of the dilepton mass follows a linear relation with a sharp endpoint. In the experimental data, this sharp endpoint is washed out by detector effects. The goal of this chapter

is the construction of an estimator for the kinematic endpoint m_{ll}^{max}. Experimental effects are modelled using a number of approximations. A good estimator of the endpoint should be related to the true (theoretical) endpoint via an invertable (and simple) relation, the simplest of which is a straight line,

$$m_{ll}^{max,est.} = a + b \cdot m_{ll}^{max,true}. \tag{5.2}$$

In the best case the estimator should be unbiased, i.e. $a = 0$, $b = 1$, as this would maximize the precision of the estimation. The extraction of these parameters for the constructed estimator of m_{ll}^{max} is described at the end of this chapter.

5.2.1 The Decay Chain $\tilde{\chi}_2^0 \to \tilde{l}_i^{\mp} l^{\pm} \to \tilde{\chi}_1^0 l^{\mp} l^{\pm}$: The Kinematic Endpoint and a Model for the Signal Distribution

If the leptonic decay (5.1) of the second lightest neutralino is considered, as shown in figure 5.3, the visible decay products are two leptons. In the following lepton means either a muon or an electron. The decay chain may as well contain two taus, but these undergo hadronic or leptonic decays including neutrinos in the detector, such that the treatment of the visible decay products is different from the treatment of muons and electrons described in the following. Although none of the sparticles can be seen directly, information about these can be gained by looking at these leptons. Following the common nomenclature, the lepton originating from the decay of the $\tilde{\chi}_2^0$ will be referred to as the *near* lepton, and the lepton originating from the $\tilde{l}_i$ decay is referred to as the *far* lepton. The only directly measurable observables of this decay chain are the four-momenta of these two leptons, p_μ^{near} and p_μ^{far}. The slepton must be on-shell, if the process shown in figure 5.3 is a sequence of two two-body decays. For the mSUGRA points under study here, the real three-body decay

$$\tilde{\chi}_2^0 \to l^{\pm} l^{\mp} \tilde{\chi}_1^0, \tag{5.3}$$

in which the slepton would be off-shell, is highly suppressed as shown in figure 5.3. For this reason a possible contribution of real three-body decays does not need to be taken into account for all further considerations, here. Furthermore, at all parameter points used here, the slepton is the partner of the right chiral lepton. The mass hierarchy forbids the respective decay including a $\tilde{l}_L$ instead.

In a reference frame S, the square of the sum of the two lepton momenta in (5.1) is given by

$$\begin{aligned} m_{ll}^2 &= (p_{near} + p_{far})_\mu (p_{near} + p_{far})^\mu \\ &= 2m_l^2 + 2E_{near}^S E_{far}^S - 2\vec{p}_{near}^{\,S} \cdot \vec{p}_{far}^{\,S} \qquad (5.4) \\ &\approx 2E_{near}^S E_{far}^S \left(1 - \cos\theta^S\right), \qquad (5.5) \end{aligned}$$

where for (5.5) the high energy approximation $m_l = 0$ is applied and θ^S is the opening angle between the two three-momenta $\vec{p}_i^{\,S}$. If S is chosen to be the rest frame of the slepton $S_{\tilde{l}}$, and two-body decay formulae [13] are applied, (5.5) can be rewritten as

$$\begin{aligned} m_{ll}^2 &= \underbrace{2\frac{m_{\tilde{l}}^2 - m_{\tilde{\chi}_1^0}^2}{2m_{\tilde{l}}}}_{=E_{far}^{S_{\tilde{l}}}} \cdot \underbrace{\frac{m_{\tilde{\chi}_2^0}^2 - m_{\tilde{l}}^2}{2m_{\tilde{l}}}}_{=E_{near}^{S_{\tilde{l}}}} \cdot \left(1 - \cos\theta^{S_{\tilde{l}}}\right), \\ &= \frac{\left(m_{ll}^{max}\right)^2}{2} \cdot \left(1 - \cos\theta^{S_{\tilde{l}}}\right), \qquad (5.6) \end{aligned}$$

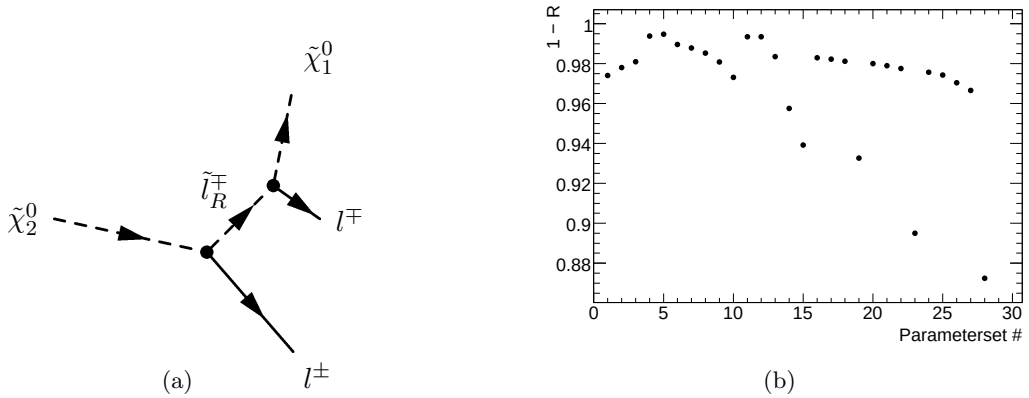

Figure 5.3: (a) The tree level Feynman diagram for the $\tilde{\chi}_2^0$ decay chain studied in this chapter. In collisions at the LHC, the $\tilde{\chi}_2^0$ will most likely originate from a squark decay. Since it is unstable, it can decay into a lepton and a slepton as shown in the figure. The slepton is unstable itself and may further decay into a $\tilde{\chi}_1^0$ and another lepton. The $\tilde{\chi}_1^0$, in this case the LSP, escapes the detector undetected, leaving the two leptons as the only visible decay products of the $\tilde{\chi}_2^0$. (b) This diagram shows 1-R, where R is defined as $\frac{\Gamma(\tilde{\chi}_2^0 \to \tilde{\chi}_1^0 ll)}{\Gamma(\tilde{\chi}_2^0 \to \tilde{l}_R l) \times \Gamma(\tilde{l}_R \to \tilde{\chi}_1^0 l)}$. In most cases, the relative fraction R is less than some per cent.

where the maximal value

$$(m_{ll}^{max})^2 = \frac{\left(m_{\tilde{\chi}_2^0}^2 - m_{\tilde{l}}^2\right)\left(m_{\tilde{l}}^2 - m_{\tilde{\chi}_1^0}^2\right)}{m_{\tilde{l}}^2} \tag{5.7}$$

is acquired when the two leptons are back to back, i.e. $\cos\theta^{S_{\tilde{l}}}$ = -1.

Both the slepton and the second lightest neutralino are unstable and thus have a finite average lifetime. This is directly translated into a finite width in the respective mass distributions via the uncertainty principle (see, for example, [60]). The finite width of the distributions for two of the masses occurring in (5.7) thus lead to a distribution with non-vanishing width for the endpoint. Nevertheless, as shown in figure 5.4, the widths of the relevant mass distributions are very small with respect to the endpoint for all parameter sets used here (see table 5.1), such that this effect is neglected, and a sharp distribution for the theoretical endpoint (5.7) is assumed.

In $S_{\tilde{l}}$, there is no angular correlation between the two leptons since the slepton carries spin 0. This can be translated into a differential cross section for the process shown in figure 5.3, which in $S^{\tilde{l}}$ is given by

$$\frac{1}{\sigma}\frac{d\sigma}{d\cos\theta^{S_{\tilde{l}}}} = \frac{1}{2}. \tag{5.8}$$

By means of (5.6), this is directly transferred into a differential cross-section with respect to the Lorentz invariant mass, namely

$$\begin{aligned} \frac{1}{\sigma}\frac{d\sigma}{dm_{ll}} &= \frac{1}{\sigma}\left|\frac{d\cos\theta}{dm_{ll}}\right|\frac{d\sigma}{d\cos\theta} \\ &= \frac{2m_{ll}}{\left(m_{ll}^{max}\right)^2}. \end{aligned} \tag{5.9}$$

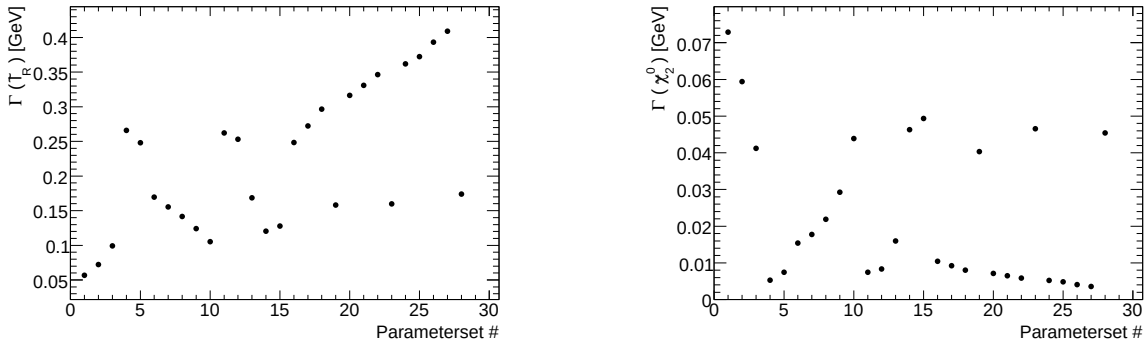

(a) (b)

Figure 5.4: (a) shows the width of the $\tilde{l}_R$, while (b) shows the width of the $\tilde{\chi}_2^0$ for the parameter points examined in this chapter. On the y-axis, the width is given in GeV, on the x-axis the number of the respective parameter point (as listed in 5.1) is shown. For both particles and nearly all parameter points, the decay widths are less than 1% of the theoretical endpoint in the dilepton spectrum, such that their smearing effect on the theoretical endpoint is neglected, here.

As the dilepton mass m_{ll} is Lorentz invariant, so is the differential cross-section (5.9). Thus, if the dilepton mass spectrum of the decay shown in figure 5.3 is measured, a triangular distribution with a slope of $m = \frac{2}{\left(m_{ll}^{max}\right)^2}$ and a sharp endpoint (5.7) is expected by theory. This is shown for the Monte Carlo *truth* information for parameter set 5 in figure 5.5 as an example.

Experimentally, the invariant dilepton mass is determined from the four-momenta of the two leptons which can only be measured with a finite resolution. Assuming Gaussian uncertainties, the probability to measure the value p_z for the z-component of a particle's three-momentum, for example, if the true value is given by p_z^t, can then be calculated by

$$p_{meas}(p_z|p_z^t) = \frac{1}{\sqrt{2\pi}\sigma_{p_z}} \cdot e^{-\frac{(p_z - p_z')^2}{2\sigma_{p_z}^2}}, \tag{5.10}$$

where the mean p_z' and the width σ_{p_z} of the distribution are in general functions of all components of the lepton four-momenta p_{li}. A general function describing the experimentally measured dilepton mass spectrum from the decay chain $\tilde{\chi}_2^0 \to l\tilde{l} \to \tilde{\chi}_1^0 ll$ is therefore given by

$$\left(\frac{1}{\sigma}\frac{d\sigma}{m_{ll}}\right)_{exp} = \int \frac{2m_{ll}'}{\left(m_{ll}^{max}\right)^2} \cdot f(p_{l1}, p_{l2}) \cdot \delta(m_{ll}' - m_{ll}^2) d^4p_{l1} d^4p_{l2}, \tag{5.11}$$

in which the function f parametrizes the resolution effects and m_{ll} is regarded as a function of the four-momenta, $m_{ll}^2 = p_{l1} \cdot p_{l2}$. From a measurement of the cross section (5.11), an estimator for the value of m_{ll}^{max} can be extracted.

In (5.11), f is in principle the product of eight expressions of the form (5.10), one for each component of the two lepton four momenta. In the present study, a simplifying assumption has been made. The function f was not considered as a function of each single component of the muon four-momenta, but rather as a function of the invariant mass itself. Assuming Gaussian uncertainties for each measured value of m_{ll}, f is again of the form of (5.10). The width of this distribution was taken to be constant, and the mean of the Gaussian was taken to be the *true*

Number	m_0 [GeV]	$m_{1/2}$ [GeV]	Events	L_{int} [fb^{-1}]	N_{Signal}	$m_{ll}^{max,theo}$ [GeV]
SU3	100	300	–	–	–	102.70
1	76	300	166,567	29.81	1,394	92.23
2	82	300	166,546	30.12	1,871	95.82
3	91	300	166,567	30.39	2,423	99.99
4	100	210	166,599	4.88	4,284	52.94
5	100	220	166,589	6.16	4,650	62.11
6	100	270	166,582	17.65	5,179	92.05
7	100	280	166,547	21.27	4,734	96.04
8	100	291	166,558	26.14	4,025	99.96
9	100	305	166,534	33.37	2,908	104.11
10	100	322	166,546	44.76	2,058	108.07
11	110	240	166,594	9.73	4,577	71.16
12	110	245	166,584	10.8	4,734	74.92
13	110	300	166,558	31.02	4,726	104.01
14	115	355	166,552	77.49	1,632	120.93
15	125	380	166,537	113.82	1,397	130.16
16	128	300	166,539	31.69	4,861	101.87
17	133	300	166,563	31.94	4,779	100.18
18	138	300	166,530	32.15	4,753	97.99
19	140	400	166,511	154.05	1,508	140.06
20	142	300	166,527	32.23	4,691	95.87
21	145	300	166,535	32.38	4,716	94.00
22	148	300	166,520	32.47	4,637	91.96
23	150	430	166,496	234.22	1,153	150.56
24	151	300	166,554	32.61	4,584	89.71
25	153	300	166,531	32.75	4,539	88.08
26	157	300	166,537	32.89	4,377	84.45
27	160	300	166,518	32.98	4,046	81.43
28	160	450	166,494	307.82	1,035	158.75

Table 5.1: The used parameter sets. As a comparison, the official ATLAS benchmark point SU3 is included in the list. For all parameter sets listed here (including the SU3 benchmark point), $\tan\beta = 6$, $A_0 = -300$ GeV, $\text{sgn}\mu = +1$. The sets cover a range of roughly 100 GeV on the m_{ll}^{max}-axis, such that with the construction of the calibration curve a reasonable range of possible endpoints for the decay chain shown in figure 5.3 in the mSUGRA bulk region is covered. The total number of generated events, the corresponding integrated luminosity at $\sqrt{s} = 10$ TeV and the number of signal events is shown, as well as the theoretical endpoint.

value. The differential cross section (5.11) is thus given by

$$\begin{aligned}
\frac{1}{\sigma}\frac{d\sigma}{dm_{ll}} &= \frac{1}{\sqrt{2\pi}\sigma_{m_{ll}}} \cdot \int \frac{2m'_{ll}}{\left(m_{ll}^{max}\right)^2} \cdot e^{-\frac{(m'_{ll}-m_{ll})^2}{2\sigma^2_{m_{ll}}}} dm'_{ll} \\
&= \frac{2 \cdot \sigma_{m_{ll}}}{\sqrt{2\pi} \cdot \left(m_{ll}^{max}\right)^2} \left[e^{-\frac{m_{ll}^2}{2\sigma^2_{m_{ll}}}} - e^{-\frac{(m_{ll}^{max}-m_{ll})^2}{2\sigma^2_{m_{ll}}}} \right] \\
&+ \frac{2m_{ll}}{\left(m_{ll}^{max}\right)^2} \cdot \frac{1}{2} \left[\text{erf}\left(\frac{m_{ll}^{max} - m_{ll}}{\sqrt{2}\sigma_{m_{ll}}} \right) - \text{erf}\left(\frac{-m_{ll}}{\sqrt{2}\sigma_{m_{ll}}} \right) \right],
\end{aligned} \tag{5.12}$$

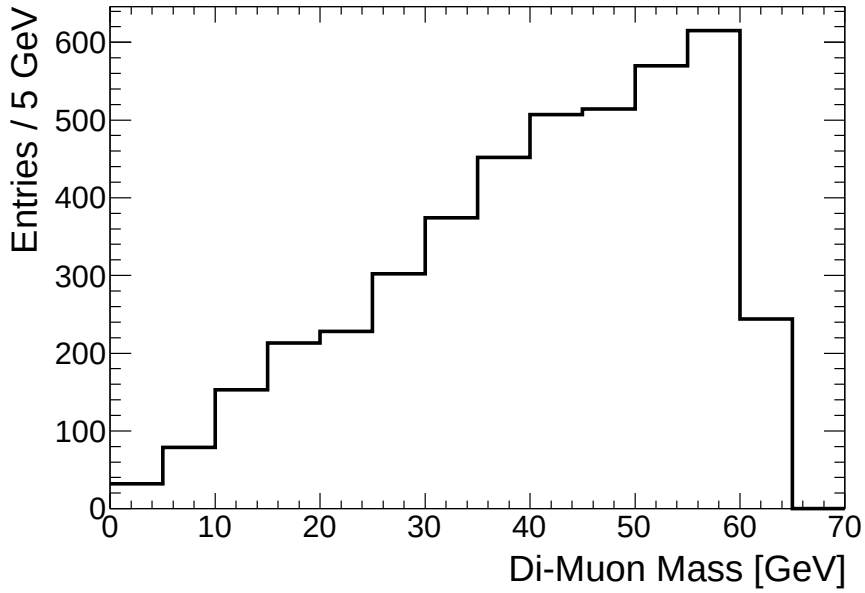

Figure 5.5: The invariant mass spectrum of muon-pairs originating from the $\tilde{\chi}_2^0$-decay chain. The histogram shows the distribution obtained from Monte Carlo *truth* information for the Parameterpoint 5. The triangular shape and the endpoint are clearly visible. The fact that the last bin shows less entries than the next to last one is a binning effect.

in which $\sigma_{m_{ll}}$ is the invariant mass resolution. The function (5.12) is plotted for various values of this resolution in figure 5.6. The effect of the smearing can nicely be seen here. With decreasing resolution, i.e. increasing $\sigma_{m_{ll}}$, the sharp edge is washed out and the distribution peaks at lower values. In the limit $\sigma_{m_{ll}} \to 0$, the perfect triangular shape is restored, while for large values of $\sigma_{m_{ll}}$ the distribution becomes more and more Gaussian.

5.2.2 Background

In the present study, only supersymmetric and combinatorial background was taken into account. If, for example, a pair of gluinos is produced and both of these undergo the decay chain shown in figure 2.12(a), there are four leptons of the same flavour in the final state in $\sim 25\%$ of all such events. This yields two potential combinations of two pairs of opposite sign leptons, of which only one is the "correct" one (the signal combination). From data it is not clear which one is the correct combination. There are more decay chains with one or more leptons, like the one shown in figure 2.12(b). Finally a Z^0 decaying into two muons might occur in one of the sparticle decays. These processes give rise to more combinatorial background. Obviously, a cut on the Z^0 mass must not be applied for the background reduction. The supersymmetric background is taken into account and two ways to handle it are described in the next section.

SM background like top pair production was explicitly not taken into account for the present study.

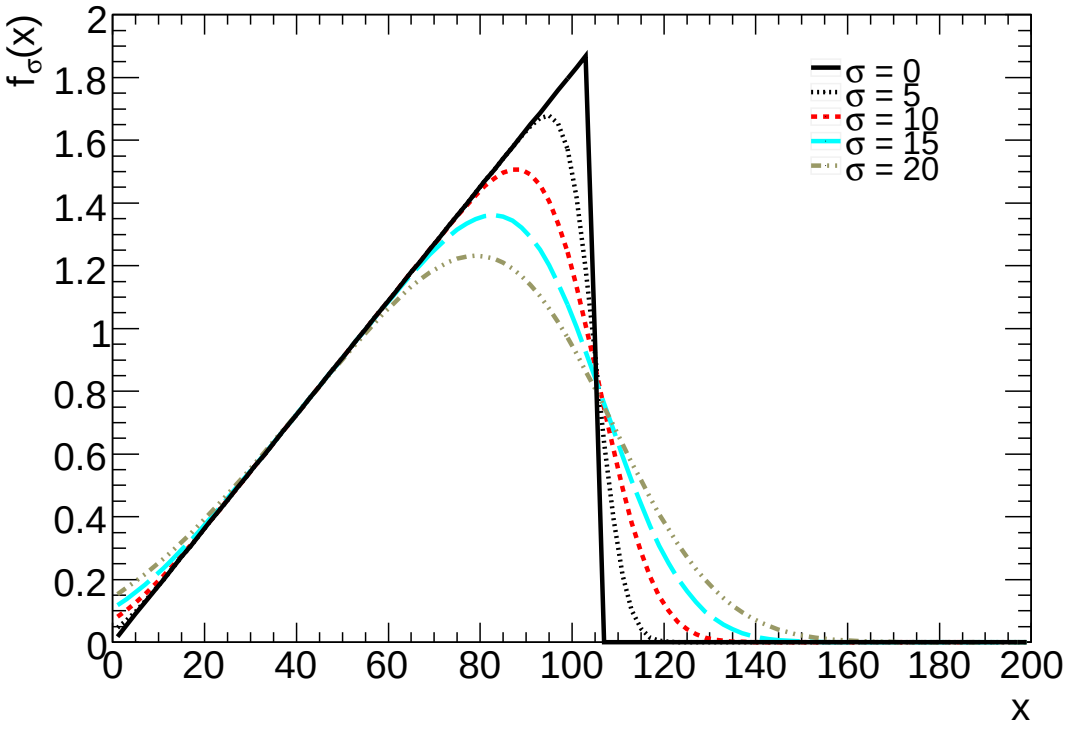

Figure 5.6: Plots of the tested fit function for a number of different invariant mass resolutions. The hypothetical endpoint here was fixed at $x \sim 100$.

5.2.3 Calibration Curve

The extraction of the kinematic endpoint (5.7) was done in the same way for all 28 parameter sets, no point-specific optimisations have been used. Only muons were used for this first approach, although for reasons of lepton universality and the dominant third family approximation (i.e. $(\mathbf{y}_l)_{ab} = 0$ for the first two generations), the numerical value of the endpoint is expected to be (nearly) the same for a muonic and an electronic decay of the $\tilde{\chi}_2^0$, as in this case $m_{\tilde{\mu}} = m_{\tilde{e}} = m_{\tilde{l}}$.

The muon candidates used for the extraction of the invariant mass spectrum were taken from the AOD STACO muon collection [59], which contains muon candidates reconstructed from statistically combined ID and muon chamber hits. Muons were selected according to the proposed cuts in the SUSY CSC notes [59]. These are:

- Combination quality: The tracks of the muon candidate in the ID and the muon system should match with a $\chi^2 < 100$. This is a very loose cut.
- Isolation: The energy deposit in the calorimeter in a cone of $\Delta R = \sqrt{(\Delta\eta)^2 + (\Delta\phi)^2} < 0.2$ around the muon should be less then 10 GeV. This criterion was used because only isolated muons are of interest, here.
- Jet Overlap: All muons in a cone of $\Delta R = 0.4$ around a jet were rejected as these muons were assumed to originate from the jet. Only jet candidates with a minimal distance of $\Delta R = 0.2$ to the next nearest electron were considered.

Any event with a pair of two muons with opposite charge, fulfilling these criteria, was selected and the muon pair was taken as a candidate muon pair for the extraction of the invariant mass triangle. This way, the obtained set of opposite sign(charge) same flavour (OSSF) dimuon pairs contains a lot of combinatorial background.

In the first step a cut on the transverse momentum of both muons was applied for the reduction of the supersymmetric and combinatorial background. It turned out that the signal to background ratio could significantly be improved for all used parameter sets when a cut of 25 GeV was applied. This can be seen from the p_T-distributions shown as an example in figure 5.7. The cut efficiencies for signal and combinatorial background are listed in table 5.2. Before the cut is applied, the background is clearly dominant, but after the application of the cut this is no longer the case. However, the shape of the background distribution changes. For the extraction of the kinematic endpoint of the signal spectrum, the remaining background was modelled by a Landau distribution. It was checked that the signal distribution, in particular the position of the endpoint, is not significantly altered by the application of the cut.

Figure 5.8 shows the effect of the cut for one parameter set. After the application of the cut, the triangular shape of the signal distribution becomes clearly visible in the total spectrum, which is not the case before the cut is applied. This method does not provide the highest separation power and signal efficiency, but it turned out to be very robust. A common method for the reduction of the combinatorial background is a statistical subtraction. Some details on this method and a reason why it was not used at this point are described in appendix A.

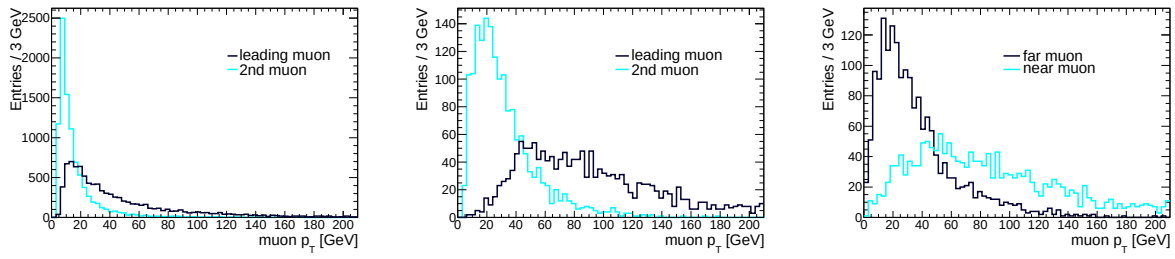

(a) (b) (c)

Figure 5.7: The transverse momentum distributions for (a) background, and (b)/(c) signal muon pairs. The *leading* muon is always the muon with the higher transverse momentum. As it is impossible to assign the attributes near and far to the muons correctly from data, this ordering seems natural. At the parameter point belonging to the shown plots (which is parameter point 2), the near lepton is the leading lepton in nearly all cases, which can be seen by a comparison between (b) and (c). This is due to the fact that at this point $m_{\tilde{\chi}_2^0} - m_{\tilde{l}_R} \approx 80$ GeV, while $m_{\tilde{l}_R} - m_{\tilde{\chi}_1^0} \approx 25$ GeV, such that the phase-space for the far lepton is much smaller than that for the near lepton. This is not the case for all parameter points, however. From the distributions (a)-(c) it can already be seen that a cut at $p_T = 25$ GeV for both muons might help to get rid of most background, while leaving a reasonable number of signal events.

After the extraction of the OSSF muon-pair candidates from the MC data and the application of the transverse momentum cut of 25 GeV, the invariant-mass distribution of all the remaining dimuon combinations was fitted with an appropriate function. It was already indicated that this function is given by

$$f_{m_{ll}}^{FIT} = N_{Sig} \cdot g\left(m_{ll}|m_{ll}^{max}, \sigma_{m_{ll}}\right) + N_{Bkg} \cdot \text{Landau}(m_{ll}|\text{MPV}, \sigma_{Landau}), \tag{5.13}$$

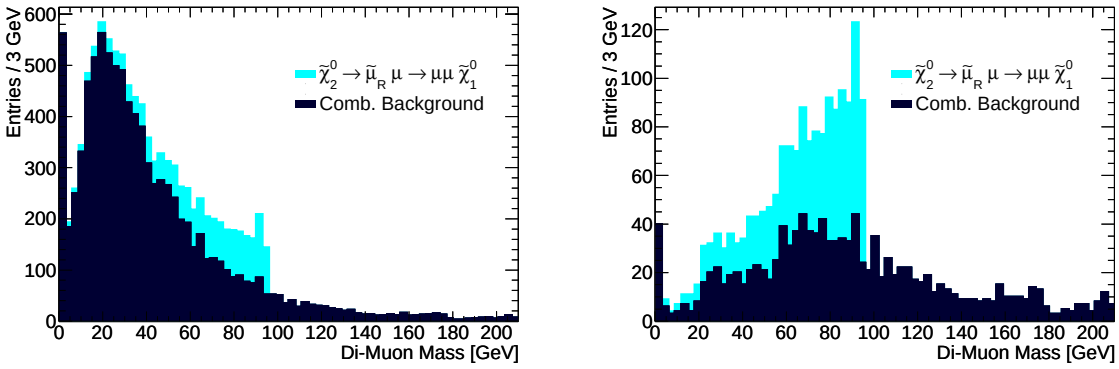

(a) (b)

Figure 5.8: The impact of the transverse momentum cut on the invariant mass-distribution for both signal and background at parameter point 2. (a) shows the distributions for $p_T > 5$ GeV, while in (b) the cut at 25 GeV has been applied. The signal-triangle becomes clearly visible after the application of the cut, while a significant part of the combinatorial background is cut away.

in which g is given by (5.12). Evidently, there are six adjustable parameters in this function, namely

- m_{ll}^{max}: The estimator for the endpoint in the invariant mass distribution of the signal.
- $\sigma_{m_{ll}}$: The constant describing the assumed experimental resolution for a single measurement of the invariant mass of two muons.
- N_{Sig}: The normalisation of the signal distribution.
- MPV: The most probable value of the Landau describing the combinatorial background.
- σ_{Landau}: The width of the Landau describing the combinatorial background.
- N_{Bkg}: The normalisation of the combinatorial background.

Thus, the location of the true best fit values is not a problem of lowest dimension, such that an advanced technique was used for the fits of the spectra, namely the method *BCHistogrammFitter::Fit()* which is included in the Bayesian Analysis Toolkit (BAT) [61].

The BAT package calculates full posterior probability density functions (pdfs) for the parameter space of a given model, which provides a prediction of the measured quantities. The actual predictions depend on the model parameters, $\vec{\lambda}$, and the model M itself. In order to include experimental effects that are not included in the pure theoretical model, a set of nuisance parameters, $\vec{\nu}$, is considered. By applying Bayes' Theorem for a fixed model the probability for a set of n parameters $\vec{\lambda}$ and n' nuisance parameters $\vec{\nu}$, given a set of experimental measurements $\vec{x} = \vec{D}$, can be calculated as

$$P(\vec{\lambda}, \vec{\nu}|\vec{D}) = \frac{P(\vec{x} = \vec{D}|\vec{\lambda}, \vec{\nu}) \cdot P_0(\vec{\lambda}, \vec{\nu})}{P(\vec{x} = \vec{D})}. \tag{5.14}$$

Here, P_0 is the prior probability for a set of (nuisance) parameters. The denominator in (5.14) is the probability for the experimental outcome $\vec{D}$ given any set of (nuisance) parameters, and

Set #	S/B before Cut	S/B after Cut	ϵ_S [%]	ϵ_B [%]
1	0.1518	0.4561	46.54	15.49
2	0.182	0.6436	52.16	14.75
3	0.2499	0.9594	59.09	15.39
4	0.429	1.127	33.41	12.72
5	0.4795	1.525	43.89	13.8
6	0.5351	1.785	61.99	18.58
7	0.5309	1.69	62.34	19.58
8	0.4476	1.525	63.11	18.52
9	0.3141	1.13	64.15	17.83
10	0.2152	0.7917	59.82	16.26
11	0.468	1.522	51.47	15.82
12	0.4925	1.697	54.68	15.87
13	0.484	1.473	67.5	22.18
14	0.1738	0.6036	65.28	18.8
15	0.1445	0.5084	68.94	19.59
16	0.4705	1.414	68.58	22.81
17	0.4504	1.317	67.88	23.22
18	0.4429	1.253	66.12	23.38
19	0.1677	0.5532	73.91	22.4
20	0.4467	1.2	64.88	24.15
21	0.4427	1.169	64.04	24.26
22	0.4367	1.08	62.07	25.11
23	0.1241	0.4198	75.16	22.22
24	0.4267	1.001	58.78	25.05
25	0.4157	0.9577	57.23	24.84
26	0.4018	0.8855	54.48	24.72
27	0.3747	0.7656	51.29	25.1
28	0.1124	0.3531	77.42	24.64

Table 5.2: Signal to background ratios and the p_T-cut efficiencies for both signal and background for all parameter points. For nearly all points, the signal efficiency is well above 50%, while the background efficiency is always smaller than 26%. The signal to background ratio is significantly improved by the cut for all points.

$P(\vec{x} = \vec{D}|\vec{\lambda}, \vec{\nu})$ is the probability for the measurement $\vec{D}$ given a specific set of (nuisance) parameters.

The so-called marginalised posterior pdf for a single parameter λ_i can be calculated from the full posterior pdf (5.14) by integrating out the dependence on all other parameters:

$$P(\lambda_i|\vec{D}) = \int_{i\neq j} d^{n-1}\lambda d^{n'}\nu P(\vec{\lambda}, \vec{\nu}|\vec{D}). \tag{5.15}$$

In this case, the measurements are the numbers of bin entries in the dimuon invariant mass histograms. For all parameter sets, a total number of 50 bins has been used, such that there is a total of 50 measurements for the estimation of the model parameters. Flat priors have been used (as by default), and the probability for a measurement $\vec{D}$ given a fixed set of (nuisance) parameters is the product of Poissonian distributions for each bin. The expectation values are

given by (5.13), i.e.

$$P(\vec{D}|\vec{\lambda},\vec{\nu}) = \prod_i \frac{e^{-\int_i f_{m_{ll}}^{FIT} dm_{ll}} \cdot \left(\int_i f_{m_{ll}}^{FIT} dm_{ll}\right)^{n_i}}{n_i!}, \tag{5.16}$$

where n_i denotes the actual number of entries in the ith bin, and $\int_i f_{m_{ll}}^{FIT} dm_{ll}$ is the expectation value for this bin. (5.16) implies the assumption of Poissonian uncertainties for each bin. In order to find the set of (nuisance) parameters which maximize the full posterior pdf (5.14), this pdf is determined using Markov Chain Monte Carlo (MCMC). A Markov Chain is a series of points $\vec{\lambda}_i$ in the parameter space, in which the pdf for the ith step depends only on the current position, $\vec{\lambda}_{i-1}$. Using a MCMC, a stationary posterior pdf is created, which is realised in BAT via the Metropolis algorithm. For the study presented here, a total of 500,000 iterations have been used in the MCMC. The parameter start values and allowed ranges have been chosen *by eye* in the first time, and have been improved in an iterative procedure, such that for each parameter set a total of 3-5 individual fits have been performed. Two of the final fits are shown as an example in figure 5.9. BAT estimates the goodness of the fit by the computation of a p-value. The p-values for all fits performed for the present study are listed in table 5.3, and it turns out that (nearly) all p-values indicate quite a good fit quality.

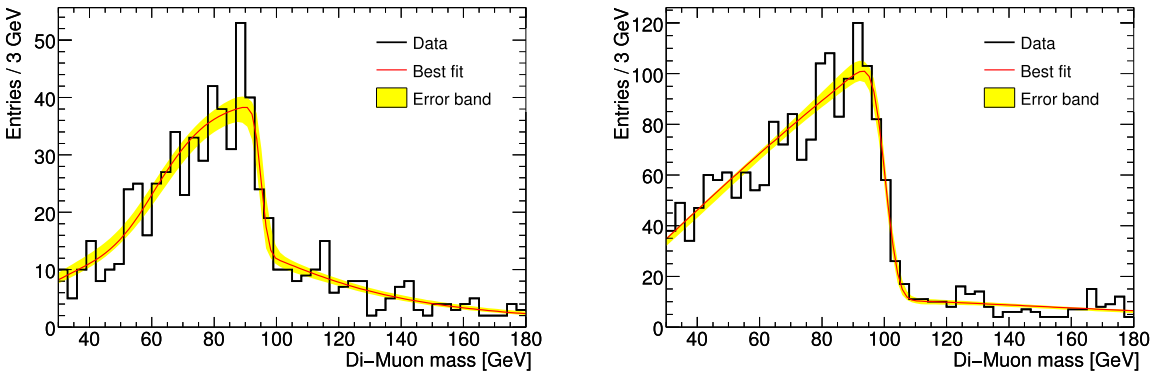

Figure 5.9: Results of two of the fits performed with BAT. (a) shows the reconstructed spectra with the best fit result including the uncertainty band for parameter set 1. In (b), the same plot is shown for parameter set 17. The p-values for the fits are (a) 0.65 and (b) 0.09.

For the estimation of the true kinematic endpoint (5.7), the median of the marginalised pdf for the parameter m_{ll}^{max} has been used, rather than the global mode of the full posterior pdf. Assuming a somewhat Gaussian behaviour of the marginalised pdf, the mean, the median and the mode should not be too different, such that in principle all three could be used. Nevertheless, with respect to the mean, the median is more robust against large deviators, and the mode of the marginalised pdf might experience small deviations from the *true* mode due to small statistical fluctuations and somewhat larger fluctuations due to the autocorrelation of the elements of the Markov Chain. The estimators determined in this way are listed in table 5.3, and an example for the marginalised posterior pdf for m_{ll}^{max} is shown in figure 5.10. The 0.16 and 0.84 quantiles are used for the quotation of the lower and upper uncertainties on the estimator.

Having extracted the endpoint estimators for all 28 parameter sets used, the final step was the determination of the parameters of the calibration curve (5.2). As a matter of fact, not all

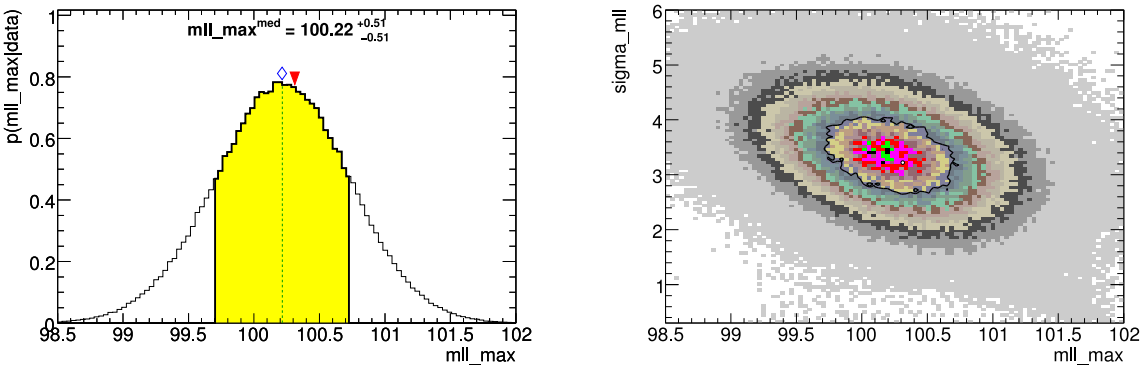

(a) (b)

Figure 5.10: Some more details of the fit for parameter set 17. (a) shows the marginalised posterior pdf for the kinematic endpoint in arbitrary units. The dashed line denotes the median, while the diamond and the triangle denote the mean and the global mode, respectively. The colored area marks the 16% and 84% quantiles of the distribution. In (b), the two dimensional posterior pdf for the endpoint m_{ll}^{max} and the nuisance parameter $\sigma_{m_{ll}}$ is shown in arbitrary units. The correlation at this parameter point is roughly -35%. These plots were automatically generated by BAT. The parameters mll_max and sigma_mll are given in GeV.

of the parameter sets have been used for this for two reasons: First, it can be seen from table 5.3, that for the five parameter sets 22, 24, 25, 26 and 27, the fitted values for the endpoint show significant upward fluctuations with respect to the true value. Obviously, this is also the case for some more sets, like the sets 1 and 2, but for the former mentioned points, a clear reason for the significant deviations can be given. This reason is the vicinity of the endpoint to the Z^0 peak, which after application of the p_T cut remains clearly visible in the respective spectra, as shown in figure 5.11(a), for example. The critical attribute of the parameter sets 22 and 24-27 is, that the theoretical endpoint in the signal spectrum is below the Z^0 pole mass (or, more precisely, below 93 GeV, which is the upper edge of the bin containing the Z^0 mass of ~ 91 GeV). This is as well the case for the points 1 and 6, but for these two points, as shown for point 6 in figure 5.11(b), the Z^0 contribution is nearly invisible. As the Z^0 pole is not explicitly included in the modelling of the background, the best fit value for the kinematic endpoint is pulled upwards, if the true value is only slightly smaller than the Z^0 mass. If the endpoint is still close to, but above the Z^0 mass, this is no longer a problem, as the peak is then simply absorbed in the triangular shape, causing an increase in the bin content of two or three bins and thus decreasing the p-value for the fit, but not washing out the kinematic edge. If the endpoint is below the Z^0 pole with a sufficient distance, the Z^0 peak does not affect the best fit value of the edge, as well. For this reason, the five parameter sets 22 and 24-27 have been excluded from the construction of the calibration curve.

The background model was not changed in order to include the Z^0 mass peak for two reasons. First, this would introduce additional parameters to the fit and is superfluous for the remaining 23 parameter sets for this first test. Thus point specific optimisations would have to be introduced, as there are evidently parameter sets with a significant number of Z^0 bosons in the SUSY decay chain which have nearly the same numerical endpoint in the dimuon spectrum as points in which sparticle decays into a Z^0 are strongly suppressed. The implementation of point specific optimisations was not desired at this point. Secondly, the addition of a *Breit-Wigner*

Set #	True Value [GeV]	Fitted Value [GeV]	p-Value of fit
1	92.23	$95.14^{+1.02}_{-1.15}$	0.65
2	95.82	$97.25^{+0.81}_{-0.74}$	0.97
3	99.99	$99.96^{+0.82}_{-0.66}$	0.77
4	52.94	$52.04^{+0.77}_{-0.57}$	0.06
5	62.11	$61.6^{+0.52}_{-0.49}$	0.74
6	92.05	$92.28^{+0.36}_{-0.4}$	0.66
7	96.04	$95^{+0.47}_{-0.62}$	0.38
8	99.96	$99.78^{+0.59}_{-0.45}$	0.82
9	104.11	$104.36^{+0.74}_{-0.88}$	0.28
10	108.07	$107.86^{+0.82}_{-0.9}$	0.84
11	71.16	$71.06^{+0.45}_{-0.53}$	0.73
12	74.92	$74.95^{+0.28}_{-0.29}$	0.94
13	104.01	$103.82^{+0.5}_{-0.5}$	0.5
14	120.93	$120.85^{+1.36}_{-1.66}$	0.94
15	130.16	$126.81^{+2.82}_{-3.13}$	0.06
16	101.87	$101.59^{+0.42}_{-0.51}$	0.65
17	100.18	$100.22^{+0.51}_{-0.51}$	0.09
18	97.99	$98.04^{+0.44}_{-0.44}$	0.65
19	140.06	$136.39^{+1.24}_{-1.33}$	0.96
20	95.87	$95.46^{+0.48}_{-0.51}$	0.17
21	94	$94.4^{+0.54}_{-0.53}$	0.9
22	91.96	$93.18^{+0.37}_{-0.3}$	0.64
23	150.56	$146.77^{+2.79}_{-3.35}$	0.27
24	89.71	$91.95^{+0.5}_{-0.53}$	0.89
25	88.08	$90.3^{+0.74}_{-0.76}$	0.73
26	84.45	$88.58^{+0.99}_{-0.97}$	0.16
27	81.43	$86.4^{+1.76}_{-1.96}$	0.01
28	158.75	$155.76^{+2.37}_{-2.47}$	0.01

Table 5.3: Fit results obtained with BAT. For each parameter set, the true value of the endpoint and the fitted value including statistical uncertainties are shown. In addition, the p-values for all fits are listed, which indicate a good goodness of fit for nearly all parameter points.

or a *Gaussian* to the background model, peaking at $\sim$ 91 GeV, would introduce the risk of underestimating the numerical value of the endpoint at these parameter points.

Still, not all of the remaining 23 parameter sets have been used for the construction of the calibration curve, as a test sample was needed to check the goodness of the assumption of a linear calibration curve. The parameter points 3, 5, 6, 9 and 23 have been chosen to constitute this test-sample. The choice was arbitrary, but it was paid attention that the whole range from $\sim$ 50 GeV to $\sim$ 160 GeV was covered by both the test sample and the sample used for the fit of the calibration curve.

For this fit, the class *TGraphAsymmErrors* as included in the *root*-software package [62] has been used. All the remaining 18 parameter sets have been used for the fit of the two parameters occurring in the linear calibration curve. In order to reduce the correlation between the slope

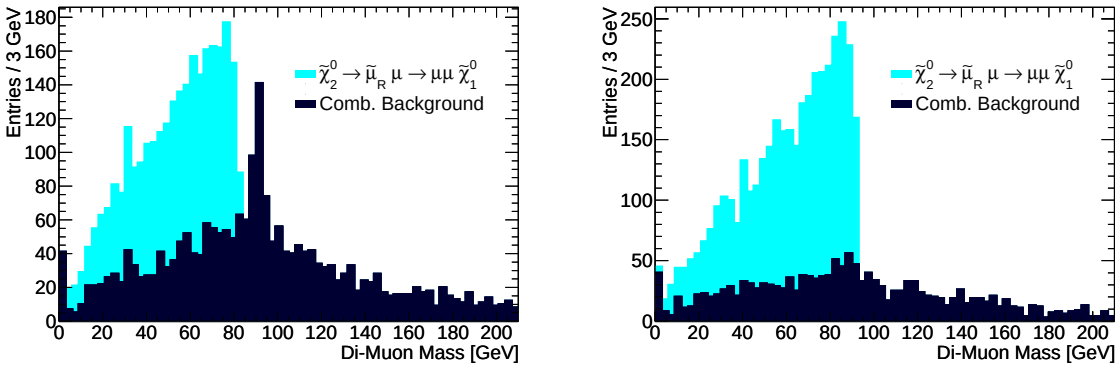

(a) (b)

Figure 5.11: (a) shows the invariant mass distributions for both signal and combinatorial background (generator level) at parameter point 27 after the application of the p_T-cut. It can clearly be seen that the Z^0 peak might influence a determination of the kinematic endpoint in the signal spectrum (the effect is even increased when detector effects are taken into account). In (b) the respective distribution for parameter point 6 is shown. At this point, no Z^0 peak is visible in the spectrum, which indicates that sparticle decays into Z^0 bosons are suppressed at this parameter point.

and the offset, a modified version of (5.2) has been used, namely

$$m_{ll}^{max,est.} = a' + b' \cdot \left(m_{ll}^{max,true} - 100 \text{ GeV} \right). \tag{5.17}$$

The result of the fit is shown in figure 5.12, and the fitted values of the slope $b' = 0.988 \pm 0.009$ and the offset $a' = (99.76 \pm 0.15)$ GeV are in good agreement with 1 and 100 GeV within 2 σ. However, the p-value of roughly 4% is relatively small. This might indicate an underestimation of the uncertainties on the estimator. The correlation between a' and b' is about 53%. If the fitted values for the slope and the offset of the calibration curve are applied to the test sample, a very good agreement between the true value and the extracted value is observed, as shown in table 5.4.

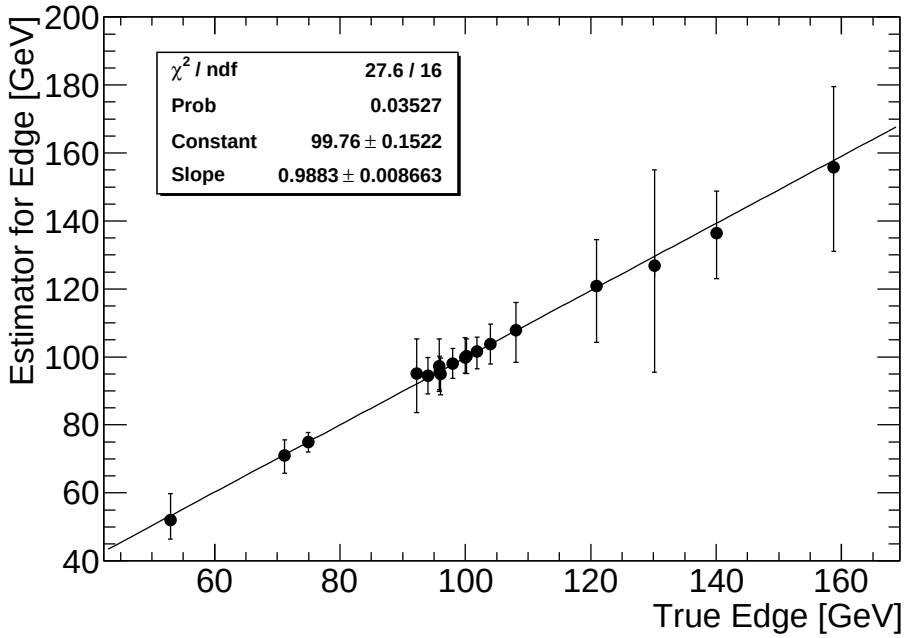

Figure 5.12: Fit of the calibration curve. 18 of 23 selected points were used to fit this straight line. On the x-axis, the true value of the kinematic endpoints are drawn, while the fitted values are shown on the y-axis. The error bars show the upper and lower uncertainties with a magnification factor of 10. The fit of a straight line yields quite a high χ^2 with a p-value of only 4%. The best fit slope and offset might indicate very small systematic effects, but within 2 σ they are in agreement with a straight line through the origin with slope 1.

True Value [GeV]	Fitted and "Gauged" Value [GeV]	Deviation [σ]
62.11	$61.39^{+0.69}_{-0.67}$	1.06
92.05	$92.43^{+0.21}_{-0.45}$	0.85
99.99	$100.20^{+0.85}_{-0.68}$	0.3
104.11	$104.65^{+0.76}_{-0.9}$	0.61
150.56	$147.57^{+2.85}_{-3.41}$	1.05

Table 5.4: Comparison of the results obtained with the constructed calibration curve (see figure 5.12) with the true values for the test sample. The deviations, expressed in terms of the uncertainties on the fitted and "gauged" values, are also quoted. In principle, the test with the control sample shows that for the given simplifications, the tested function is perfectly adequate for the determination of the kinematic endpoint (5.7).

The results show, that an unbiased estimator was found for the kinematic endpoint m_{ll}^{max}. The parametrisation of the measured signal distribution and the modelling of the combinatorial SUSY background have been proven to describe the Monte Carlo data very well. Given the explained approximations and assumptions, the tested method was shown to be successfull.

6 Systematic Uncertainties in Fits of SUSY-Lagrangians with the Program Fittino

In the previous section, one observable, which may be measurable at the LHC and be employed for SUSY parameter determination given that nature is actually supersymmetric, was examined. Now, the "final" step of SUSY parameter estimation is explained and performed on pseudo data. The focus in this section is on the program *Fittino* [35], which amongst other such programs [7, 63, 64], is one alternative for the extraction of SUSY Lagrangians from future data. After a short description of the functionality of the program, two new interfaces between *Fittino* and the programs *SoftSUSY* [37] and *SUSY-HIT* [65], which have been written in the context of this thesis, are introduced. With the implementation of these interfaces in the *Fittino* source code, systematic uncertainties on the *Fittino* results can be evaluated for the first time.

Some of the plots shown in this chapter were generated automatically. Therefore, two different labels for the parameters will be used. The parameter m_0 is sometimes referred to as M0, the parameter $m_{1/2}$ is sometimes labelled M12 and the parameter A_0 is sometimes labelled A0.

6.1 The Program *Fittino*

Fittino uses observables directly related to SUSY, as well as observables which are sensitive to SUSY only indirectly, to extract the MSSM parameters whose corresponding theoretical predictions of these observables fit best to the actual measured values. The difficulty of this endeavour was explained in section 3, where also two different approaches for the solution of the problem were illustrated. *Fittino* follows a top-down approach, although the estimation of the parameter start values may be done using bottom-up techniques. As the unconstrained MSSM contains 105 parameters, a fit of the complete, unconstrained model was futile. In order to retain the possibility to fit the parameters of the Lagrangian density, all complex phases, intergeneration mixing and mixing in the first two generations are set to zero, such that only 24 parameters remain [35]. In addition, high scale models like the GMSB, AMSB and mSUGRA model [24] can be fitted, which leaves even a smaller number of fit parameters.

Fittino is steered with an input file, which contains all used observables, the model and the parameters to be fitted. The measured values and the uncertainties need to be given for all observables. The uncertainties are assumed to be Gaussian for all observables and can be given as the sum of several distinct uncertainties. This has the advantage that the individual sources for the uncertainties can be named, and uncertainties of distinct observables arising from the same source (for example the jet energy scale) can be treated as 100% correlated. For the model parameters, start values and estimated uncertainties can be given. In addition, some switches for the fitting algorithms are set in the input file. In the current version, sparticle masses, branching ratios and production cross sections in electron-positron collisions can be used as observables. Furthermore, a number of already measured, so called *Low Energy* (LE) observables can be used, such as the anomalous magnetic moment of the muon $(g-2)_\mu$ [66, 67], or the branching

fraction $BF(b \to s\gamma)$ [68], which are sensitive to supersymmetric contributions. The sparticle masses can either be used directly, or embedded in kinematic edges, such as the one discussed in the previous chapter. *Fittino* currently knows the formulae for the most kinematic edges and kinks that may be measured at the LHC.

The fitting procedure is schematically shown in figure 6.1. Starting with the initial values for the parameters to be fitted, either obtained by tree-level estimates or as given in the input file, various external programs are called for the prediction of the used observables at the current point in the parameter space. For the SUSY observables, this is currently done with the program *SPheno* [36], while the LE Observables are calculated with the *Mastercode* package [69], which is a combination of *SoftSUSY*, FeynHiggs [70], SuperIso [71, 72], DarkSUSY [73] and MicrOMEGAs [74, 75]. The predicted values are then compared to the given "measured" values, and a χ^2 is calculated. Depending on the chosen fitting algorithm, *Fittino* jumps to a new point in the parameter space, for which a χ^2 is calculated in exactly the same way. By repeating this procedure until a convergence criterion is fulfilled or a termination condition is reached, the central values of the fit parameters are found. The final step is then the determination of the uncertainties on the best-fit values, which is done with *MINOS*.

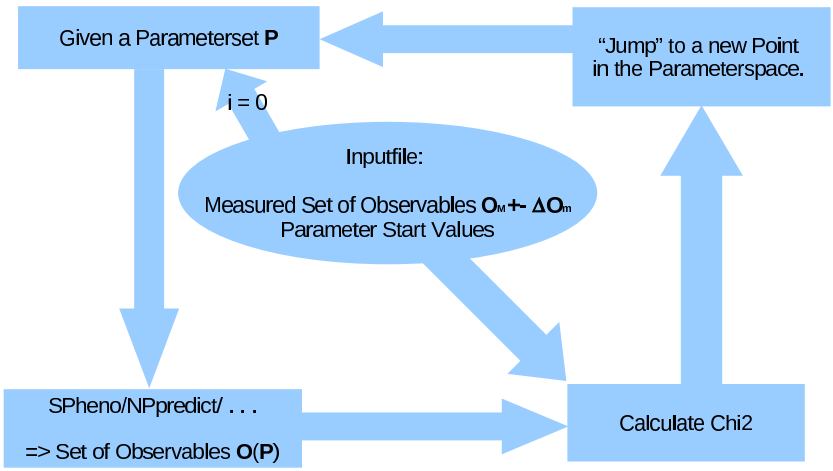

Figure 6.1: Schematics of the *Fittino* loop for the determination of the best-fit values. The communication between *Fittino* and the theory codes is done via the SUSY Les Houches file format. The input file contains information about the fitting algorithm(s) to be used and their configuration in addition to the observables, their uncertainties and the model with its parameters. Furthermore, switches for the output can be set.

Fittino offers three different methods for the determination of the best-fit parameters, the first of which is a *MINUIT* minimisation of the χ^2 function. As the MSSM parameter space is of high dimension, this can be done by performing fits in several subsectors of the MSSM parameter space first with most parameters fixed, before a global fit of all parameters is executed. The slepton or the squark mass parameters together with $\tan\beta$, or the stop and sbottom mixing

parameters are examples for parameter subsectors. However, due to the high dimensionality of the parameter space, more sophisticated techniques were implemented. One of these techniques, a MCMC has already been introduced in the previous section. In the present thesis, the third method, an implementation of a simulated annealing algorithm, is used. This is described in a bit more detail now, where the description is essentially taken from [35].

The basic idea of simulated annealing is to treat the χ^2-surface in the parameter space as a potential and to define a temperature t, from which the probability to jump to a certain point in the parameter space can be calculated. After the calculation of the χ^2 for the initial set of parameter values, each parameter P_i is varied within its assumed uncertainty (which is either given in the input file or determined by the tree level estimates) ten times. From the standard deviation of the corresponding χ^2-distribution, the initial temperature

$$t_0 = \frac{1}{2}\sigma_{\chi^2} \tag{6.1}$$

is derived. The value of t_0 can as well be given by hand in the input file. Now, each parameter is varied once and a new χ_i^2 is calculated after each variation. If $\chi_i^2 < \chi_{i-1}^2$, the new point is accepted and the algorithm continues with the variation of the next parameter. If the new point yields a worse χ^2, i.e. $\chi_i^2 > \chi_{i-1}^2$, a random number $p \in [0,1]$ is drawn and the new point is accepted if

$$p < e^{-\frac{\left(\chi_i^2 - \chi_{i-1}^2\right)}{t}}. \tag{6.2}$$

Otherwise, the new point is rejected. This allows the algorithm to escape from local minima in the χ^2-surface. The variation of the parameters is repeated 20 times each, and for all parameters the number of accepted new points is counted. In order to achieve a test range of

$$|\chi_i^2 - \chi_{i-1}^2| \approx t, \tag{6.3}$$

the estimated uncertainties for each parameter are iteratively varied, such that the fraction of accepted points $f_a = n_{accept}/n_{total}$ lies between 40% and 60%, which is achieved by

$$\Delta P_i^{new} = \Delta P_i^{old}\left(2\frac{f_a - 0.6}{0.4} + 1\right) \qquad \text{if} \quad f_a > 0.6, \tag{6.4}$$

$$\Delta P_i^{new} = \Delta P_i^{old}\frac{1}{\left(2\frac{0.4 - f_a}{0.4} + 1\right)} \qquad \text{if} \quad f_a < 0.4. \tag{6.5}$$

For n parameters, this is repeated $3n$ times, or at least 60 times if $n < 20$. Finally, the temperature is reduced by a constant reduction factor $r < 1$, and the whole procedure starts over again. Typically, a reasonable choice is $r \in [0.4, 0.6]$. The algorithm aborts if the maximum number of iterations as specified in the input file is reached, or if the variation of the χ^2 during the readjustment of the parameter step sizes is smaller than the variation within the four lowest χ^2 values found so far and the variation of all these values is smaller than 0.0001. If one of these criteria is matched, a final *MINUIT* minimisation and *MINOS* uncertainty analysis is performed.

The great advantage of using the simulated annealing algorithm is its capability to escape from local minima and its little dependence on the start values. Furthermore, in the beginning the algorithm may run over a large area in the parameter space due to high initial temperatures, while by reducing the temperature, the granularity of the fit in the vicinity of the assumed global minimum is increased. This ensures that the minimum found by the simulated annealing algorithm is very close to the true minimum and the minimum found by *MINUIT* in the final minimisation in most cases, which of course, comes by the cost of a relatively long run time.

6.2 New Interfaces to RGE-Codes for *Fittino*

External programs are needed for the prediction of the observables corresponding to a given point in the parameter space. So far, *Fittino* was only linked to *SPheno* for the prediction of the SUSY mass spectrum and the branching fractions. If, for example a high scale model like mSUGRA is fitted, *SPheno* solves the one- or two-loop renormalisation group equations and calculates the SUSY mass spectrum at the EWSB scale Q_{EWSB} for a given set of high scale parameter values. Masses are calculated to one-loop order, and two-loop corrections are added to the neutral Higgs bosons and the μ-parameter. The calculation is iteratively continued until a certain precision, which can be defined by the user, is reached. Finally, sparticle branching ratios and supersymmetric contributions to $(g-2)_\mu$ and $b \to s\gamma$ are computed. For a possible inclusion of future ILC measurements, *SPheno* also predicts SUSY production cross sections at an electron-positron collider, taking into account initial state radiation and longitudinal beam polarisation. A detailed description of the full functionality of *SPheno* can be found in [36].

It was mentionend in the previous chapter that for official ATLAS Monte Carlo, as well as for the private samples that were used for the construction of the calibration curve, the Fortran program *Isasugra* [56, 57] was used. If pseudo measurements of SUSY observables from analyses on this Monte Carlo were used as an input for *Fittino*, shifts in the best-fit values of the parameters with respect to the initial input values for *Isasugra* are expected due to differences between *Isasugra* and *SPheno*.

SoftSUSY and *SuSpect* are two additional packages which solve the RGEs and compute the SUSY couplings and masses at low scale for a given high scale input. Due to small pairwise differences between these codes, essentially four different sparticle spectra are obtained for the same given input. Therefore four different sets of best-fit parameters will be obtained when performing four individual fits of the Lagrangian parameters to the same measurements, each using one of the four spectrum calculators. These give rise to additional uncertainties on the parameters.

It is therefore essential to study the impact of the differences between *Isasugra*, *SoftSUSY*, *SPheno* and *SuSpect* on the values and uncertainties of the best-fit parameter values obtained by *Fittino*. Especially for large values of $\tan\beta$ and m_0 the differences in the predictions are known to become large [76]. Nevertheless, even if only small differences appear in the mass spectrum itself, the differences might become significant in the combination of the masses to more complex expressions like (5.7). It is the intend of this chapter to provide a first insight into these systematic uncertainties on the central parameter values obtained with *Fittino*, when a number of possible LHC measurements is used as input for the fit of an mSUGRA Lagrangian density.

For this purpose, the *Fittino* source code had to be extended in order to provide a link between *Fittino* and *SoftSUSY*/*SUSY-HIT*. However, an interface for *Isasugra* was not added, as the communication between Fittino and the external programs is done via the SUSY Les Houches Accord (SLHA) file format [77], which could not be used as an input for the available version of *Isasugra*.

6.2.1 Implementation of the new Interfaces

The *SUSY-HIT* Interface

The SUspect-SdecaY-Hdecay-InTerface (*SUSY-HIT*) is a package consisting of *SuSpect* [38] as a spectrum calculator, and the Fortran codes *SDECAY* [78] and *HDECAY* [79], which calculate decay widths and branching ratios of sparticles and MSSM Higgs bosons, respectively. Given

a general *SUSY-HIT* input file and an SLHA file which contains the SUSY breaking model and the corresponding parameter values, and in addition some *SuSpect* specific switches, first *SuSpect* is called for the calculation of the sparticle mass spectrum, after which *SDECAY* and *HDECAY* are executed. Whenever it is necessary, numerical values are translated between the $\overline{\text{MS}}$ and the $\overline{\text{DR}}$ scheme to retain consistency. *SUSY-HIT* can also be configured to leave out the *SuSpect* call, if a sparticle spectrum in the SLHA format is provided by another spectrum calculator. A more detailed description of the *SUSY-HIT* package is provided in [65].

The *SUSY-HIT* interface for *Fittino* is called if the value for the *Calculator* variable is set to *SUSPECT* in the *Fittino* steering file. *Fittino* then writes the general *SUSY-HIT* input file, requesting a call of *SuSpect* before *SDECAY* and *HDECAY* are called, and also an input file for *SuSpect* in the SLHA format, which, amongst other things, contains the numerical values of the current point in the parameter space. After the creation of the input files, *SUSY-HIT* is executed in a child process of the main program, which waits for the child process to finish. If a certain time limit, which can be set in the *Fittino* steering file, is exceeded, the child process is killed and the χ^2 is set to $1.1 \cdot 10^{11}$, such that a new point in the parameter space can be tested. This is a precaution to avoid that the spectrum calculator gets caught in an infinite loop, which is known to happen in some rare cases when *SPheno* is used and could not be excluded for *SuSpect*. If the *SUSY-HIT* run was successfull (i.e. it finished within the specified timelimit), an SLHA output file is written, which is read by *Fittino* for the calculation of the χ^2. Since *Fittino* needs some SM parameters and observables, which the programs included in *SUSY-HIT* do not write into their output by default, the *SUSY-HIT* routines were slightly changed to provide the relevant output.

A scheme of the *SUSY-HIT* interface when using *SuSpect* as a spectrum calculator is shown in figure 6.2(a).

The *SoftSUSY* Interface

For the inclusion of *SoftSUSY*, another interface was added to the *Fittino* source code. If the variable *Calculator* is set to *SOFTSUSY* in the *Fittino* input file, *Fittino* creates an SLHA input file for *SoftSUSY*, which is called in a child process, again. If *SoftSUSY* finishes the calculation within the timelimit, the general *SUSY-HIT* input file is written, telling the program to use the SLHA output of *SoftSUSY* as an input. The *SUSY-HIT* code is then executed, and the input is read in by *Fittino* as for the *SuSpect* case. The cycle for a *SoftSUSY* call is shown in figure 6.2(b). The *SoftSUSY* interface has been designed such, that in principle any other code calculating decay widths and branching fractions for sparticles and MSSM Higgs bosons can be used. Nevertheless, for the present study, only *SDECAY* and *HDECAY* as embedded in *SUSY-HIT* were used, if necessary. As for *SUSY-HIT*, minor modifications to the *SoftSUSY* code were necessary, such that it provides all output needed by *Fittino*.

The Electroweak Symmetry Breaking Scale

It should be noted here, that the *SoftSUSY* and *SUSY-HIT* interfaces in the current version automatically set $Q_{EWSB} = 1$ TeV. Q_{EWSB} is the scale at which the EWSB conditions are imposed during the calculation of the low energy parameters (before the sparticle spectrum is calculated at this scale). By default, all spectrum calculators use an estimate for Q_{EWSB} in the first iteration of the calculation, and later set $Q_{EWSB} = \sqrt{m_{\tilde{t}_1} \cdot m_{\tilde{t}_2}}$. However, all the codes used here allow the user to overwrite this default value, which had been applied for the *SPheno* interface in the "original" *Fittino* version. For comparability reasons, the same has been included in the new interfaces. This is at the moment hard coded in the *Fittino* source code.

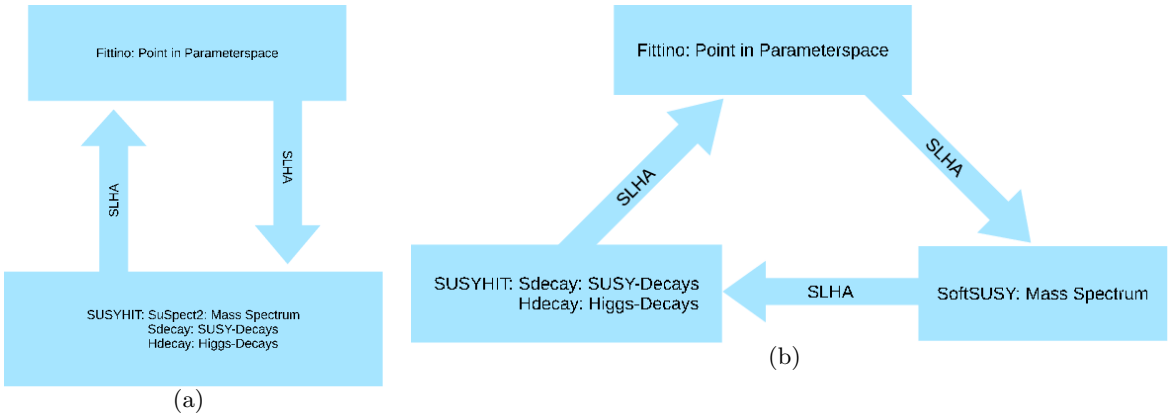

Figure 6.2: Schematic overview over the new interfaces. (a) When using *SuSpect* as a spectrum calculator, only one external executable is called, which is *SUSY-HIT*. As usual, the communication between *Fittino* and *SUSY-HIT* is done via the SLHA format. The substructure of *SUSY-HIT* is shown in the respective box. (b) shows the flow-chart for the *SoftSUSY* interface. When *SoftSUSY* is used for the calculation of the SUSY spectrum, *Fittino* hands the current parameter set to *SoftSUSY* via the SLHA, which creates a spectrum file in the SLHA format for *SUSY-HIT*, which is called afterwards.

Trivial Tests of the Interfaces

For a simple, trivial test of the interfaces, pseudo measurements have been calculated with *SoftSUSY* at the official ATLAS SU3 benchmark point and mSUGRA Lagrangians have been fitted to these pseudo measurements using that very same spectrum calculator during the fit. The same was done using *SuSpect* for both the input and the fit. Table 6.1 shows the list of input observables, which at this point have been chosen disregarding their measurability at the LHC. In addition, the uncertainties are rough and somewhat arbitrary estimates, as the only goal of this test is the demonstration of the basic functionality of the interfaces. It has rather been paid attention that the slepton-, squark- and neutralino/chargino sectors are all included, although not all sparticles appear in the input file, of course. The simulated annealing algorithm with a maximum number of 60,000 calls has been used for two independent fits with different parameter start values, which were explicitly defined in the input file rather than being estimated by tree level approximations. The first chosen set of start values equals the input values, i.e.

$$\begin{aligned} m_0 &= (100 \pm 30)\text{GeV} & m_{1/2} &= (300 \pm 90)\text{GeV} & A_0 &= (-300 \pm 650)\text{GeV} \\ & & \tan\beta &= 6 \pm 7 & \text{sgn}\mu &= 1, \end{aligned} \tag{6.6}$$

where *Fittino* takes care that always $\tan\beta > 0$. The second set of start values was chosen as

$$\begin{aligned} m_0 &= (76 \pm 30)\text{GeV} & m_{1/2} &= (331 \pm 90)\text{GeV} & A_0 &= (383 \pm 650)\text{GeV} \\ & & \tan\beta &= 13.2 \pm 7.2 & \text{sgn}\mu &= 1. \end{aligned} \tag{6.7}$$

These are approximately the best-fit values obtained by *Fittino*, if only LE observables are used for the fit of an mSUGRA Lagrangian with fixed $\text{sgn}\mu = +1$ using the *Mastercode* [80]. The results for the fits are summarised in table 6.2, while the evolution of the parameters and the χ^2 during the run of the simulated annealing algorithm are shown in figures 6.3 and 6.4. From these tables and figures it can be concluded that the interfaces to *SuSpect* and *SoftSUSY* are

Observable	Value (*SoftSUSY*)	Value (*SuSpect*)
α_{em}	127.925 ± 0.016	127.925 ± 0.016
G_F	$1.166 \cdot 10^{-5} \pm 10^{-10}$	$1.166 \cdot 10^{-5} \pm \cdot 10^{-10}$
α_s	0.1176 ± 0.0020	0.1176 ± 0.0020
m_Z	(91.1875 ± 0.0021) GeV	(91.1875 ± 0.0021) GeV
m_b	(4.83 ± 0.17) GeV	(4.83 ± 0.17) GeV
m_t	(172.4 ± 0.01) GeV	(172.4 ± 0.01) GeV
m_τ	(1.77684 ± 0.00017) GeV	(1.77684 ± 0.00017) GeV
m_W	(80.314 ± 0.025) GeV	(80.480 ± 0.025) GeV
m_{h_0}	(109.5 ± 5.0) GeV	(110.3 ± 5.0) GeV
$m_{\tilde{\chi}_1^+}$	(223.7 ± 5.0) GeV	(222.6 ± 5.0) GeV
$m_{\tilde{\chi}_2^+}$	(476.6 ± 5.0) GeV	(479.1 ± 5.0) GeV
$m_{\tilde{\chi}_1^0}$	(118.8 ± 5.0) GeV	(118.7 ± 5.0) GeV
$m_{\tilde{\chi}_2^0}$	(223.2 ± 5.0) GeV	(223.0 ± 5.0) GeV
$m_{\tilde{\chi}_3^0}$	(458.5 ± 10.0) GeV	(462.9 ± 10.0) GeV
$m_{\tilde{\chi}_4^0}$	(474.0 ± 10.0) GeV	(479.7 ± 10.0) GeV
$m_{\tilde{u}_R}$	(639.3 ± 10.0) GeV	(642.4 ± 10.0) GeV
$m_{\tilde{u}_L}$	(654.4 ± 10.0) GeV	(662.9 ± 10.0) GeV
$m_{\tilde{\nu}_{e,L}}$	(216.8 ± 5.0) GeV	(215.7 ± 5.0) GeV
$m_{\tilde{\nu}_{\tau,1}}$	(215.1 ± 5.0) GeV	(215.1 ± 5.0) GeV
$m_{\tilde{\tau}_1}$	(151.6 ± 5.0) GeV	(149.8 ± 5.0) GeV
$m_{\tilde{\tau}_2}$	(232.5 ± 5.0) GeV	(230.7 ± 5.0) GeV
$m_{ll}^{max}\left(\tilde{\chi}_1^0, \tilde{\chi}_2^0, \tilde{\mu}_R\right)$	(103.8 ± 5) GeV	(103.2 ± 5) GeV
$\lvert m_{\tilde{g}} - m_{\tilde{\chi}_1^0}\rvert$	(597.3 ± 10) GeV	(598.9 ± 10) GeV
$\mathrm{BF}(\tilde{\chi}_2^0 \to \tau\tilde{\tau}_1)$	0.266 ± 0.100	0.250 ± 0.100
$\mathrm{BF}(\tilde{\chi}_2^0 \to e\tilde{e}_R)$	0.0345 ± 0.0200	0.0298 ± 0.0200
$\mathrm{BF}(\tilde{g} \to b\tilde{b}_1)$	0.091 ± 0.020	0.086 ± 0.020
$\mathrm{BF}(\tilde{b}_1 \to b\tilde{\chi}_2^0)$	0.268 ± 0.020	0.264 ± 0.020

Table 6.1: Observables used for the trivial tests of the interfaces. All mass sectors (squarks, charged and neutral sleptons and gauginos/higgsinos) are included. Furthermore, four branching ratios have been used to test the compatibility of the *SDECAY* and *HDECAY* output. The given numerical values correspond to the *SoftSUSY* / *SuSpect* (masses) and *SDECAY* (branching ratios) predictions for the ATLAS SU3 benchmark point. The uncertainties are only arbitrary guesses.

(a)

Name	Start	Best-Fit
m_0[GeV]	100	99.7 ± 5.3
$m_{1/2}$[GeV]	300	299.9 ± 2.5
A_0[GeV]	-300	-300.2 ± 40.5
$\tan\beta$	6	6.0 ± 1.4

(b)

Name	Start	Best-Fit
m_0[GeV]	76	99.7 ± 5.3
$m_{1/2}$[GeV]	331	299.9 ± 2.5
A_0[GeV]	383	-300.2 ± 40.5
$\tan\beta$	13.2	6.0 ± 1.4

(c)

Name	Start	Best-Fit
m_0[GeV]	100	99.9 ± 5.3
$m_{1/2}$[GeV]	300	300.0 ± 2.5
A_0[GeV]	-300	-299.4 ± 37.8
$\tan\beta$	6	6.0 ± 1.3

(d)

Name	Start	Best-Fit
m_0[GeV]	76	99.9 ± 5.1
$m_{1/2}$[GeV]	331	300.0 ± 2.4
A_0[GeV]	383	-299.4 ± 40.3
$\tan\beta$	13.2	6.0 ± 1.4

Table 6.2: Results for the trivial tests of the *SUSY-HIT* and the *SoftSUSY* interfaces. Tables (a) and (b) show the results obtained with *SoftSUSY* for the two different start-points, tables (c) and (d) quote the respective results for *SuSpect*.

working fine for fits of the mSUGRA model, although there are some phases during the fit in which the simulated annealing algorithms gets stuck in regions with very high χ^2. This is known to happen when using *SPheno* as well, which means that it is not a fundamental problem of the written interfaces. An explanation for the behaviour might be that the algorithm runs into regions which are incompatible with the given observables. For example, if the $\tilde{\mu}_R$ is heavier than the $\tilde{\chi}_2^0$ in these regions, the prediction for the endpoint (5.7), which is used as an observable here, yields "nan", such that *Fittino* forces $\chi^2 = 1.1 \cdot 10^{11}$.

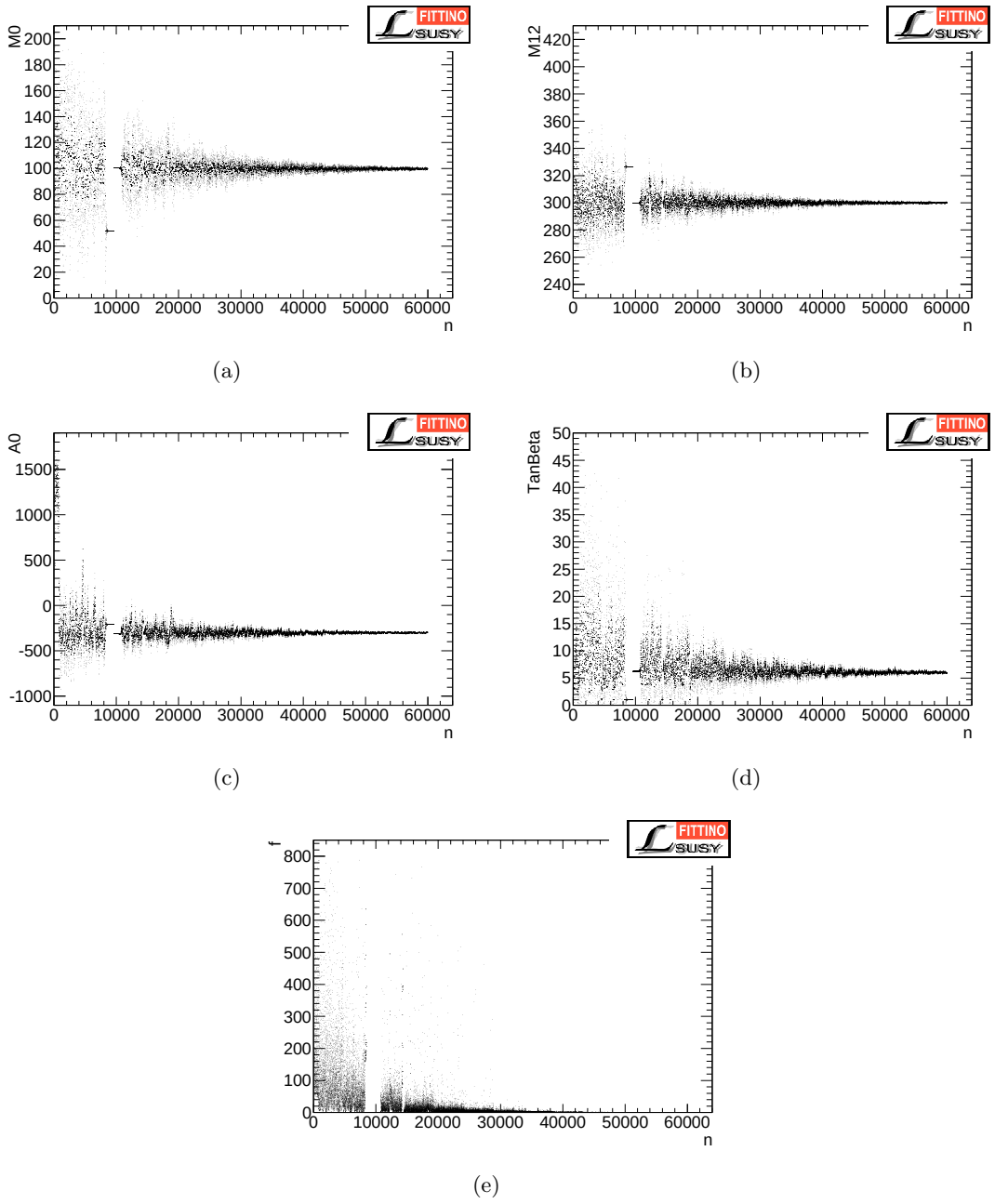

Figure 6.3: The behaviour of the four parameters m_0 in (a), $m_{1/2}$ in (b), A_0 in (c) and $\tan\beta$ in (d), during the run of the simulated annealing algorithm. The x-axis shows the number of iterative steps, the y-axis the value of the respective parameter at this step. Although there are regions at which the algorithm gets stuck in unphysical regions, the freeze-out of the parameters can nicely be seen. Finally, (e) shows the behaviour of the χ^2.

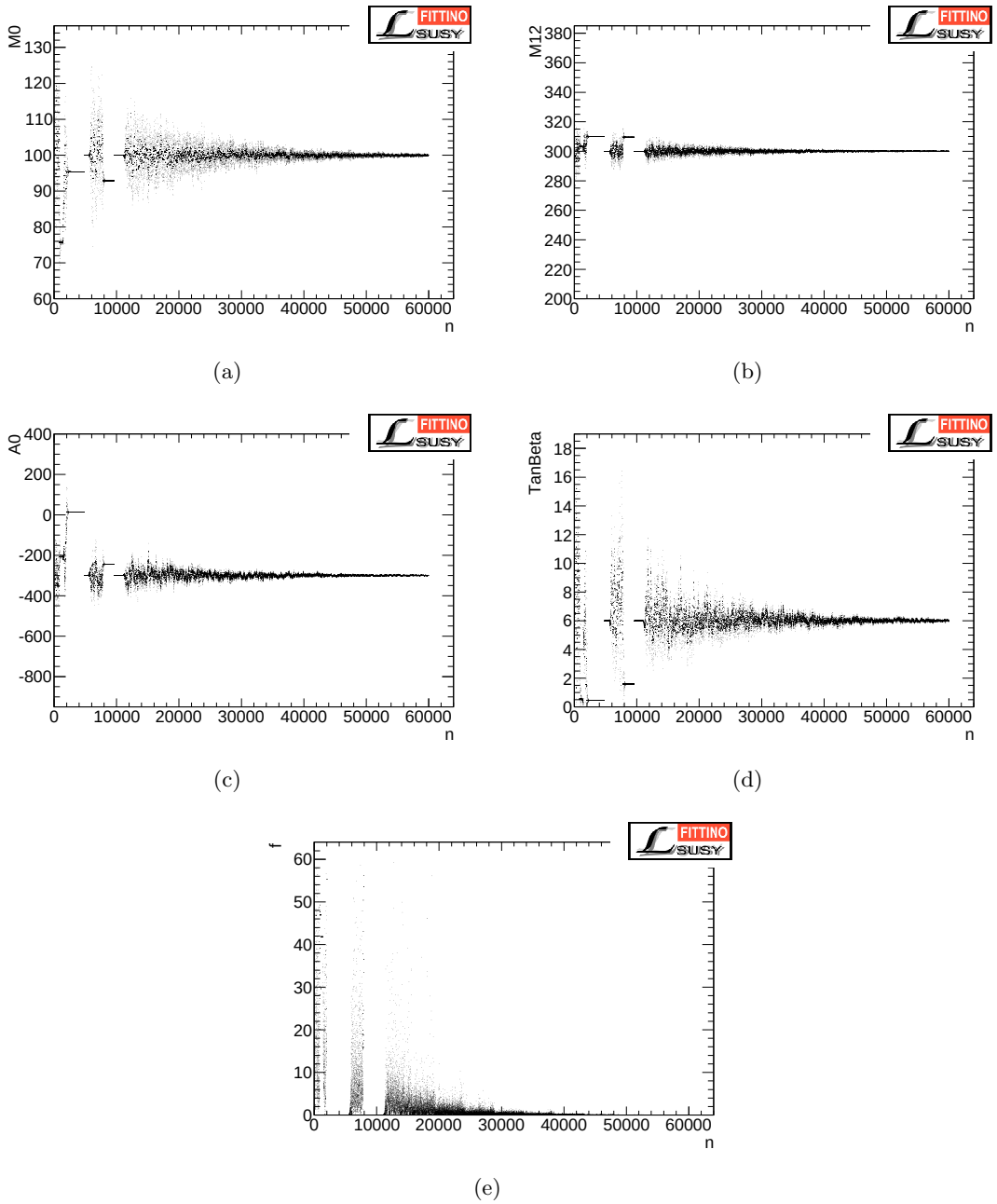

Figure 6.4: The behaviour of the parameters when using *SuSpect* as spectrum calculator. (a) shows m_0, (b) shows $m_{1/2}$, while (c) and (d) show A_0 and $\tan\beta$. The evolution of the χ^2 is again shown in (e).

6.2.2 Differences in the available RGE-Codes

Since this is not a thesis on the theory of supersymmetry, the main sources for the differences between the four codes *Isasugra*, *SPheno*, *SoftSUSY* and *SuSpect* are described only very briefly at this point. Some comparing plots are shown at the end of this section. One of the differences between *Isasugra* and the other three codes is the use of different renormalisation schemes during some parts of the calculation [76]. Moreover, the codes use different order loop-corrections for the calculation of some of the spectrum sectors [76]. Finally, numerical differences in the initial estimation for the bottom Yukawa coupling h_b may lead to significant differences in the spectrum, especially at large values of $\tan\beta$, while differences in the respective top Yukawa coupling h_t cause corresponding deviations for large m_0 [81]. A more detailed treatment of the differences can for example be found in [76] and [81].

In figures 6.5 and 6.6, a comparison of the mass spectra obtained with *Isasugra*, *SoftSUSY*, *SPheno* and *SuSpect* is shown for one of the parameter points examined in the next section as an example. Although the deviations observed in the prediction of the masses are mostly small, they may lead to clear shifts in the central values of the parameters.

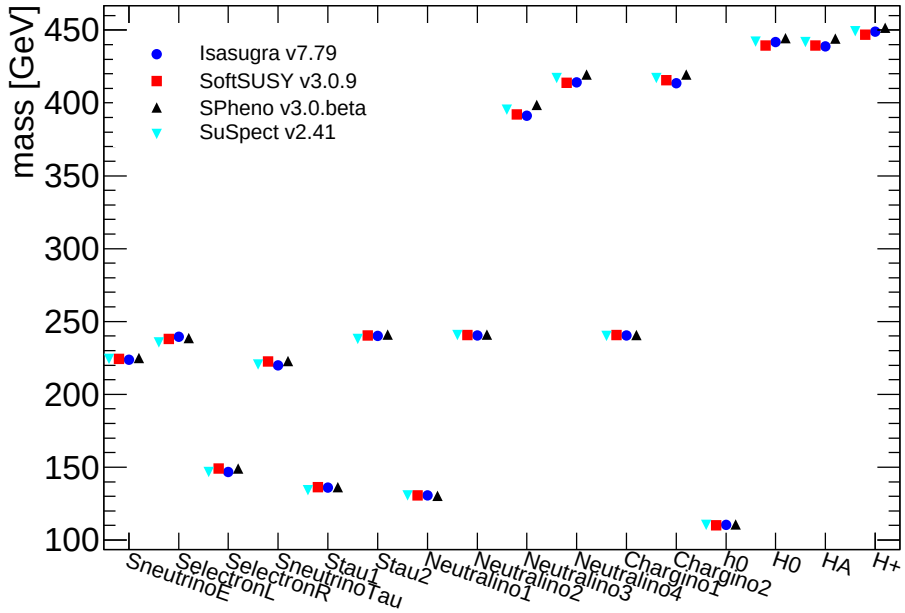

Figure 6.5: Comparison of the prediction of the "light" sparticles' masses according to *Isasugra*, *SPheno*, *SoftSUSY* and *SuSpect* for the same mSUGRA input parameters. The differences, although very small, can clearly be seen, especially for the heavy neutralinos, chargino and Higgses, where *SPheno* and *SuSpect* show a tendency to slightly higher values.

6.3 Comparisons of Fit Results with *SoftSUSY*, *SPheno* and *SuSpect*

For the comparison of the three software packages which can be interfaced to *Fittino* via the SLHA format, a small interval on the $m_{1/2}$-axis in the mSUGRA parameter space is examined.

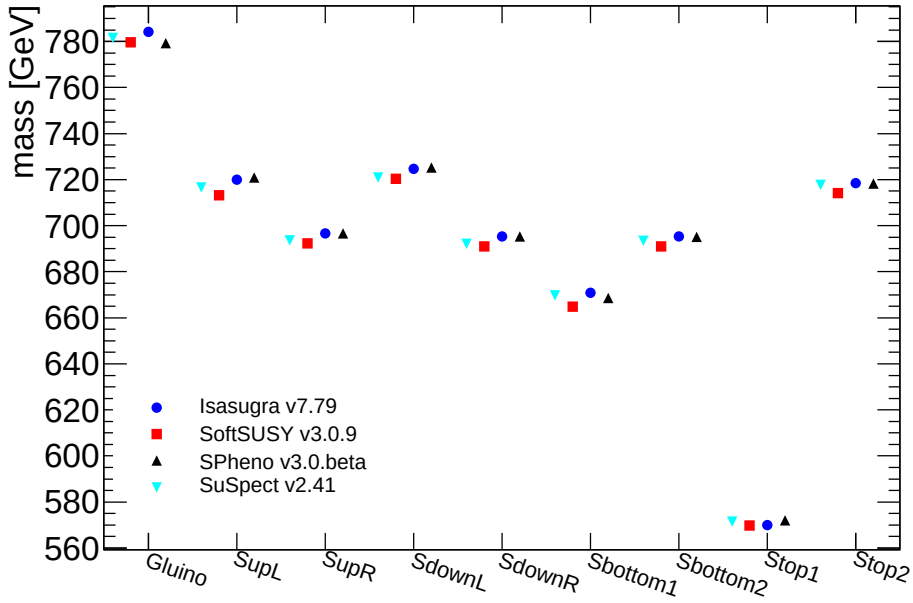

Figure 6.6: This diagram shows the comparison of the coloured sparticles' masses as predicted by *Isasugra*, *SPheno*, *SoftSUSY* and *SuSpect* for the same given mSUGRA parameters. For reasons explained in chapter 2 these sparticles are typically heavier than the sleptons and gauginos, such that absolute difference in the predictions are more obvious, here. For the superpartners of light quarks, *Isasugra* and *SPheno* seem to predict higher values, while for the third generation squarks *SoftSUSY* predicts lower masses than the three other spectrum calculators. If these masses are used for the prediction of kinematic edges in invariant mass spectra from SUSY decay chains, the shown differences may lead to significant deviations.

Eleven or twelve mass edges, which are expected to be measurable at the LHC given that the respective parameter set is realised in nature, are used as an input; no LE observables are used. Distributions for all parameters are obtained separately for each spectrum calculator. This way, a detailed comparison of the central values and the uncertainties is provided following a frequentist approach, and correlations between the best-fit values can be calculated.

6.3.1 Method

For each of the parameter points listed in table 6.3, the sparticle masses were calculated with *Isasugra*7.79. From this mass spectrum, the desired mass edges were calculated and put into the *Fittino* input file as pseudo measurements. This way, at least the central values of the mSUGRA parameters obtained with *SPheno*, *SoftSUSY* and *SuSpect* can be compared to the corresponding *Isasugra* values. It is obvious that, if *Isasugra* was used for both the calculation of the pseudo measurements and the fit procedure, the mean value of the respective parameter distributions were equal to the input values within statistical errors, just as it is the case for the other calculators (see previous section). However, *Isasugra* uses $Q_{EWSB} = \sqrt{m_{\tilde{t}_1} \cdot m_{\tilde{t}_2}}$, since it was not possible for this code to specify the EWSB scale by hand. The error caused by this inconsistency is absorbed in the calculation of the total uncertainties on the observables

(see below). Details of the examined parameter space and the observables follows in the next sections.

If *Fittino* is configured to calculate pull distributions, the input observables are smeared according to a Gaussian distribution whose mean value and width correspond to the given observable value and uncertainty. For a single run, a random seed needs to be given to *Fittino*, from which a single smeared set of observables is thrown and used for the fit of the model parameters. If this is repeated for a reasonable number of different random seeds, the user gets absolute and pull distributions for all observables and parameters. The pull distributions refer to the input (start) values and the measured (estimated) uncertainties of the observables (parameters). For the present study, only the absolute distributions have been used. From these parameter distributions the central value and the uncertainty can be determined. Since *Fittino* assumes all uncertainties to be Gaussian, if the region in the parameter space is sufficiently smooth, the distributions of the parameters are expected to be Gaussian, as well. The constitution of a Gaussian parameter distribution from a Gaussian observable distribution is sketched in figure 6.7. However, the occurrence of side minima, unrecognised correlations between observables and a non-continuous behaviour of the χ^2-surface in the parameter space may cause non-Gaussian parameter distributions. This may occur if for example the χ^2 surface contains steps near the best-fit values. If, as an example, a certain decay chain becomes kinematically available with a high branching fraction within a small variation in the parameter space, a non-Gaussian behaviour of the parameter distributions is expected.

The creation of parameter distributions offers several advantages for the comparison to be performed here. The distributions obtained by using one spectrum calculator can be compared with the distributions obtained by using the other calculators, such that shifts in the best fit values and the uncertainties become directly visible. Furthermore, if a sufficiently large sample of smeared observable sets is thrown, the linear correlation coefficients can be calculated. If the differences in the best-fit values are pure systematic shifts, the results for the single fits are expected to be highly correlated.

Each set of smeared observables was individually fitted using the simulated annealing algo-

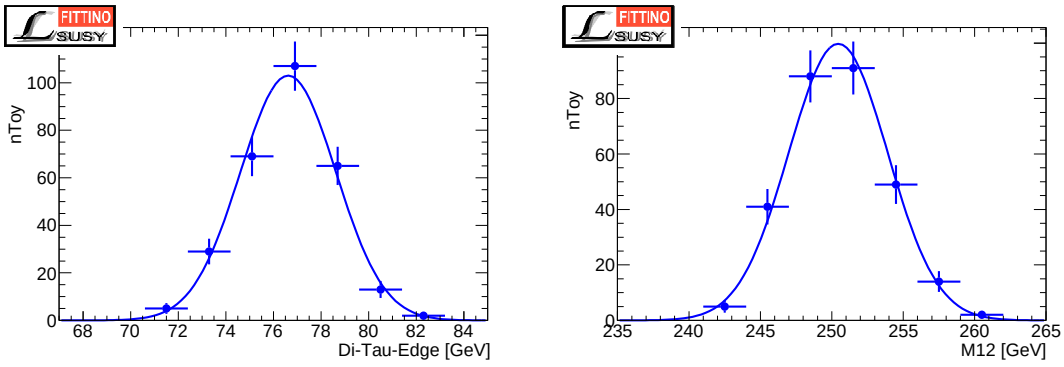

(a) (b)

Figure 6.7: Example for the translation of a (a) Gaussian observable distribution into a (b) Gaussian parameter distribution when pull distributions (not shown here) are calculated by *Fittino*. However, the occurrence of side minima, unrecognised correlations between observables and a non-continuous behaviour of the χ^2-surface in the parameter space may cause non-Gaussian parameter distributions.

rithm with a maximum of 60,000 iterations for all three implemented spectrum calculators. This corresponds to an average duration of one day per fit using *SPheno*, three days per fit when using *SoftSUSY* and four days per fit when using *SuSpect*. The initial temperature for the fits is calculated from the χ^2 corresponding to the parameter start values, which are set to the *Isasugra* input values, while the temperature reduction coefficient was set to 0.5. A total of 100 smeared sets of observables were thrown for each of the used parameter points, which are discussed in the following.

6.3.2 Parameterspace

The part of the mSUGRA parameter space for which toy measurements were created and fits with each of the three usable RGE-codes were performed is listed in table 6.3. The fixed values roughly correspond to the best fit values for an mSUGRA fit with fixed signμ=+1, if only LE observables are used for the fit, whose SUSY corrections are predicted by the *Mastercode*. The $m_{1/2}$-interval roughly corresponds to the 1-σ-interval obtained by this fit. The details for the LE fit can be found in [80]. A variation of $m_{1/2}$ for this comparison has been chosen as the 1-σ-interval is of an appropriate size, such that with a step width of $\Delta m_{1/2} = 10$ GeV a total of 17 parameter points can be compared. This way, a reasonable range in the mass spectrum is examined, while a realistic though significant amount of computing power is needed - a total of 5100 fits had to be performed (3 Calculators and 100 smeared observable sets per parameter point), which was done on the LHC computing grid. Furthermore, the cross section at the LHC for all points under investigation here is high enough to provide the used set of observables at an integrated luminosity of 300 fb^{-1}, as shown in figure 6.8.

Parameter	Value/Range
m_0	70 GeV
$m_{1/2}$	[250,410] GeV
A_0	400 GeV
$\tan\beta$	13
signμ	+1

Table 6.3: Parameter space used for the comparison of the three RGE-codes. Only the gaugino mass parameter was varied, the other parameters were fixed near the best fit values obtained by fitting the mSUGRA Lagrangian to LE observables, only.

6.3.3 Observables

A number of observables which are expected to be measurable at the LHC when a dataset of 300 fb^{-1} at $\sqrt{s} = 14$ TeV has been collected [82] were used as an input for the fit. First, the mass of the lightest neutral Higgs boson, m_{h_0} is used, which could for example be measured in the decay $h_0 \to \tau\tau$ [59]. The mass of the lightest chargino, $m_{\tilde{\chi}_1^+}$ is the second mass which is used directly. By exploiting the decay chain

$$\tilde{q}_L \to q\tilde{\chi}_1^+ \to qW\tilde{\chi}_1^0 \to qqq\tilde{\chi}_1^0,$$

this can be measured up to a two-fold ambiguity [83]. Three edges of the type discussed in the previous chapter are used for measurements in the neutralino and slepton sector. These are measured by determining the kinematic endpoints in the $m_{\mu\mu}$ and $m_{\tau\tau}$ spectra arising from the

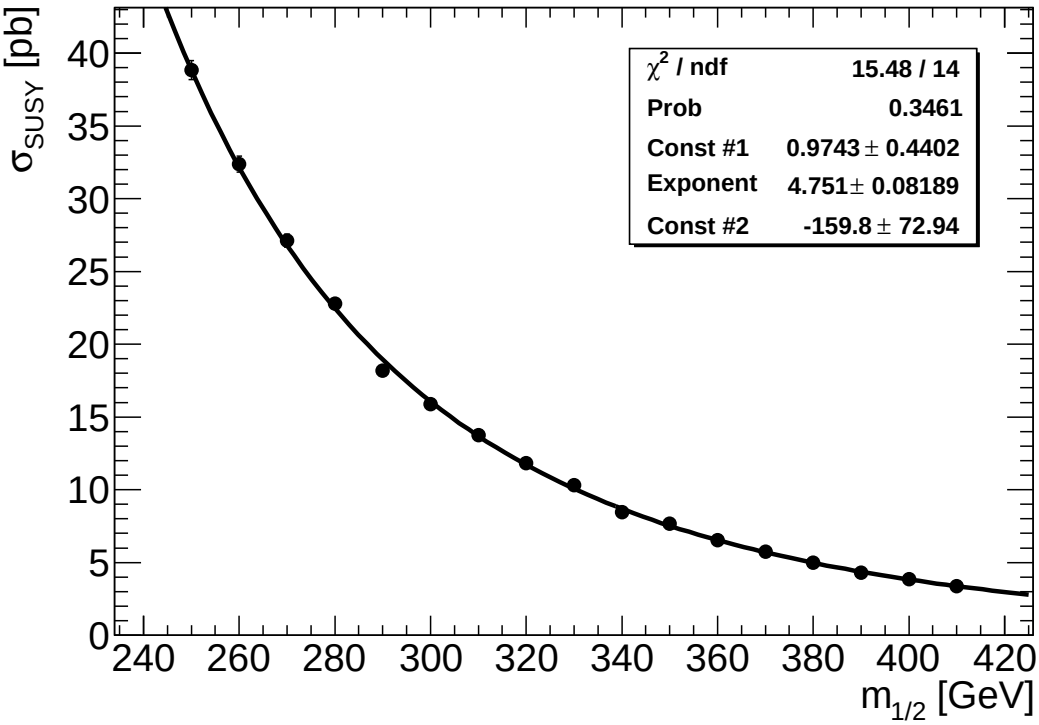

Figure 6.8: Total SUSY production cross sections at the LHC for $\sqrt{s} = 14$ TeV with respect to $m_{1/2}$, for fixed $m_0 = 70$ GeV, $\tan\beta = 13$, $A_0 = 400$ GeV and sign$\mu = +1$. It turned out that the behaviour is well described by the ansatz $\sigma_{tot}(m_{1/2}) = \frac{\text{Const } \#1}{m_{1/2}^{\text{Exponent}}} - \frac{\text{Const } \#2}{m_{1/2}}$. This can qualitatively be understood, as with increasing $m_{1/2}$ the gluino mass increases (as well as, by loop corrections, the squark masses). Since the dominant SUSY production processes at the LHC are squark and gluino production, the cross section decreases with increasing $m_{1/2}$.

decay chains

$$\begin{array}{lcll} \tilde{\chi}_2^0 & \rightarrow & \mu\tilde{\mu}_R \rightarrow \mu\mu\tilde{\chi}_1^0, & \\ \tilde{\chi}_2^0 & \rightarrow & \tau\tilde{\tau}_1 \rightarrow \tau\tau\tilde{\chi}_1^0 & \text{and} \\ \tilde{\chi}_4^0 & \rightarrow & \tau\tilde{\tau}_2 \rightarrow \tau\tau\tilde{\chi}_1^0. & \end{array} \tag{6.8}$$

The endpoints in the ditau spectra can of course not be measured directly, as the taus undergo hadronic or leptonic decays including neutrinos and are not measured directly. Nevertheless, techniques have been developed to derive the endpoint from the spectra of the visible decay products [59]. An analysis of the decay chain

$$\tilde{g} \rightarrow b\tilde{b}_{1,2} \rightarrow bb\tilde{\chi}_2^0 \rightarrow bbl\tilde{l}_R \rightarrow bbll\tilde{\chi}_1^0$$

yields a measurement of $m_{\tilde{g}} - m_{\tilde{\chi}_1^0}$ [82]. Information about the charged sleptons is completed by measuring $\sqrt{m_{\tilde{l}_L}^2 - 2m_{\tilde{\chi}_1^0}^2}$ from electroweak s-channel Z/γ exchange dislepton production and

the subsequent decay

$$\tilde{l}_L \to l\tilde{\chi}_1^0$$

using the *stransverse mass* m_{T2} [84, 85]. For the superpartners of the right-chiral quarks, by using the stransverse mass again, roughly $\sqrt{m^2_{\tilde{q}_R} - 2m^2_{\tilde{\chi}_1^0}}$ can be measured exploiting the decay [80, 82]

$$\tilde{q}_R \to q\tilde{\chi}_1^0.$$

The measurement of an edge in the invariant mass distribution of the quark and one of the leptons originating from the squark decay,

$$\tilde{q}_L \to q\tilde{\chi}_2^0 \to ql\tilde{l}_R \to qll\tilde{\chi}_1^0$$

includes information about the superpartners of the left-chiral quarks in the fit. This variable is referred to as m_{lq}^{high}, and is defined as

$$m_{lq}^{high} = \max\left(m_{lq}^{near}, m_{lq}^{far}\right), \tag{6.9}$$

where *near* and *far* refer to the lepton, as in the previous chapter. Instead of using m_{lq}^{near} and m_{lq}^{far}, the spectra of m_{lq}^{high} and correspondingly m_{lq}^{low} are typically used since it is impossible to assign the attributes *near* and *far* to the leptons correctly on data. Finally, the stop and sbottom sector are included in the comparison via endpoints in the invariant mass distribution of the top-bottom pair originating from the decay chains [82, 86]

$$\begin{aligned} \tilde{g} &\to t\tilde{t}_1 \to tb\tilde{\chi}_1^+ \qquad \text{and} \\ \tilde{g} &\to b\tilde{b}_i \to tb\tilde{\chi}_1^+. \end{aligned} \tag{6.10}$$

All edges are sufficiently separated from each other for the parameterspace used here, such that no branching ratio weighted combinations need to be used, as it is the case for the SPS1a benchmark point, for example [80]. The endpoints in the m_{tb} spectra are in principle analogons of the edges in the invariant dilepton mass spectra, but due to the high top mass the high energy approximation must not be applied for the calculation of the numerical values, such that in principle (5.4) has to be used instead of (5.5). This complicates the final formulae for the endpoints, which can be found in [86].

With this choice of observables, a wide range of the SUSY mass spectrum is covered. Information is missing only about the $\tilde{\chi}_3^0$, the $\tilde{\chi}_2^+$ the $\tilde{t}_2$ and the complete sneutrino sector, as these will most likely be hard to measure at the LHC with sufficient accuracy. In addition, default values of some SM observables, such as the masses of the Z, W, τ and the b-quark, as well as the strong and electromagnetic coupling constants α_s and α_{em} are used (Fittino would use default values for these, anyway). The evolution of the observables as predicted by *Isasugra* with respect to $m_{1/2}$ is shown in figure 6.9. The variable $m_{tb}^{max}(\tilde{t}_1)$ was not used for $m_{1/2} < 280$ GeV, as the necessary decay chain is kinematically forbidden in this region. Furthermore, for $m_{1/2} > 350$ GeV, the observable $m_{\tau\tau}^{max}(\tilde{\chi}_2^0, \tilde{\chi}_1^0, \tilde{\tau}_1)$ could not be used as the respective decay chain is forbidden for these points, too. Together with the SM observables, a total of 21 or 20 observables have been used.

The estimation of experimental uncertainties mainly relies on [80] and [82]. The experimental uncertainties are estimated using the expected uncertainties at the SPS1a parameter point.

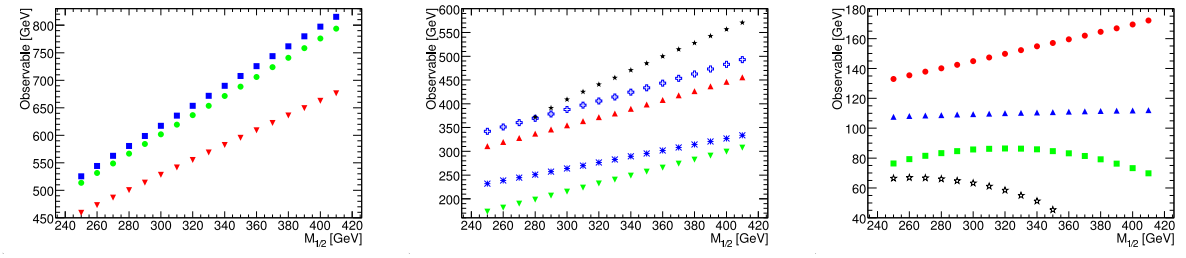

(a) (b) (c)

Figure 6.9: The evolution of the used observables as predicted by *Isasugra* with respect to $m_{1/2}$. (a) shows the evolution of the observables with the largest numerical values. These are $\sqrt{m^2_{\tilde{q}_R} - 2m^2_{\tilde{\chi}^0_1}}$ (squares), $m_{\tilde{g}} - m_{\tilde{\chi}^0_1}$ (circles) and $m^{high}_{lq}(\tilde{q}_L, \tilde{\chi}^0_2, \tilde{l}_R, \tilde{\chi}^0_1)$ (triangles). These observables show a linear dependence on $m_{1/2}$ in first order. (b) shows the observables with medium numerical values, which are $m^{max}_{tb}(\tilde{t}_1, \tilde{g}, \tilde{\chi}^+_1)$ (filled stars), which is available for $m^{in}_{1/2} > 270$ GeV only, $m^{max}_{tb}(\tilde{b}_{1,2}, \tilde{g}, \tilde{\chi}^+_1)$ (crosses for $\tilde{b}_1$, triangles pointing upwards for $\tilde{b}_2$), $m^{max}_{\tau\tau}(\tilde{\chi}^0_4, \tilde{\tau}_2, \tilde{\chi}^0_1)$ (stars) and $m_{\tilde{\chi}^+_1}$ (triangles pointing downwards). Finally, (c) shows the observables with the lowest numerical values. These are $\sqrt{m^2_{\tilde{l}_L} - 2m_{\tilde{\chi}^0_1}}$ (circles), m_{h_0} (triangles), $m^{max}_{ll}(\tilde{\chi}^0_2, \tilde{l}_R, \tilde{\chi}^0_1)$ (squares) and $m^{max}_{\tau\tau}(\tilde{\chi}^0_2, \tilde{\tau}_1, \tilde{\chi}^0_1)$ (stars).

These were scaled with the ratio of the respective cross sections to get rough estimates for the parameter points used for this comparison. Furthermore, for all observables, an additional uncertainty was taken into account for this first comparison. For each value of $m_{1/2}$, all observables are predicted using all four spectrum calculators. The maximum of the pairwise deviations

$$\Delta O_{max} = \max_{i,j}(|O_i - O_j|), \tag{6.11}$$

where i and j indicate the spectrum calculators, was then added to the experimental uncertainty in quadrature. For most observables, this contribution is in the same order as the experimental uncertainty. The SUSY observables, their predictions according to *Isasugra*, and the used uncertainties are listed for $m_{1/2} = 330$ GeV in table 6.4, as an example.

Finally it must be stated that for this study no assignment ambiguities (see, for example, [80]) for the mass edges are taken into account. If only a single ambiguity is considered in the SPS1a benchmark scenario, it was shown that for $\mathcal{L}_{int} \gtrsim 300$ fb^{-1}, the probability to actually take the wrong decision is about zero [80]. Although this picture might change if more than one ambiguity is taken into account, for the present study, all edges were assigned correctly.

6.3.4 Results

Approximately 100 smeared observable sets were thrown for each parameter point under investigation here. The exact number does not always equal 100 for various reasons. While at some points, single jobs failed due to problems on the LHCG, for other points more statistics was created for various reasons. The results of all fits for the parameter point at $m^{in}_{1/2} = 330$ GeV are shown in figure 6.10 as an example. A fit of the χ^2-distributions is in very good agreement with the input, i.e. 21 observables, 4 parameters and 0 bounds, which yields 17 degrees of freedom. Furthermore, a Gaussian distribution could be fitted to the parameter distributions, such that a mean and a width for each parameter could be extracted. The mean could then be

Observable	Value [GeV]	σ_{exp}^{est} [GeV]	ΔO_{max} [GeV]
m_{h_0}	110.33	0.13	0.60
$m_{\tilde{\chi}_1^+}$	240.51	12.91	0.81
$m_{ll}^{max}(\tilde{\chi}_2^0, \tilde{l}_R, \tilde{\chi}_1^0)$	86.31	0.12	6.02
$m_{\tau\tau}^{max}(\tilde{\chi}_2^0, \tilde{\tau}_1, \tilde{\chi}_1^0)$	55.01	6.17	10.67
$m_{\tau\tau}^{max}(\tilde{\chi}_4^0, \tilde{\tau}_2, \tilde{\chi}_1^0)$	282.93	7.87	5.66
$m_{\tilde{g}} - m_{\tilde{\chi}_1^0}$	653.47	14.89	5.19
$\sqrt{m_{\tilde{q}_R}^2 - 2m_{\tilde{\chi}_1^0}^2}$	671.67	11.17	5.92
$\sqrt{m_{\tilde{l}_L}^2 - 2m_{\tilde{\chi}_1^0}}$	152.27	6.82	7.67
$m_{lq}^{high}(\tilde{q}_L, \tilde{\chi}_2^0, \tilde{l}_R, \tilde{\chi}_1^0)$	568.73	5.62	11.44
$m_{tb}^{max}(\tilde{b}_1, \tilde{g}, \tilde{\chi}_1^+)$	414.23	5.01	5.83
$m_{tb}^{max}(\tilde{b}_2, \tilde{g}, \tilde{\chi}_1^+)$	379.64	6.16	9.11
$m_{tb}^{max}(\tilde{t}_1, \tilde{g}, \tilde{\chi}_1^+)$	454.76	5.01	11.61

Table 6.4: Used observables and their values as predicted by *Isasugra*, their assumed experimental uncertainties for 300 fb^{-1} at $\sqrt{s} = 14$ TeV and the maximum difference between the predictions of all four spectrum generators for $m_{1/2} = 330$ GeV.

interpreted as the overall best-fit value and the width of the Gaussian could be interpreted as the uncertainty on the central value.

The results of all fits are summarised in figure 6.11. Clear shifts of the best-fit values can be seen for all fitted parameters. For A_0, the central values obtained using *SPheno* tend to be higher than the values obtained with *SuSpect*, which generally yields higher values then *SoftSUSY*. For m_0, in general *SuSpect* yields higher values than *SoftSUSY* and *SPheno*. Such a general tendency is however not observed for $m_{1/2}$ and $\tan\beta$. Nevertheless, in subregions of the used parameter space, a clear "hierarchy" between the results obtained with the three RGE-codes is visible. For example, for $m_{1/2}^{in} \leq 350$ GeV, fits using *SPheno* seem to yield the lowest best-fit $\tan\beta$, while for $m_{1/2}^{in} \geq 360$ GeV, the value obtained using *SPheno* is always larger than the best-fit values obtained with *SoftSUSY* and *SuSpect*. It remains to mention that all best-fit values agree with each other within their estimated uncertainties. At this point, this is clearly not a surprise, as the deviations between the observable predictions using the different spectrum calculators have been used as uncertainties on the observables for the fit. Appendix B contains a short comparison of the best fit values obtained by using estimated experimental uncertainties only.

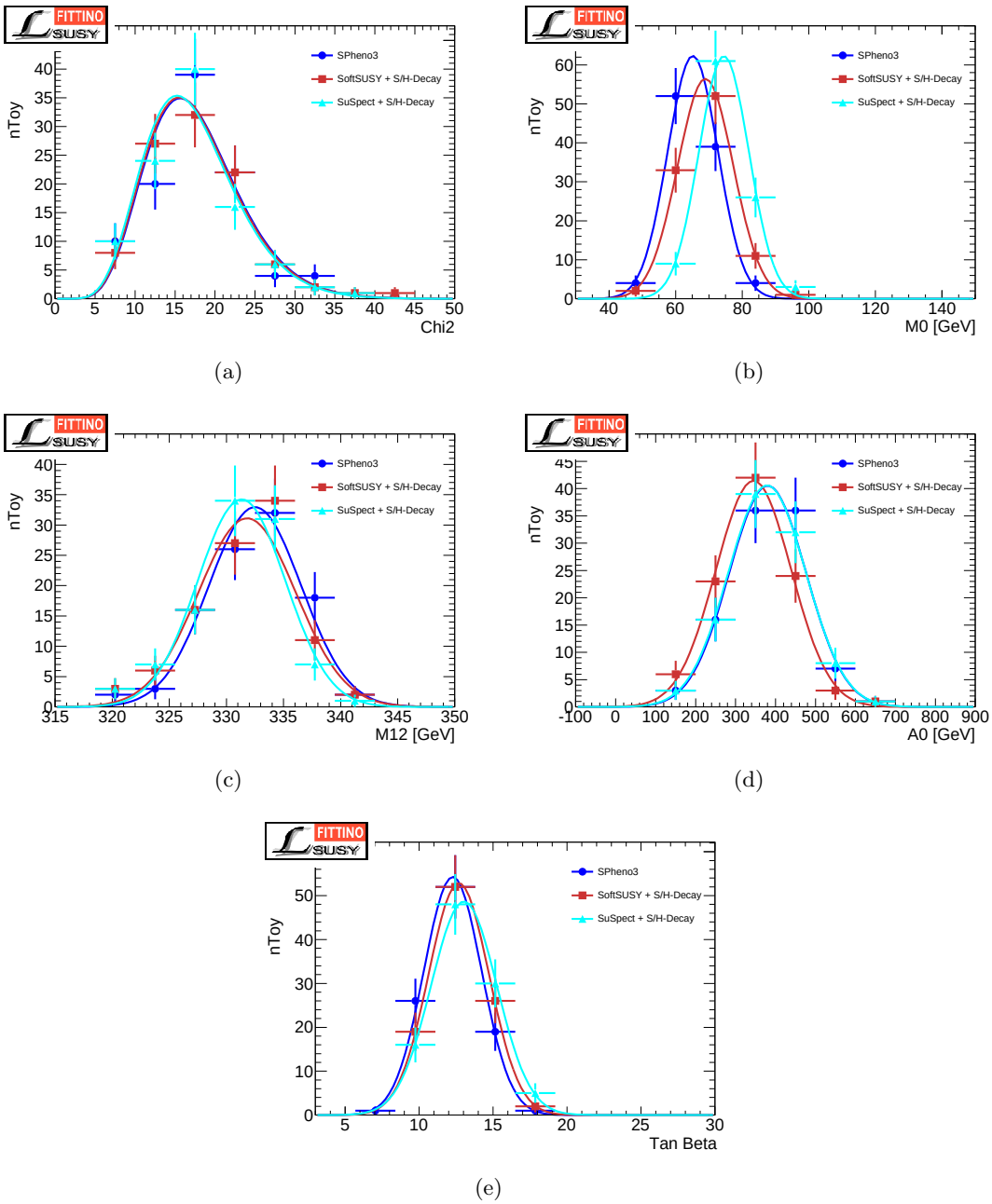

Figure 6.10: (a) χ^2-distributions and (b)-(e) the parameter distributions, for the fits performed at $m_{1/2}^{in} = 330$ GeV. At this point, all parameter distributions are well described by a Gaussian. Clear differences in the means of the respective distributions can be seen for m_0 in (b). The shifts for $m_{1/2}$ are also visible, although these are not that obvious as shown in (c). In the distributions of the parameter A_0 plotted in (d), *SPheno* and *SuSpect* show good agreement, while *SoftSUSY* is a little off with respect to these. For $\tan\beta$ finally, all three codes show small disagreements as plotted in (e). However, the χ^2 distributions for the fits show perfect agreement with the input (17 degrees of freedom) for all three interfaces, as shown in (a), which a posteriori justifies (6.11).

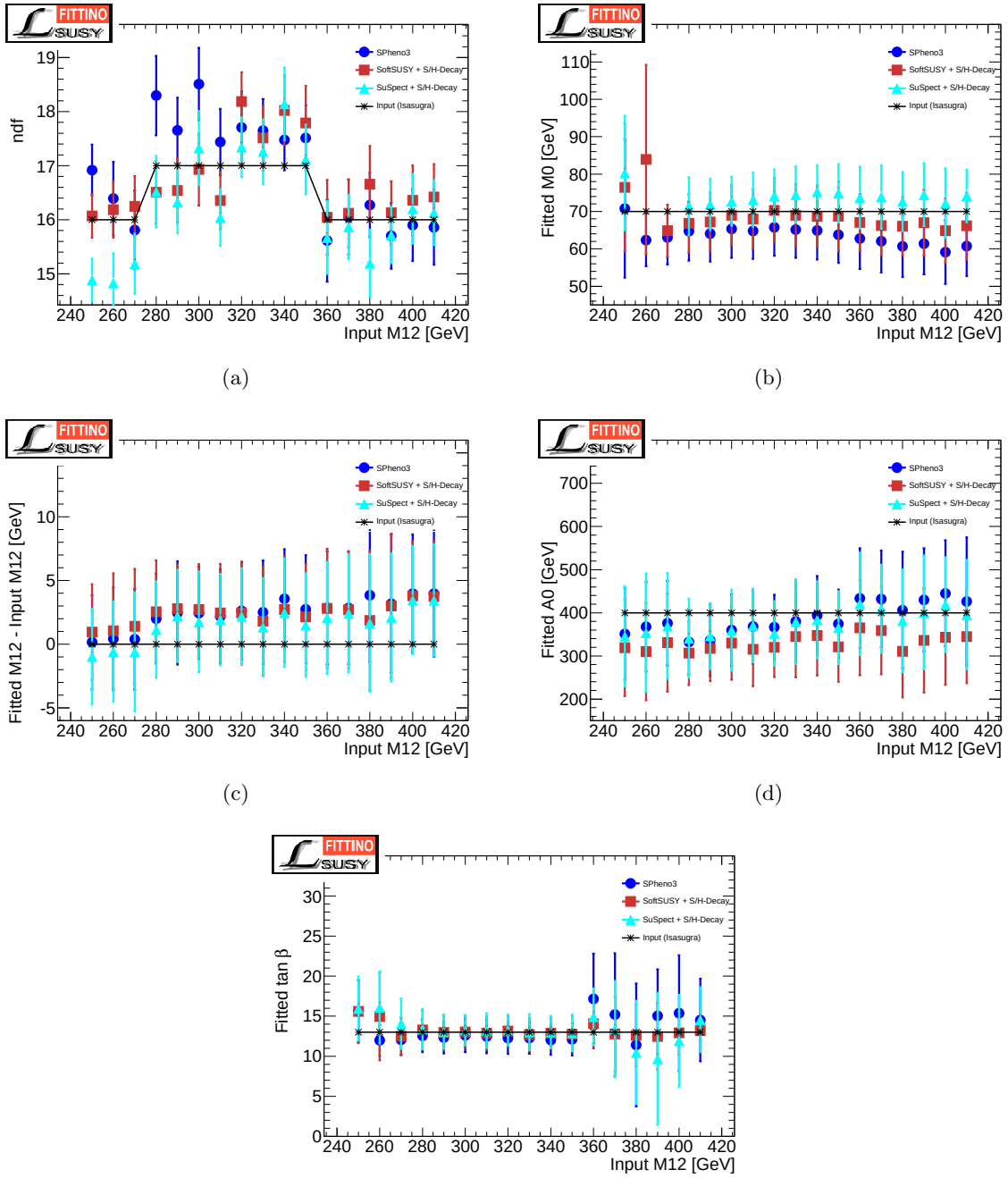

Figure 6.11: Summary of the comparisons of *SPheno*, *SoftSUSY* and *SuSpect*. (a) For the χ^2-distributions, the fitted number of degrees of freedom with its statistical uncertainty is shown. A fair agreement between the input and the fitted values is observed, although at some points, *SuSpect* seems to yield lower χ^2 values as expected, while fits with *SPheno* have a higher average χ^2 as expected. For the parameter distributions of m_0 in (b) and A_0 in (d) a clear hierarchy between the three codes can be seen over the whole examined parameter range, while this is not so evident for $m_{1/2}$ in (c) and $\tan\beta$ in (e).

The parameter m_0 turned out to be problematic here at two parameter points. For $m_{1/2}^{in} = 260$ GeV and $m_{1/2}^{in} = 270$ GeV, the m_0 distributions seem to show a second maximum when *SuSpect* is used for the fit, such that the fit of a Gaussian to the distribution yields unreasonable values. This is shown in figure 6.12, which indicates that this might also be the case if *SoftSUSY* is used, while the effect is not that large, though still visible, for *SPheno*. It remains to be seen if this is a statistical fluctuation or a real side minimum, since a significant increase of statistics, and therefore a significant amount of computing power is needed to clarify this.

The question is whether the observed differences in the central values can be interpreted as systematic shifts. This was studied by examining the correlations between the results obtained by fitting the parameters using each of the three RGE codes with the same smeared set of observables. Samples for the two-dimensional parameter distributions are shown in figure 6.13 and the extracted correlation coefficients for each parameter and each combination of spectrum calculators are shown in figures 6.14. The observed correlations are high, as it was expected if the shifts in the central values were systematic shifts. However, a problematic region in the parameter space was found here.

By examining the correlation coefficients for m_0, a "step" is observed around $m_{1/2}^{in} = 310$ GeV. The corresponding two-dimensional plots for $m_{1/2}^{in} = 250$ GeV with increased statistics to verify this effect are shown in figure 6.15. From these plots it can be seen that besides the main branch which reflects a high correlation, an anticorrelated side branch emerges.

In the first place, a connection between the anticorrelated branch and the usage of the observable $m_{tb}^{max}(\tilde{t}_1)$ was suspected, as the side branch is most distinctive at the points which kinematically forbid the required decay chain, and less distinct in the regions where the decay is allowed, but has only a small phase space available. On the other hand, it completely vanishes for even higher values of $m_{1/2}^{in}$. It was therefore doubted that the inclusion of the observable $m_{tb}^{max}(\tilde{t}_1)$ avoided the occurrence of the this side branch, as the sensitivity of the fit to m_0 is increased if $m_{tb}^{max}(\tilde{t}_1)$ is used.

To test this hypothesis, another series of fits was performed for the point at $m_{1/2}^{in} = 350$ GeV, at which the decay chain (6.10) is kinematically allowed, without using the observable $m_{tb}^{max}(\tilde{t}_1)$.

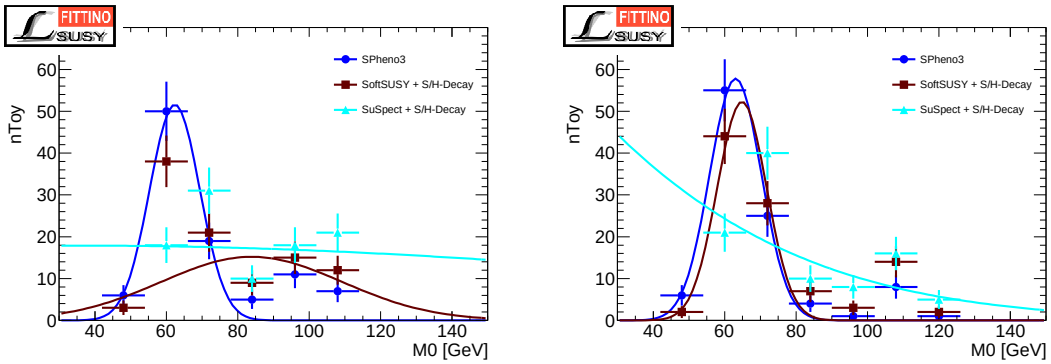

(a) (b)

Figure 6.12: Distributions for the parameter m_0 for the fits performed with an input of $m_{1/2}^{in} = 260$ GeV (a) and $m_{1/2} = 270$ GeV (b). At both points, the distribution obtained with *SuSpect* is clearly not well described by a Gaussian. This seems to be the case for the distributions obtained by *SPheno* and *SoftSUSY*, too. The reason for this remains unknown at this point.

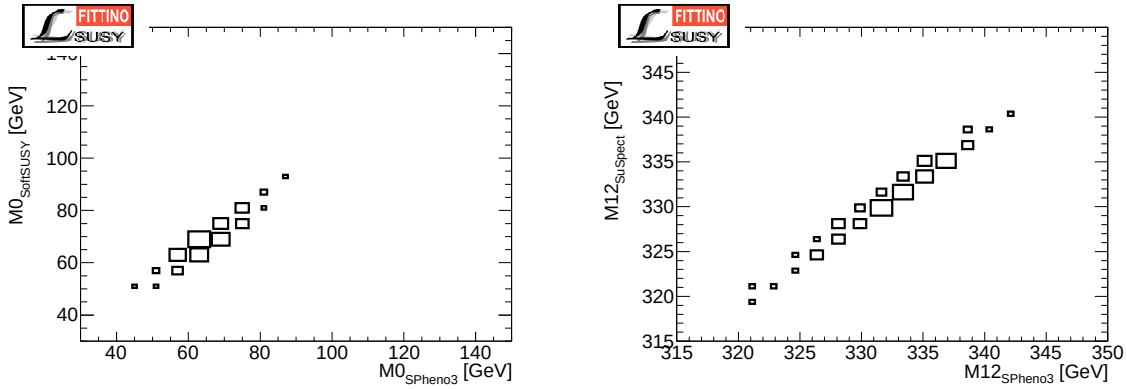

(a) (b)

Figure 6.13: Two dimensional distributions for the best-fit parameter values in the "calculator-space". Figure (a) shows the correlation between m_0^{SPheno} and $m_0^{SoftSUSY}$, (b) shows the correlations between $m_{1/2}^{SPheno}$ and $m_{1/2}^{SuSpect}$. For both parameters, the best-fit values are highly correlated. This matches the expectation for systematic shifts.

The resulting plots for the $m_0 - m_0$-correlations are shown in figure 6.16. The anticorrelated branch is not observed in the two-dimensional distributions for the fits neglecting $m_{tb}^{max}(\tilde{t}_1)$, such that it can tentatively be concluded that it is not due to the inclusion of this observable that the anticorrelation vanishes. Certainly, this has to be examined in a more rigorous way, which is out of the scope for the present thesis.

Finally, it can be stated that the new interfaces for *Fittino* work quite well for fits of mSUGRA Lagrangians and that they can be employed for studies of systematic uncertainties on best-fit values when using mass related SUSY observables.

In a first study of these systematic shifts, first hints for problematic parameters and regions in the mSUGRA parameter space have been found, which require a more detailed analysis.

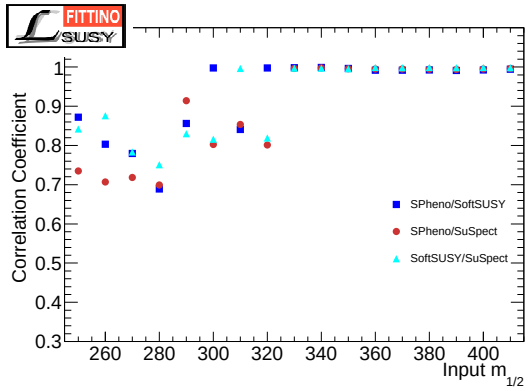

(a) m_0

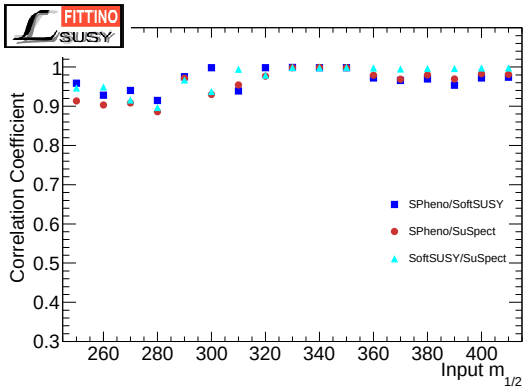

(b) $m_{1/2}$

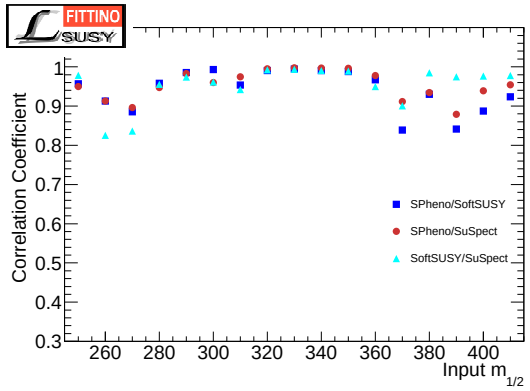

(c) A_0

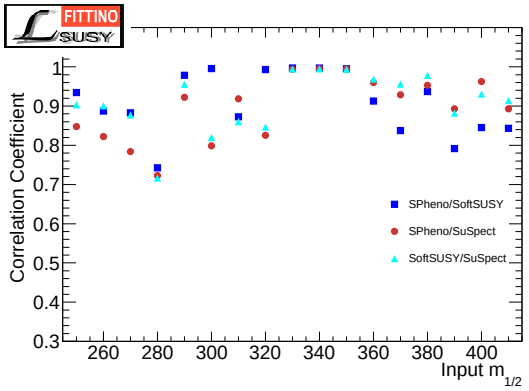

(d) $\tan\beta$

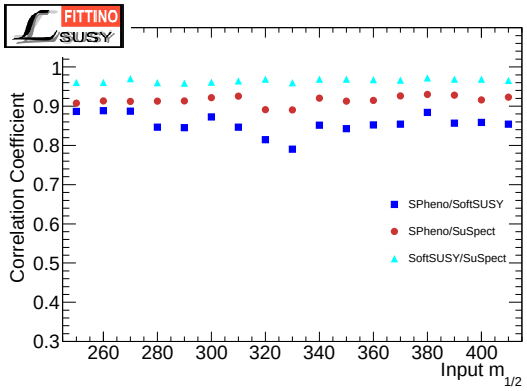

(e) χ^2

Figure 6.14: Correlation coefficients for the best-fit values for (a)-(d) all parameters, and (e) the χ^2 for all examined parameter sets. For all parameters and the χ^2, the correlation coefficients are well above 60%, which is expected. However, some features show up which need further investigation. For example, the step at $m_{1/2} \approx 310$ GeV for m_0 may indicate that there is some problem in this region.

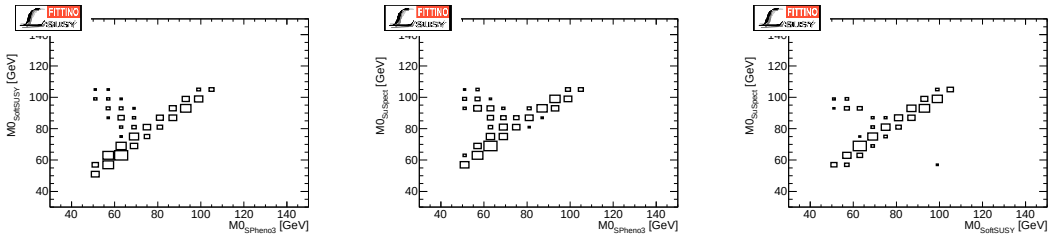

(a) (b) (c)

Figure 6.15: For $m_{1/2}^{in} = 250$ GeV, in addition to the clearly visible "main" branch, which reflects a high correlation between m_0^i and m_0^j, where i and j denote the spectrum calculators, an anticorrelated "side" branch emerges. For the plots shown in (a)-(c), 290 different random seeds have been used, and the "side" branch seems to be of non-statistical nature.

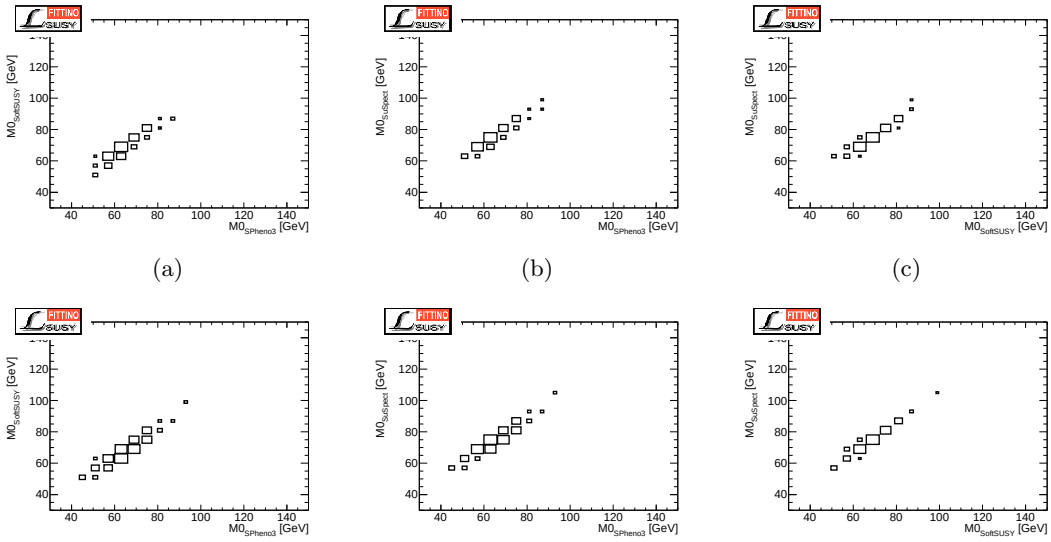

(a) (b) (c)

(d) (e) (f)

Figure 6.16: Correlations between the m_0 best-fit values for $m_{1/2} = 350$ GeV for all available used input observables (a)-(c), and for all used observables without $m_{tb}^{max}(\tilde{t}_1)$ (d)-(f). This parameter point does not show the anticorrelated "side"-branch. As it was suspected that the inclusion of this variable might be connected to the absence of the anticorrelated branch, parameter distributions have been created with *Fittino* neglecting this observable at a point at which it is available. As no "side"-branch can be seen in (d)-(f), it can be concluded that this first suspicion was not correct.

7 Summary and Outlook

7.1 Summary

A study on the measurement of a SUSY observable in a best case scenario and a first insight into systematic uncertainties for SUSY parameter reconstruction was presented.

The SUSY observable examined in the present thesis is a kinematic endpoint in the invariant dimuon mass spectrum of the SUSY decay chain

$$\tilde{\chi}_2^0 \to \tilde{\mu}_R \mu \to \tilde{\chi}_1^0 \mu\mu.$$

It was assumed that the SM background can be rejected with a purity and signal efficiency of 100%, and a function for the extraction of the endpoint, assuming a constant resolution factor for the dimuon mass, was tested. A total of 28 points in the mSUGRA parameterspace were taken and fits for the extraction of the endpoint were performed, taking into account a model for the supersymmetric and combinatorial background. This model turned out to be inadequate for 5 of these parameter points after a cut on the transverse momenta of the muons had been applied. The reason for this was shown to be the vicinity of the endpoint to the mass of the Z^0, which occurs at significant numbers in the SUSY decay chains at these points. For a number of reasons, the Z^0 mass peak was not included in the background model, such that these 5 parameter points were neglected, and 18 of the remaining points were randomly chosen for the determination of a calibration curve for the estimator of the kinematic endpoint.

The last 5 parameter points served as a control sample for the calibration curve and the calibrated, fitted estimators for the endpoint showed very good agreement with the theoretical values. However, the parametrisation of the calibration curve is in agreement with a straight line of slope 1 through the origin within 2σ. It could thus be concluded, that the assumption of a constant resolution factor for the dimuon mass is a good simplification and yields an unbiased estimator for the kinematic endpoint.

Furthermore, two new interfaces for the program *Fittino* have been written and successfully tested, allowing for a first study of systematic uncertainties on the central values of the SUSY Lagrangian parameters extracted from toy and possible future data. The SUSY spectrum calculators *SoftSUSY* and *SuSpect*, as well as the decay calculators *SDECAY* and *HDECAY* were linked to *Fittino*, which by default uses *SPheno* for the prediction of SUSY observables.

By performing toy fits of the four continuous mSUGRA parameters to the same pseudo-data at 17 different mSUGRA parameter points using all three spectrum calculators separately, shifts in the best-fit values were seen. These could be explained by small pairwise differences in the predictions obtained with the three RGE codes for the same input. A detailed analysis of the fit results, using *Fittino*'s capability to smear the input observables and generate parameter distributions, showed that these shifts are of systematic nature, rather than random deviations, which met the expectations.

Within the context of this study, a problematic region in the mSUGRA parameter space has been identified, as the two dimensional $m_{0,i} - m_{0,j}$ pull distributions, where i and j denote the three RGE packages, showed an anticorrelated branch for $i \neq j$ for some of the used parameter

sets. A first attempt to trace the emergence of this branch back to the usage of an edge in the top-bottom spectrum of a gluino decay chain showed no direct connection.

It can be summarised that the newly written *Fittino* interfaces work well for fits of mSUGRA models and have already been proven to allow for a wide range of interesting studies with the program *Fittino*.

7.2 Outlook

The examination of the estimator for the kinematic endpoint is of course far from being complete. SM background and a more refined technique for the extraction of the signal spectrum need to be examined, as well as additional uncertainties like the impact of the lepton energy scale, and trigger efficiencies. One technique for the reduction of any supersymmetric background was already tested. The results obtained with the method of statistical subtraction showed a significant deviation from the expectations, such that the more robust cut method had been used to determine the goodness of the estimator. This has to be studied further.

There is as well some more work to be done on the written *Fittino* interfaces. The functionality of the *SoftSUSY+SUSY-HIT* interface was successfully tested for fits of mSUGRA, GMSB and AMSB models, while the *SUSY-HIT* interface at the moment is known not to work for fits of GMSB models when *SuSpect* is being used as a spectrum calculator. This problem was traced back to *SuSpect* itself and is not directly related to the written interface. There are more models, for example the MSSM18 and MSSM24 which are generally supported by *Fittino*, but for which the new interfaces were not yet successfully tested. Problems when fitting these models using *SoftSUSY* or *SuSpect* can mainly be ascribed to the communication between *Fittino* and the external codes. For example, different phase conventions for SUSY masses may disturb the communication between *SoftSUSY* and *SUSY-HIT*. These problems were mainly identified and removed already, but a number of yet unsolved problems still remain.

However, as the *Fittino* collaboration decided to completely rewrite the whole program from scratch in a more object oriented way, to allow for an easy extension of the code and an easy inclusion of new models, like the E_6MSSM [87], this work will be done in the near future during the recoding of *Fittino*.

On the physics side, there is also a number of things to do, which are directly connected to the work presented in this thesis. A detailed analysis of the anticorrelated branch in the $m_{0,i} - m_{0,j}$ needs to be performed and the origin of this branch has to be identified. In addition, if only expected experimental uncertainties for a collected data set of 300 fb^{-1} are used for the fits, the systematic shifts for m_0 exceed the widths of the single parameter distributions by one order of magnitude, roughly. The shifts are not that large for the other mSUGRA parameters. Although an agreement within one standard deviation is not expected when theoretical uncertainties on the observables are not included, the parameter m_0 seems to require a detailed examination here, as well. However, it is most likely that the differences between the SUSY spectrum calculators become smaller long before such a large dataset has been collected, as the knowledge about SUSY, if it turns out to exist, will certainly increase until then.

Furthermore the possibility to fit the electroweak symmetry breaking scale Q_{EWSB} as a nuisance parameter has recently been added to *Fittino*. The impact of this on the differences between the results obtained with the three RGE packages would be interesting to know, as well.

A comparison of misinterpretation probabilities could also be performed with the new interfaces. For certain configurations in the mSUGRA parameterspace for example, the slepton in (5.1) could be both the $\tilde{l}_R$ and a $\tilde{l}_L$. In such a scenario, two endpoints could be measured in the

dilepton spectrum, given that both decays acquire a sufficiently high branching fraction. A priori, it was not clear which edge has to be assigned to which slepton. One method to resolve this is described in [80]. There is a significant number of such assignment ambiguities when dealing with SUSY observables, and a detailed analysis is currently being performed by members of the *Fittino* collaboration using *SPheno* only. A comparison of the available spectrum and decay calculators would be desirable here, too.

If nature turns out to be supersymmetric, it is expected that first fits of SUSY Lagrangians can be performed with a dataset of 1fb^{-1} at $\sqrt{s} = 14$ TeV already, which in a very optimistic scenario might be available end of 2013 or early 2014. Given that SUSY is realised in nature, the first sparticles might already have been produced at the LHC, as in December 2009, with the first collisions at the so far unreached center of mass energy of 2.36 TeV, physicists at CERN have successfully started to explore strange new worlds, to seek out new particles and new interactions, to boldly go where no man has gone before.

A Statistical Subtraction of Combinatorial Background

A common approach for a better separation of signal and background with respect to the method used in chapter 5 is a statistical subtraction of opposite sign opposite flavour (OSOF) lepton pairs [59]. This means, that the invariant mass spectrum for electron-muon combinations of opposite charge is determined and subtracted from the dimuon spectrum taking into account a scaling factor of 1/2. According to lepton universality, the remaining spectrum should be free of combinatorial background within statistical limits. This method has been tested on generator level here. The invariant mass distribution of the combinatorial background as well as the electron-muon combinations turned out to be well described by an exponential for $m_{ll} \gtrsim 30$ GeV. However, the results were not satisfactory. This is shown in a little detail in figure A.1, where a loose cut on the transverse momentum has been applied, $p_T^{e/\mu} > 5$ GeV, to get rid of very soft leptons.
For the study presented in chapter 5, this technique has thus not been used. A more refined treatment might resolve this problem. As an example, the p_T cut could be slightly increased. However, it was decided that the method presented in chapter 5 was sufficient for the first test of the estimator.

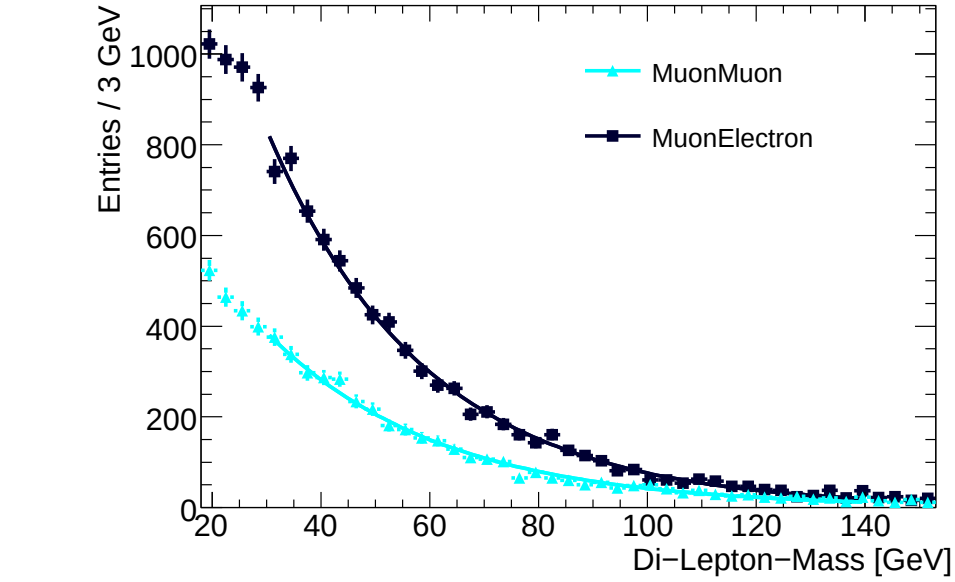

(a)

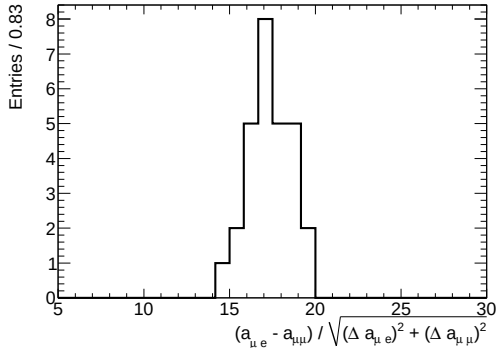

(b)

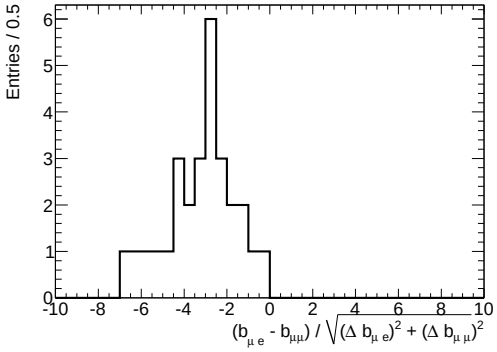

(c)

Figure A.1: (a) shows the invariant dilepton mass spectra for combinatorial muon-muon background and for muon-electron combinations (generator level). For $m_{ll} > 30$ GeV, both distributions can be fitted with an exponential, which has two parameters: the slope b of the exponential and a constant a (normalization factor). The diagrams (b) and (c) summarize the results of the performed fits. Pull distributions for the fitted parameters have been created. The pull for the constant a qualitatively meets the expectation, as a higher number of muon-electron combinations than background muon-muon combinations is expected. However, a clear bias in the pull for the exponential slope b can be seen. This is not expected and needs to be studied further.

B Fits of mSUGRA Lagrangians Using Estimated Experimental Uncertainties Only

Figure B.1 shows the m_0- and A_0-distributions obtained by *Fittino* when only estimated experimental uncertainties for an integrated luminosity of 300fb^{-1} at $\sqrt{s} = 14$ TeV are used for the fits. The deviations are significant. These plots show that a comparison like the one presented in chapter 6 is important if SUSY Lagrangians are fitted to data. Of course the differences between the three spectrum calculators are expected to decrease long before a dataset of 300fb^{-1} has been collected. Nevertheless, first fits might be possible using observables extracted from 1fb^{-1}. At this points, a comparison of the fit results obtained using either *SPheno*, *SoftSUSY* or *SuSpect* is of importance for the determination of the parameter uncertainties.

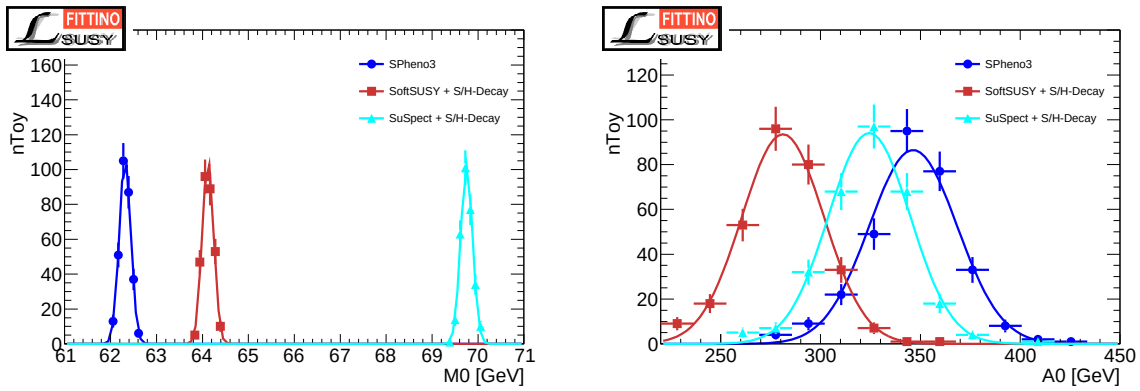

(a) (b)

Figure B.1: Distributions for (a) m_0 and (b) A_0 when using estimates for the experimental uncertainties with a dataset of 300fb^{-1} only. The deviation between the central values is significant, especially for the parameter m_0.

List of Figures

List of Tables

Bibliography

[1] M. Planck, *Wissenschaftliche Selbstbiographie: Mit einem Bildnis und der von Max von Laue gehaltenen Traueransprache, 2. Auflage*, Johann Ambrosius Barth Verlag Leipzig, (1948).

[2] J. J. Thomson, *Cathode rays*, Phil. Mag. **44** (1897) 293.

[3] C. Campagnari and M. Franklin, *The Discovery of the Top Quark*, Rev. Mod. Phys. **69** (1997) 137, `hep-ex/9608003`.

[4] The DONuT Collaboration, K. Kodama *et al.*, *Final tau-neutrino results from the DONuT experiment*, Phys. Rev. **D78** (2008) 052002, `0711.0728`.

[5] G. Quast, *Global fit to electroweak precision data*, Eur. Phys. J. **C33** (2004) s641.

[6] The Gfitter Collaboration, J. Haller, *Fits of the Electroweak Standard Model and Beyond using Gfitter*, `0810.3664`.

[7] H. Flacher *et al.*, *Gfitter - Revisiting the Global Electroweak Fit of the Standard Model and Beyond*, Eur. Phys. J. **C60** (2009) 543, `0811.0009`.

[8] The Gfitter Collaboration, A. Hoecker, *Status of the global electroweak fit of the Standard Model*, `0909.0961`.

[9] S. Weinberg, *The Quantum theory of fields. Vol. 1: Foundations*, Cambridge, UK: Univ. Pr. (1995) 609 p.

[10] S. Weinberg, *The quantum theory of fields. Vol. 2: Modern applications*, Cambridge, UK: Univ. Pr. (1996) 489 p.

[11] S. Weinberg, *The quantum theory of fields. Vol. 3: Supersymmetry*, Cambridge, UK: Univ. Pr. (2000) 419 p.

[12] F. Halzen and A. Martin, *Quarks and Leptons: An Introductory Course in Modern Particle Physics*, John Wiley & Sons, (1984).

[13] D. Griffiths, *Introduction to Elementary Particles*, Wiley-VCH Verlag GmbH & Co. KGaA, (2004).

[14] J. C. Maxwell, *A dynamical theory of the electromagnetic field*, Phil. Trans. Roy. Soc. Lond. **155** (1865) 459.

[15] S. Weinberg, *Feynman Rules for Any Spin. 2. Massless Particles*, Phys. Rev. **134** (1964) B882.

[16] The Particle Data Group Collaboration, C. Amsler *et al.*, *Review of particle physics*, Phys. Lett. **B667** (2008) 1.

[17] E. Noether, *Invariante Variationsprobleme.*, Goett. Nachr. (1918) 235.

[18] E. P. Wigner, *Gruppentheorie und ihre Anwendung auf die Quantenmechanik der Atomspektren*, Vieweg, (1931).

[19] C. L. Bennett *et al.*, *4-Year COBE DMR Cosmic Microwave Background Observations: Maps and Basic Results*, Astrophys. J. **464** (1996) L1, `astro-ph/9601067`.

[20] The WMAP Collaboration, G. Hinshaw *et al.*, *Five-Year Wilkinson Microwave Anisotropy Probe (WMAP) Observations:Data Processing, Sky Maps, & Basic Results*, Astrophys. J. Suppl. **180** (2009) 225, `0803.0732`.

[21] S. R. Coleman and J. Mandula, *ALL POSSIBLE SYMMETRIES OF THE S MATRIX*, Phys. Rev. **159** (1967) 1251.

[22] R. Haag, J. T. Lopuszanski, and M. Sohnius, *All Possible Generators of Supersymmetries of the s Matrix*, Nucl. Phys. **B88** (1975) 257.

[23] I. J. R. Aitchison, *Supersymmetry in particle physics: An elementary introduction*, SLAC-R-865.

[24] S. P. Martin, *A Supersymmetry Primer*, `hep-ph/9709356`.

[25] G. Jungman, M. Kamionkowski, and K. Griest, *Supersymmetric dark matter*, Phys. Rept. **267** (1996) 195, `hep-ph/9506380`.

[26] F. Kuypers, *Klassische Mechanik*, Wiley-VCH Verlag GmbH & Co. KGaA, 6th edn., (2003).

[27] J. L. Kneur and N. Sahoury, *Bottom-Up Reconstruction Scenarios for (un)constrained MSSM Parameters at the LHC*, Phys. Rev. **D79** (2009) 075010, `0808.0144`.

[28] Bruning, Oliver Simon and Collier, Paul and Lebrun, P and Myers, Stephen and Ostojic, Ranko and Poole, John and Proudlock, Paul, *LHC Design Report*, vol. 1, CERN, Geneva, (2004).

[29] Bruning, Oliver Simon and Collier, Paul and Lebrun, P and Myers, Stephen and Ostojic, Ranko and Poole, John and Proudlock, Paul, *LHC Design Report*, vol. 2, CERN, Geneva, (2004).

[30] M. Benedikt, P. Collier, V. Mertens, J. Poole, and K. Schindl, *LHC Design Report*, vol. 3, CERN, Geneva, (2004).

[31] The ILC Collaboration, J. Brau, (Ed.) *et al.*, *ILC Reference Design Report Volume 1 - Executive Summary*, `0712.1950`.

[32] The ILC Collaboration, G. Aarons *et al.*, *International Linear Collider Reference Design Report Volume 2: PHYSICS AT THE ILC*, `0709.1893`.

[33] The ILC Collaboration, N. Phinney *et al.*, *International Linear Collider Reference Design Report Volume 3: Accelerator*, `0712.2361`.

[34] The ILC Collaboration, T. Behnke, (Ed.) *et al.*, *ILC Reference Design Report Volume 4 - Detectors*, `0712.2356`.

[35] P. Bechtle, K. Desch, and P. Wienemann, *Fittino, a program for determining MSSM parameters from collider observables using an iterative method*, Comput. Phys. Commun. **174** (2006) 47, `hep-ph/0412012`.

[36] W. Porod, *SPheno, a program for calculating supersymmetric spectra, SUSY particle decays and SUSY particle production at e+ e- colliders*, Comput. Phys. Commun. **153** (2003) 275, `hep-ph/0301101`.

[37] B. C. Allanach, *SOFTSUSY: A C++ program for calculating supersymmetric spectra*, Comput. Phys. Commun. **143** (2002) 305, `hep-ph/0104145`.

[38] A. Djouadi, J.-L. Kneur, and G. Moultaka, *SuSpect: A Fortran code for the supersymmetric and Higgs particle spectrum in the MSSM*, Comput. Phys. Commun. **176** (2007) 426, `hep-ph/0211331`.

[39] *ATLAS: Detector and physics performance technical design report. Volume 1*, CERN-LHCC-99-14.

[40] *ATLAS detector and physics performance. Technical design report. Vol. 2*, CERN-LHCC-99-15.

[41] The CMS Collaboration, G. L. Bayatian *et al.*, *CMS physics: Technical design report*, CERN-LHCC-2006-001.

[42] The LHCb Collaboration, S. Amato *et al.*, *LHCb technical proposal*, CERN-LHCC-98-04.

[43] *ALICE: Technical proposal for a large ion collider experiment at the CERN LHC*, CERN-LHCC-95-71.

[44] The TOTEM Collaboration, V. Berardi *et al.*, *TOTEM: Technical design report. Total cross section, elastic scattering and diffraction dissociation at the Large Hadron Collider at CERN*, CERN-LHCC-2004-002.

[45] The LHCf Collaboration, O. Adriani *et al.*, *Technical design report of the LHCf experiment: Measurement of photons and neutral pions in the very forward region of LHC*, CERN-LHCC-2006-004.

[46] *CERN press release PR09.08, 20.09.2008*, http://press.web.cern.ch/press/PressReleases/Releases2008/PR09.08E.html.

[47] *AthenaFramwork*, `https://twiki.cern.ch/twiki/bin/view/Atlas/AthenaFramework, revision r60`.

[48] G. Barrand *et al.*, *GAUDI - A software architecture and framework for building HEP data processing applications*, Comput. Phys. Commun. **140** (2001) 45.

[49] G. Corcella *et al.*, *HERWIG 6.5: an event generator for Hadron Emission Reactions With Interfering Gluons (including supersymmetric processes)*, JHEP **01** (2001) 010, `hep-ph/0011363`.

[50] S. Frixione and B. R. Webber, *The MC@NLO 2.2 event generator*, `hep-ph/0309186`.

[51] M. L. Mangano, M. Moretti, F. Piccinini, R. Pittau, and A. D. Polosa, *ALPGEN, a generator for hard multiparton processes in hadronic collisions*, JHEP **07** (2003) 001, `hep-ph/0206293`.

[52] The GEANT4 Collaboration, S. Agostinelli *et al.*, *GEANT4: A simulation toolkit*, Nucl. Instrum. Meth. **A506** (2003) 250.

[53] D. Cavalli, D. Costanzo, S. Dean, M. Duhrssen, S. Hassani, M. Heldmann, K. Jakobs, A. Nairz, A. Phillips, S. Resconi, E. Richter-Was, P. Sherwood, L. Vacavant, I. Vivarelli, J. B. De Vivie de Riégie, and I. Wingerter-Seez, *Performance of the ATLAS fast simulation ATLFAST*, Tech. Rep. ATL-PHYS-INT-2007-005. ATL-COM-PHYS-2007-012, CERN, Geneva, (Jan 2007).

[54] J. Hofestaedt, *Monte Carlo studies of the inverse problem: determination of the mass of the lightes supersymmetric particle with ATLAS at the LHC*, Bachelorarbeit, II. Physikalisches Institut, Georg-August Universitaet Goettingen.

[55] J. M. Butterworth, J. R. Forshaw, and M. H. Seymour, *Multiparton interactions in photoproduction at HERA*, Z. Phys. **C72** (1996) 637, `hep-ph/9601371`.

[56] F. E. Paige, S. D. Protopopescu, H. Baer, and X. Tata, *ISAJET 7.69: A Monte Carlo event generator for p p, anti-p p, and e+ e- reactions*, `hep-ph/0312045`.

[57] F. E. Paige, S. D. Protopopescu, H. Baer, and X. Tata, *ISAJET 7.79: A Monte Carlo event generator for p p, anti-p p, and e+ e- reactions*, taken from http://www.hep.fsu.edu/ isajet/.

[58] *Atlfast II*, `https://twiki.cern.ch/twiki/bin/view/Atlas/AtlfastII, revision r50`.

[59] The The ATLAS Collaboration, G. Aad *et al.*, *Expected Performance of the ATLAS Experiment - Detector, Trigger and Physics*, `0901.0512`.

[60] C. Cohen-Tannoudji, B. Diu, and F. Laloe, *Quantenmechanik, Tl.1*, de Gruyter, 2nd edn., (1999).

[61] A. Caldwell, D. Kollar, and K. Kroeninger, *BAT - The Bayesian Analysis Toolkit*, Comp. Phys. Commun. **180** (2009) 2197.

[62] I. Antcheva *et al.*, *ROOT: A C++ framework for petabyte data storage, statistical analysis and visualization*, Comput. Phys. Commun. **180** (2009) 2499.

[63] R. Lafaye, T. Plehn, and D. Zerwas, *SFITTER: SUSY parameter analysis at LHC and LC*, `hep-ph/0404282`.

[64] R. Lafaye, T. Plehn, M. Rauch, and D. Zerwas, *Measuring Supersymmetry*, Eur. Phys. J. **C54** (2008) 617, `0709.3985`.

[65] A. Djouadi, M. M. Muhlleitner, and M. Spira, *Decays of Supersymmetric Particles: the program SUSY-HIT (SUspect-SdecaY-Hdecay-InTerface)*, Acta Phys. Polon. **B38** (2007) 635, `hep-ph/0609292`.

[66] The Muon g-2 Collaboration, G. W. Bennett *et al.*, *Measurement of the negative muon anomalous magnetic moment to 0.7-ppm*, Phys. Rev. Lett. **92** (2004) 161802, `hep-ex/0401008`.

[67] The Muon G-2 Collaboration, G. W. Bennett *et al.*, *Final report of the muon E821 anomalous magnetic moment measurement at BNL*, Phys. Rev. **D73** (2006) 072003, `hep-ex/0602035`.

[68] The CLEO Collaboration, S. Ahmed *et al.*, *b to s gamma branching fraction and CP asymmetry*, hep-ex/9908022.

[69] O. Buchmueller *et al.*, *Predictions for Supersymmetric Particle Masses in the CMSSM using Indirect Experimental and Cosmological Constraints*, JHEP **09** (2008) 117, 0808.4128.

[70] S. Heinemeyer, W. Hollik, and G. Weiglein, *FeynHiggs: a program for the calculation of the masses of the neutral CP-even Higgs bosons in the MSSM*, Comput. Phys. Commun. **124** (2000) 76, hep-ph/9812320.

[71] F. Mahmoudi, *SuperIso: A program for calculating the isospin asymmetry of B -¿ K* gamma in the MSSM*, Comput. Phys. Commun. **178** (2008) 745, 0710.2067.

[72] F. Mahmoudi, *SuperIso v3.0, flavor physics observables calculations: Extension to NMSSM*, Comput. Phys. Commun. **180** (2009) 1718.

[73] P. Gondolo *et al.*, *DarkSUSY: Computing supersymmetric dark matter properties numerically*, JCAP **0407** (2004) 008, astro-ph/0406204.

[74] G. Belanger, F. Boudjema, A. Pukhov, and A. Semenov, *micrOMEGAs: A program for calculating the relic density in the MSSM*, Comput. Phys. Commun. **149** (2002) 103, hep-ph/0112278.

[75] G. Belanger, F. Boudjema, A. Pukhov, and A. Semenov, *micrOMEGAs2.0: A program to calculate the relic density of dark matter in a generic model*, Comput. Phys. Commun. **176** (2007) 367, hep-ph/0607059.

[76] B. Allanach, S. Kraml, and W. Porod, *Comparison of SUSY mass spectrum calculations*, hep-ph/0207314.

[77] P. Z. Skands *et al.*, *SUSY Les Houches Accord: Interfacing SUSY Spectrum Calculators, Decay Packages, and Event Generators*, JHEP **07** (2004) 036, hep-ph/0311123.

[78] M. Muhlleitner, *SDECAY: A Fortran code for SUSY particle decays in the MSSM*, Acta Phys. Polon. **B35** (2004) 2753, hep-ph/0409200.

[79] A. Djouadi, J. Kalinowski, and M. Spira, *HDECAY: A program for Higgs boson decays in the standard model and its supersymmetric extension*, Comput. Phys. Commun. **108** (1998) 56, hep-ph/9704448.

[80] P. Bechtle, K. Desch, M. Uhlenbrock, and P. Wienemann, *Constraining SUSY models with Fittino using measurements before, with and beyond the LHC*, 0907.2589.

[81] G. Belanger, S. Kraml, and A. Pukhov, *Comparison of SUSY spectrum calculations and impact on the relic density constraints from WMAP*, Phys. Rev. **D72** (2005) 015003, hep-ph/0502079.

[82] The LHC/LC Study Group Collaboration, G. Weiglein *et al.*, *Physics interplay of the LHC and the ILC*, Phys. Rept. **426** (2006) 47, hep-ph/0410364.

[83] M. M. Nojiri, G. Polesello, and D. R. Tovey, *Proposal for a new reconstruction technique for SUSY processes at the LHC*, hep-ph/0312317.

[84] C. G. Lester and D. J. Summers, *Measuring masses of semiinvisibly decaying particles pair produced at hadron colliders*, Phys. Lett. **B463** (1999) 99, `hep-ph/9906349`.

[85] A. Barr, C. Lester, and P. Stephens, *m(T2) : The Truth behind the glamour*, J. Phys. **G29** (2003) 2343, `hep-ph/0304226`.

[86] J. Hisano, K. Kawagoe, and M. M. Nojiri, *A detailed study of the gluino decay into the third generation squarks at the CERN LHC*, Phys. Rev. **D68** (2003) 035007, `hep-ph/0304214`.

[87] S. F. King, S. Moretti, and R. Nevzorov, *Theory and phenomenology of an exceptional supersymmetric standard model*, Phys. Rev. D **73(3)** (Feb 2006) 035009.

[88] *http://www.interactions.org*, ImageBank.

[89] H. Murayama, *Supersymmetry phenomenology*, `hep-ph/0002232`.

[90] *http://www.physics.gla.ac.uk/ppt/susy.htm*.

[91] *http://cdsweb.cern.ch*.

[92] *http://silicondetector.org*.

[93] *http://atlas.web.cern.ch*.

Acknowledgements

First of all, I would like to thank Dr. Carsten Hensel and Prof. Dr. Arnulf Quadt for giving me the opportunity to work in the Emmy Noether Nachwuchsgruppe at the II. Physikalisches Institut in Göttingen and for acting as referees for my thesis.

I especially would like to thank Dr. Carsten Hensel for supervising me during my study, for providing me with helpful advice and suggestions and for patiently answering my questions.

Special thanks go to Dr. Kevin Kröninger for his invaluable help concerning the field of statistics and for his advice during the writing of my thesis.

I also thank Dr. Jörn Grosse-Knetter for his advices during the writing of the thesis.

My very special gratitude goes to Anna Henrichs, who has always supported me not only in the field of physics, especially when I wrote down my thesis, but also in any other part of my life.

I would like to Fabian Kohn and Alexander Mann for their great help during my work here.

I would also like to thank Dr. Philip Bechtle for kindly advising me during my work on and with *Fittino* and for organising all the interesting and fruitful workshops on *Fittino*.

Finally, I thank all the members of the II. Physikalisches Institut in Göttingen for helpful discussions.

Last but certainly not least I would also like to thank my family, especially my parents Monika and Josef and my brothers Philipp and Simon, for their overwhelming support during my time in Göttingen.